Spring 5-15-2020

Self Capacitance based Wireless Power Transfer for Wearable Electronics: Theory and Implementation

Yarub Omer Alazzawi
Washington University in St. Louis

WASHINGTON UNIVERSITY IN ST. LOUIS

School of Engineering and Applied Science

Department of Electrical & Systems Engineering

Dissertation Examination Committee:
Shantanu Chakrabartty
Roger Chamberlain
Erica Scheller
Chuan Wang
Xuan Zhang

Self Capacitance based Wireless Power Transfer for Wearable Electronics:

Theory and Implementation

by

Yarub Omer Naji Alazzawi

A dissertation presented to
The Graduate School
of Washington University in
partial fulfillment of the
requirements for the degree
of Doctor of Philosophy

May 2020
Saint Louis, Missouri

Contents

List of Figures

List of Tables

Acknowledgments

I would like to express my sincere gratitude to a number of individuals and institutions, whose generous support and encouragement have led me to successfully finish this dissertation. I would like to thank Prof. Shantanu Chakrabartty, my advisor, for guiding me along my research progress and graciously supporting me through the course of the degree. I would like to thank my parents for everything they have done for me, my brothers; Farooq, Muhanad, Zaid, Suhaib and Hamza, my little lovely kids; Rawia, Maria and Hashumee, and my wife Riam, this dissertation would not have been possible without them.

I would also like to acknowledge the financial support from the National Institutes of Health (NIH) (Award Number: R01-DE027098), discretionary funding from the Department of Electrical and Systems Engineering (ESE) at Washington University in Saint Louis, and the Higher Committee for Educational Development in Iraq (HCED). Support from Metal Oxide Semiconductor Implementation Services (MOSIS) was vital in fabricating chips for this dissertation.

I would also like to thank the rest of my committee: Dr. Roger Chamberlain, Dr. Erica L. Scheller, Dr. Chuan Wang and Dr. Xuan Zhang for their time, thoughtful comments

and suggestions to this dissertation. I would also thank all the past and current members of the Adaptive Integrated Microsystems Lab: Kenji Aono, Tao Feng, Liang Zhou, Hassan Khan, Mingquan Yuan, Ahana Gangopadhyay, Oindrila Chatterjee, Brittany Scheid, Sri Harsha Kondapalli, Darshit Mehta, Mustafizur Rahman, and Owen Pochettino for research brainstorming and hanging out together. I would like to thank all the relatives and friends I already have and I have made since I started my Ph.D. journey especially in Michigan State University in East Lansing/Michigan, Kalamazoo/Michigan, Iraq and others in Saint Louis/Missouri.

Last but not the least, special thank with love to my Dad who died in China/Shanghai in Friday $January/10^{th}/2020$, while I was writing this dissertation. Although his death hardly broke my heart, but it hasn't stopped me from going forward on my progress the way he was continuously encouraging me until the last moment and more because basically this is the life which doesn't stop for his death or anyone else. I hope you, Dad rest in peace wherever you are right now and to the mercy of God.

Yarub Omer Naji Alazzawi

Washington University in Saint Louis

May 2020

Dedicated to mum and dad, for their encouragement, love and support

ABSTRACT OF THE DISSERTATION

Self Capacitance based Wireless Power Transfer for Wearable Electronics:

Theory and Implementation

by

Yarub Omer Naji Alazzawi

Doctor of Philosophy in Electrical Engineering

Washington University in St. Louis, 2020

Professor Shantanu Chakrabartty, Chair

Wireless power transfer (WPT) is a technology of transmitting power through different mediums to electronic devices that can be wearable or implantable for the purpose of energy harvesting. Conventionally, there are four standard types of WPT; Radio Frequency (RF), Magnetic Induction (Ind), Ultrasound (US), and Capacitive Coupling. Some of these are remotely delivered, others are locally. Conventional WPT approaches work on the principle of mutual coupling where the return paths for the source current and the load current are separate. As a result of that, the power transfer efficiency (PTE) of these approaches scales non-linearly with cross-sectional area of the transducers and the relative distance and respective alignment between the transducers.

In this work, we have invested the special properties of the self-capacitance (SC) of any electrically isolated body to deliver the power wirelessly to wearable or surface mounted

electronics. SC-based WPT is a technique that converts electrostatic energy into DC voltage, which has been used here for delivering the power over the human body surface to wearable electronic devices. The main goals of the design are to achieve the high power transfer efficiency (PTE) and deliver the power to the mm-sized electronics over a comparable long delivery distance. SC-based WPT has not been explored before, which uses floating electrodes for both power source and receiver to construct a hypothetical external ground that serves as the return path for the displacement current.

We showed that the SC-based WPT technology can be extended to provide the necessary energy to numerous low-power, wirelessly connected mm-sized nodes as needed for the next generation of the Internet of Things (IOT); specifically on the human body for the purpose of wireless health monitoring and/or fitness tracking such as in smart rooms application. The work also includes the design and implementation of power efficient wearable electronics (sensors and wireless receivers) using a common reference circuit called Proportional-To-Absolute-Temperature (PTAT) circuit. Using PTAT circuit, we have been able to reduce the complexity of the standard ultrasound receiver and the biosensor, hence making them both highly efficient in terms of noise and power consumption in addition to reducing the size of wearable electronics accordingly. We believe that our proposed WPT technique will have a great impact on the field of energy harvesting and wearable electronics, making the possibility of smart clothings and smart utilities in the near future a reality.

Chapter 1

Introduction

1.1 Motivation

Biomechatronics engineering is the field of studying the design and implementation of Mechatronics (Mechanics and Electronics) systems for biological applications such as therapy and diagnostic devices that can make the patients live easier. Hence, it bridges the gap between biology and Mechatronics. This thesis utilizes this new technology to deliver power wirelessly to wearable electronic devices that are responsible for wireless health monitoring and fitness tracking.

In recent years, smart watches and fitness trackers have become common and recognized as wearable electronic devices as shown in Figure 1.1 (a). They are important for health monitoring and tracking activity, which aid in monitoring the increasing incidents of cancers and chronic diseases like diabetes, cardiac shock and Alzheimer. The future promises even more innovations, given the rapid advancement of nanotechnology that will lead to the development of critical things such as smart clothing, electronic patches connected to the Internet as shown in Figure 1.1 (b). These wearable and implantable electronics require an energy source in order to be functional, and batteries currently act as the most common and

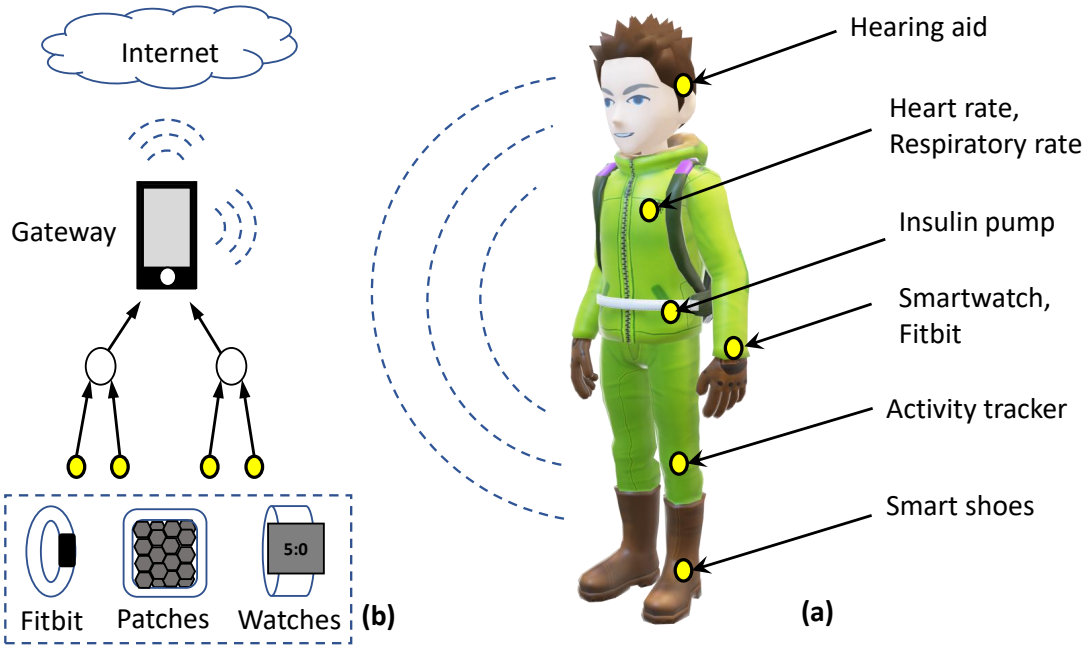

Figure 1.1: Remote monitoring of wearable electronic devices; (a) Health monitoring and fitness tracking devices; and (b) Wearable biomedical sensors.

standard energy source. The problem with batteries is that their energy capacity is limited by the size, which eventually determines both the size and weight of the wearable device. The common solution to this problem that researchers have come up with is to harvest body energy. This can be achieved by using piezoelectric, triboelectric, electromagnetic inertial induction or electromagnetic gear-and-generator actuators. In doing this, mechanical energy from bodily movement from the foot, knee, lower limb hip and/or upper limb converts to electrical energy that powers wearable and implantable electronics. The problem with this approach is the volume of the harvester determines the size of the wearable device. Different parts of the human body also have different energy density. Researchers have turned to wireless power transfer (WPT) technology to overcome these disadvantages. WPT is the technology of transferring the power from the source to the receiver without the help of

wires, and power allows to take different forms (e.g. Electromagnetic, Electrostatic, RF and ultrasound waves). Many WPT modalities are available today and have been thoroughly verified, with the conventional approaches being radio frequency (RF), Induction (Ind), ultrasound (US) and capacitive coupling. Some of these are remotely delivered, while others are delivered locally.

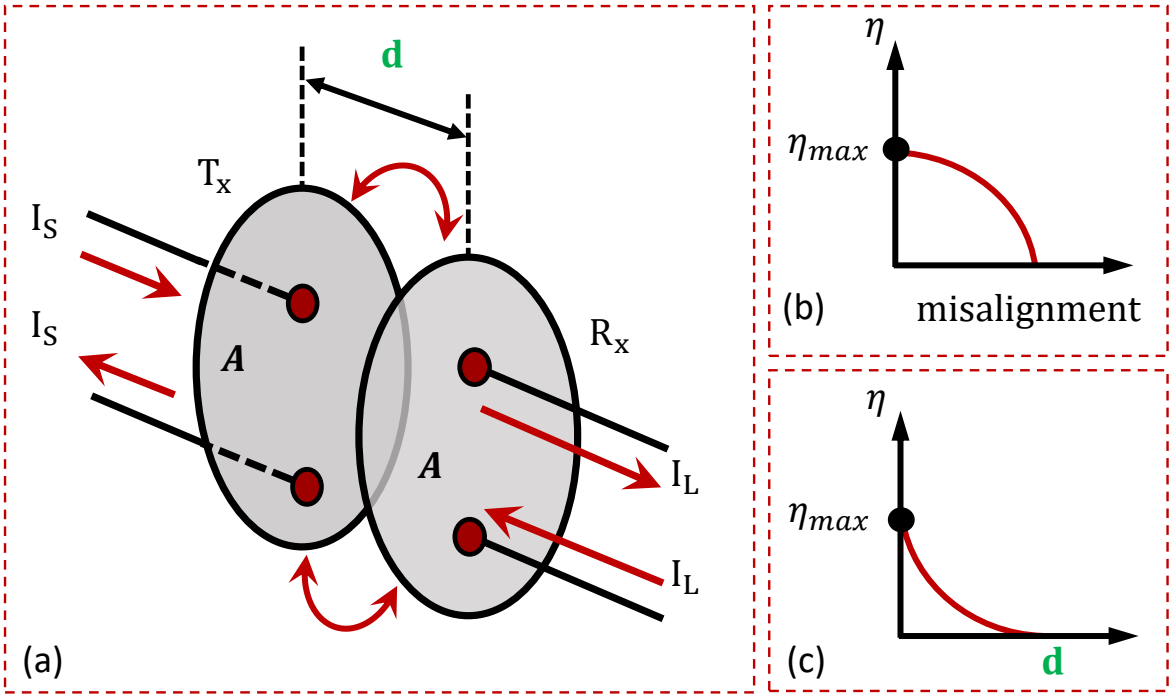

Figure 1.2: Disadvantages of conventional WPT approaches; (a) schematic of mutual coupling of conventional WPT approaches; (b) nonlinearity scaling of the PTE with the cross-sectional area of the transducers; and (c) nonlinearity scaling of the PTE with the relative distance between the transducers.

Conventional approaches for wireless power transfer rely on the mutual coupling (near-field or far-field) of the transmitter (T_x) and receiver transducers (R_x) as shown in Figure 1.2 (a) where the return paths for the source (I_S) and the load (I_L) currents are separate. As a result of that there is a fixed amount of power gets dissipated in the transmitter side and only a fraction of that power gets delivered to the receiver side, and the power transfer efficiency (PTE or η) of these approaches decays non-linearly with both respective alignment

of the transducers and with the relative distance between them as shown in Figure 1.2 (b) and (c) respectively. This thesis investigates an alternate mechanism of WPT that exploits self-capacitances (SC). Self-capacitance is an intrinsic property of any electrically isolated body and arises because fringe electrostatic fields always exist between the body and a theoretical but omni-present, infinitely-large ground plane. In practice, self-capacitances manifest themselves as parasitic elements that either serve as a nuisance during system design or could be exploited for sensing applications. However, self-capacitances can also serve as a return path for displacement currents emanating from a power-source through the external ground back to the source. In my preliminary study using a simple equivalent circuit model, I have shown that when the operational power-budget requirements are in the order of microwatts, the SC-based WPT has significant advantages. These advantages include power transfer-efficiency (PTE), receiver form-factor and system scalability when compared to other WPT approaches. This preliminary result forms the basis for my doctoral research aims to accomplish three specific aims:

1.2 Aims

- Aim 1: Using a cadaver phantom, I investigate the feasibility, advantages and limitations of SC-based WPT and its ability to remotely energize a wearable implant. As a proof-of-concept, I investigate the feasibility of a hybrid telemetry system that harvests microwatts of power from SC-based WPT approach and uses them for back-scattering a radio-frequency signal. In doing so, I demonstrate the utility of this hybrid sensing system for remote sensing in-vivo physiological parameters like temperature.

- Aim 2: In this research objective, I investigate if the SC-based WPT can be scaled to simultaneously power multiple wearable devices attached to multiple bodies that are spatially separated from each other. For this purpose, I exploit the broad-band and high PTE features of the SC-based WPT approach. In doing so, I demonstrate its utility for designing diagnostic mouse cages and smart rooms.

- Aim 3: I investigate sensing and telemetry circuits that can be efficiently energized using the proposed SC-based WPT. Using a minimum number of circuit modules, I exploit the ability of a proportional-to-absolute-temperature (PTAT) circuit to implement rectification, regulation and sensing functions. In addition, I investigate the energy-efficiency and limitations of this approach in order to demonstrate the functionality of the PTAT circuits using prototypes fabricated in a standard CMOS process.

This work invests the SC phenomenon for wireless power transfer for wearable electronics. The self-capacitance-based modal of a human body connected to power source and receiver system is a quasi-static phenomenon. It has been used before for wireless communication, but to the best of our knowledge nobody explored the wireless power transfer using this technology. In this dissertation, I show that when the operational power-budget requirements are in the order of microwatts, a SC-WPT has significant advantages over other WPT methods in terms of the power transfer-efficiency (PTE), receiver form-factor, and system scalability. I present a simple and tractable equivalent circuit model that can be used to study the effect of different parameters on the SC-based WPT. I also demonstrate the feasibility of a hybrid telemetry system where the microwatts of power, which can be harvested from SC-based WPT approach, is used for back-scattering a radiofrequency (RF) signal. This modal is used for remote sensing of in-vivo physiological parameters such as temperature. I have further verified the functionality of the hybrid system using a cadaver mouse

model housed in a cage retrofitted with 915 MHz RF back-scattering antennas. I believe that the proposed remote power-delivery and hybrid telemetry approach would be useful in the remote activation of wearable devices. This could also be useful in the design of energy-efficient animal cages used for long-term monitoring applications. In order to use the remote monitoring applications, the reliable deployment of many wireless sensor nodes is required for remote monitoring applications. These applications include the Internet of Things (IOT) for human body such as monitoring health and tracking fitness. It is likely that these nodes must be deployed for a long period of time. Most current wireless sensors contain replaceable primary or rechargeable batteries as a standard power source, thus making batteries impractical for long term deployment. In this case the wireless power transfer (WPT) is the common candidate solution. The existing approaches of wireless power transfer (WPT) to wearable and implantable electronics include near-field magnetic coupling, far-field power transfer using electromagnetic radiation and airborne ultrasound. Using these approaches, the amount of received or harvested power by the receiver is limited due to the WPT path loss. This existing technology can be limited by a variety of factors including low power transfer efficiency (PTE), a large-size receiver, short distance of power transfer and to the misalignment sensitivity. These shortcomings create a big problem in the context of the Internet of Things (IOT) for the human body because the number of small size wearable and implantable electronics is expected to raise up to several billions of devices in only the next few years. SC-based WPT is considered inherently safe because live tissue behaves as a capacitor, which means the power transfer is approximately lossless and the Specific Absorption Rate (SAR) is low.

So far, we have been discussing the issue of design and implementation of the wireless power transfer, but we have not yet touched the other side which is the power consumer (i.e. the receiver). By improving the efficiency of the receiver device, we have improved the power

transfer efficiency to a wide extent. Making the receivers or sensor nodes more power efficient is another challenge, as it is always required to reduce the power consumption of these devices as much as possible while keeping them functional. In the usual case, the wearable electronics (sensors, actuators and/or receivers) are made of electronic devices (Transistors, diodes, capacitors, resistors.... etc.). Thus, there is always a trade-off associated with their performance, in the sense that reducing power consumption, for example, reduces sensitivity. In order to design and implement an acceptable device, there must be a compromise depending on the application it will be used for: reduced power will reduce the sensitivity, while high sensitivity will require higher power.

This study has neglected most of the parasitic capacitances that might exist due to their non-significant influence on the total power consumption.

1.3 Organization of the Thesis

This thesis presents Self Capacitance based Wireless Power Transfer for Wearable Electronics: Theory and Implementation. It has been organized in the form of chapters that have been described below.

In chapter 2, the modeling and investigation of the self-capacitance based wireless power transfer efficiency is presented and compared with the conventional modalities, with the help of analytical results and discussion. Using a simple case-study, I examine different factors that determine the system PTE and compare the results with other WPT methods. I present experimental results using a mouse cadaver which has been used to verify the SC model and I also demonstrate the feasibility of a hybrid telemetry system for continuous monitoring

in-vivo temperature variations. I conclude the chapter with a discussion of limitations and extensions of the SC-based WPT method.

In Chapter 3, I present the extension of the SC-WPT to a wireless power broadcasting (WPB) framework that can simultaneously power multiple devices worn by multiple human subjects. Experimentally, I investigate the performance and design trade-offs involved when designing a self-capacitance based WPB system.

In Chapter 4, A system level architecture of a compact and energy-efficient instrumentation as receivers that can operate over a wide range of input signal using PTAT reference circuit are presented and compared with the conventional receivers showing all the necessary trade-offs. I briefly introduce a standard PTAT based ultrasound receiver circuit and describe the implementation of the receiver in a standard CMOS process. Then I describe an experimental setup that have been used to validate the fabricated prototype and along with the measured results. Finally, we summarizes the chapter with some discussion about future work.

In Chapter 5, A expected extension for the SC-WPT for both wearable and implantable electronic devices on different kind of substrates that are electrically isolated is discussed. In addition, some common examples of wearable/implantable electronic devices for substrate computing (sensing and communication) are presented, and the conventional methods for their powering technique with their limitations are explored. I conclude the chapter showing some important points that need to be taken care of in the future.

The research work is summarized in Chapter 6. Achievements are listed, and suggestions for future work are presented.

Chapter 2

Exploiting Self-Capacitances for Wireless Power Transfer

In this chapter, I present the the phenomenon of self-capacitance (SC) of any electrically isolated conductors, and the way I exploit it for wireless power transfer (WPT) to wearable electronic devices when the operational power-budget requirements are in the order of microwatts. I experimentally verify the validity of the self-capacitance equivalent circuit using a cadaver mouse model and a human head phantom setup through the demonstration of the feasibility of a hybrid telemetry system, where the microwatts of power that can be harvested from SC-based WPT approach is used for back-scattering a radio-frequency signal and is used for remote sensing of in-vivo physiological parameters like temperature. The results of this chapter are based on [7].

2.1 Introduction

In practice, self-capacitances manifest themselves as parasitic elements that either serve as a nuisance during system design or could be exploited for sensing applications [8]. However, self-capacitances can also serve as a return path for displacement currents emanating from a power-source through the external ground back to the source, as illustrated in Figure 2.1 (a)

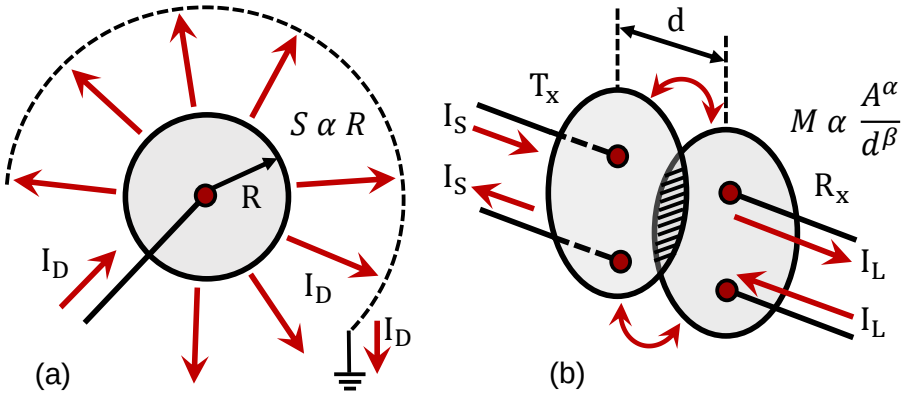

Figure 2.1: Different WPT approaches based on: (a) self-capacitance where the displacement current I_D flows back to the source through a fictitious ground; and (b) mutual coupling where the return path for the source I_S and the load I_L currents are separated from each other.

using an electrically isolated sphere. Since the path traversed by the displacement currents could be long, this attribute has been exploited in literature for designing communication links in wireless body-area-network (WBAN) [9–15]. In this work, we explore the feasibility and limitations of using self-capacitances for wireless power transfer (WPT). Conventional wireless power-delivery techniques [16,17] rely on the mutual coupling between the source and receiver transducers, as illustrated in Figure 2.1 (b), and therefore the system power-transfer efficiency (PTE) is determined by the cross-sectional area, the relative alignment and the distance between the transducers. As shown in Figure 2.1 (b), the return path for the source transducer current (I_s) is separated from the return path of the load transducer current (I_L), as a result, the source dissipates a fixed amount of power and only a fraction of the source power gets coupled to the load. In the case of self-capacitance, the return path for the source current only exists through the load and through the parasitic elements, which should lead to a high power-transfer efficiency (PTE). Also, since self-capacitances scale linearly with dimensions, we will show in this thesis the maximum received power also scales linearly with the receiver form-factor. This is in comparison to inductive WPT approach [18–21],

PTE scales as a cube of the source/receiver coil dimensions. For ultrasound-based and other far-field WPT approaches [6, 22–24], the transfer-efficiency scales as the square of the transducer dimensions. Specifically, we show in this thesis, that for power-budgets less than 10 μW, SC-based WPT offers significant advantages compared to other WPT methods, in terms of powering distances, transducer form-factor and system scalability. Additionally, the SC-based approach is robust to transducer alignment artifacts, which presents a significant challenge for other WPT modalities. The key contributions of this work in this chapter can be summarized as follows:

- A self-capacitance based simple and tractable wireless power-delivery model that can be used for system optimization and comparison with other WPT methods. Compared to the previously reported finite-element approaches [12,14] to model body-capacitance, the self-capacitance based approach is analytic and can be applied to complex geometries and substrates.
- Experimental verification of the self-capacitance based power-delivery using a cadaver mouse model.
- Experimental demonstration of a hybrid telemetry system based on RF back-scattering that is energized using the self-capacitance based wireless power transfer.

2.2 Self-capacitance based Power-transfer Model

Before presenting a more general SC-based WPT model that could be applied to complex geometries and substrates, we present a simple lumped-parameter model that can be used

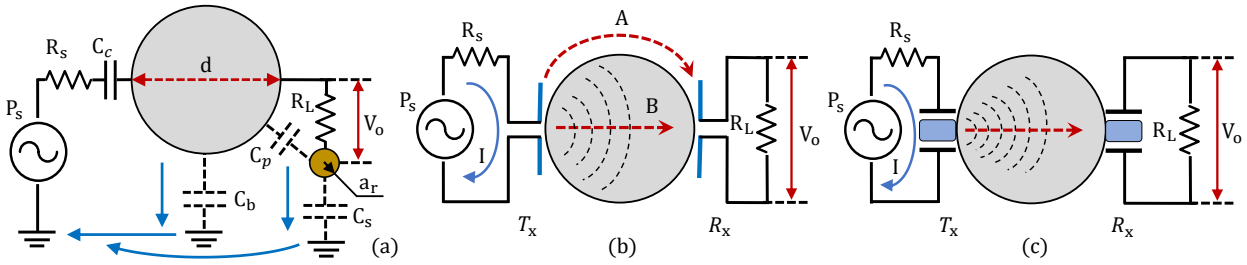

Figure 2.2: A simple case study used for comparing different WPT approaches based on: (a) Self-Capacitances; (b) near and far-field radio-frequency coupling; and (c) ultra-sonic/acoustic coupling.

for optimization and for comparison with other WPT techniques. The model as shown in Figure. 2.2 (a)-(c) uses a homogeneous sphere of diameter d as a transmission substrate or as a wave-guide, as described in [25]. In each of these cases, the objective is to transfer power from the source connected at one end of the substrate, to the load resistance R_L connected to the other end of the substrate. The power-transfer efficiency (PTE) η that has been used for comparison is defined as:

$$\eta = \frac{P_r}{P_s} \tag{2.1}$$

where P_r is the power dissipated at the resistor R_L and P_s is power dissipated at the source.

In the SC-based WPT model, as shown in Figure 2.2 (a), the self-capacitance of the substrate is modeled as C_b. The coupling capacitance C_c and the resistance R_s is used to model the interface between the power-source to the load R_L. As shown in Figure 2.2 (a), the respective displacement currents flow-back to the power source through C_b and through the self-capacitance of the load, modeled using a sphere of radius a_r. If $d \gg a_r$, then the self-capacitance of the load C_s can be approximated as [26]:

$$C_s = 4\pi\epsilon a_r \sum_{n=1}^{\infty} \frac{\sinh(\ln(D + \sqrt{(D^2-1)}))}{\sinh(n \ln(D + \sqrt{(D^2-1)}))} \geq 4\pi\epsilon a_r \tag{2.2}$$

In the expression, the ϵ is the dielectric constant of the medium and $D = (d/a_r)$ where d is the distance between the load and the substrate. Irrespective of the magnitude of the ratio D, the self-capacitance C_s can be lower-bounded by the $4\pi\epsilon a_r$, which represents the worst-case self-capacitance. We will use this simpler, worst-case expression to estimate the minimum power that can be delivered to R_L. In the following section we are going to apply the standard circuit analysis technique to Figure 2.2 (a) to derive the expression for the efficiency of power transfer and the power P_r dissipated at the load R_L.

2.2.1 Derivation of PTE and received power for SC-based WPT

For the circuit shown in Figure 2.2 (a) denote:

$$Z_s = \frac{1}{j\omega C_s}$$
$$Z_b = \frac{1}{j\omega C_b}$$
$$Z_c = \frac{1}{j\omega C_c}$$

Then,

$$V_o = Vs\frac{R_L}{R_L + Z_s}\frac{(R_L + Z_s) \parallel Z_b}{(R_L + Z_s) \parallel Z_b + (Z_c + R_s)}$$

$$= \frac{R_L Z_b V_s}{(Z_c + R_s)(R_L + Z_b + Z_s) + Z_b(R_L + Z_s)} \tag{2.3}$$

which leads to

$$P_r = \frac{{V_o}^2}{R_L} =$$

$$\frac{R_L V_s^2}{|(\frac{C_b}{C_c} + jR_sC_b\omega)(R_L - j\frac{C_s+C_b}{C_sC_b\omega}) + (R_L - j\frac{1}{C_s\omega})|^2} =$$

$$\frac{R_L {V_s}^2}{\left(R_L(1+\frac{C_b}{C_c}) + R_s(1+\frac{C_b}{C_s})\right)^2 + \left(R_LR_sC_b\omega - \frac{C_c+C_b+C_s}{C_cC_s\omega}\right)^2} \tag{2.4}$$

$$Z_{in} = (Z_c + R_s) + \frac{Z_b(R_L + Z_s)}{(R_L + Z_b + Z_s)} \tag{2.5}$$

$$P_s = \frac{{V_s}^2}{|Z_{in}|} = \frac{{V_s}^2}{|(Z_c + R_s) + \frac{Z_b(R_L+Z_s)}{(R_L+Z_b+Z_s)}|} =$$

$$\frac{{V_s}^2\left[R_L + R_L^2R_s(C_b\omega)^2 + R_s(1+\frac{C_b}{C_s})^2\right]}{\left(R_L(1+\frac{C_b}{C_c}) + R_s(1+\frac{C_b}{C_s})\right)^2 + \left(R_LR_sC_b\omega - \frac{C_c+C_b+C_s}{C_cC_s\omega}\right)^2} \tag{2.6}$$

The PTE (η) can then be estimated according to equation 2.1 as

$$\eta = \frac{R_L}{R_L + R_L^2R_s(C_b\omega)^2 + R_s(1+\frac{C_b}{C_s})^2}$$

$$\eta = \frac{1}{1 + R_LR_s(4\pi^2\epsilon_0 fd)^2 + \frac{R_s}{R_L}(1+\frac{d}{2a_r})^2} \tag{2.7}$$

Figures 2.3 and 2.4 plot the efficiency (η) and received power (P_r) for different values of R_L, R_s, a_r, d and f. The results show that η and P_r vary monotonically with respect to R_s, a_r, d and f, except for the load resistance R_L. Thus, the expression in equation 2.7 can be maximized with respect to R_L by setting:

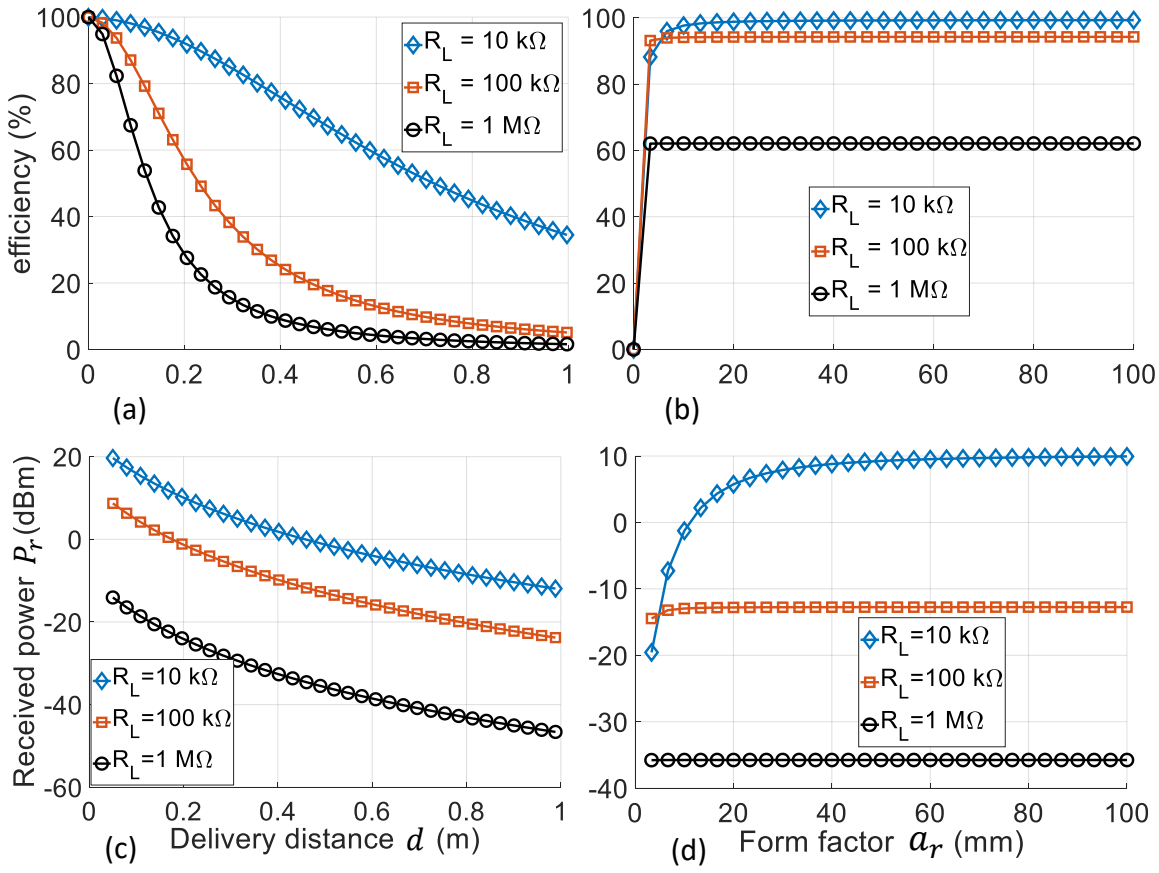

Figure 2.3: Estimated PTE (a)-(b) and received power P_r (c)-(d) as a function of delivery distance d, form factor a_r, frequency f and source resistance R_s respectively; (a) and (c) when $f = 10\ MHz$, $a_r = 10\ mm$ and $R_s = 5\ \Omega$, (b) and (d) when $f = 10\ MHz$, $d = 0.1\ m$ and $R_s = 5\ \Omega$.

$$\frac{\partial \eta}{\partial R_L} = 0, \quad R_L \approx \frac{1}{8\pi^2 \epsilon_0 f a_r} = \frac{1}{C_s \omega}$$

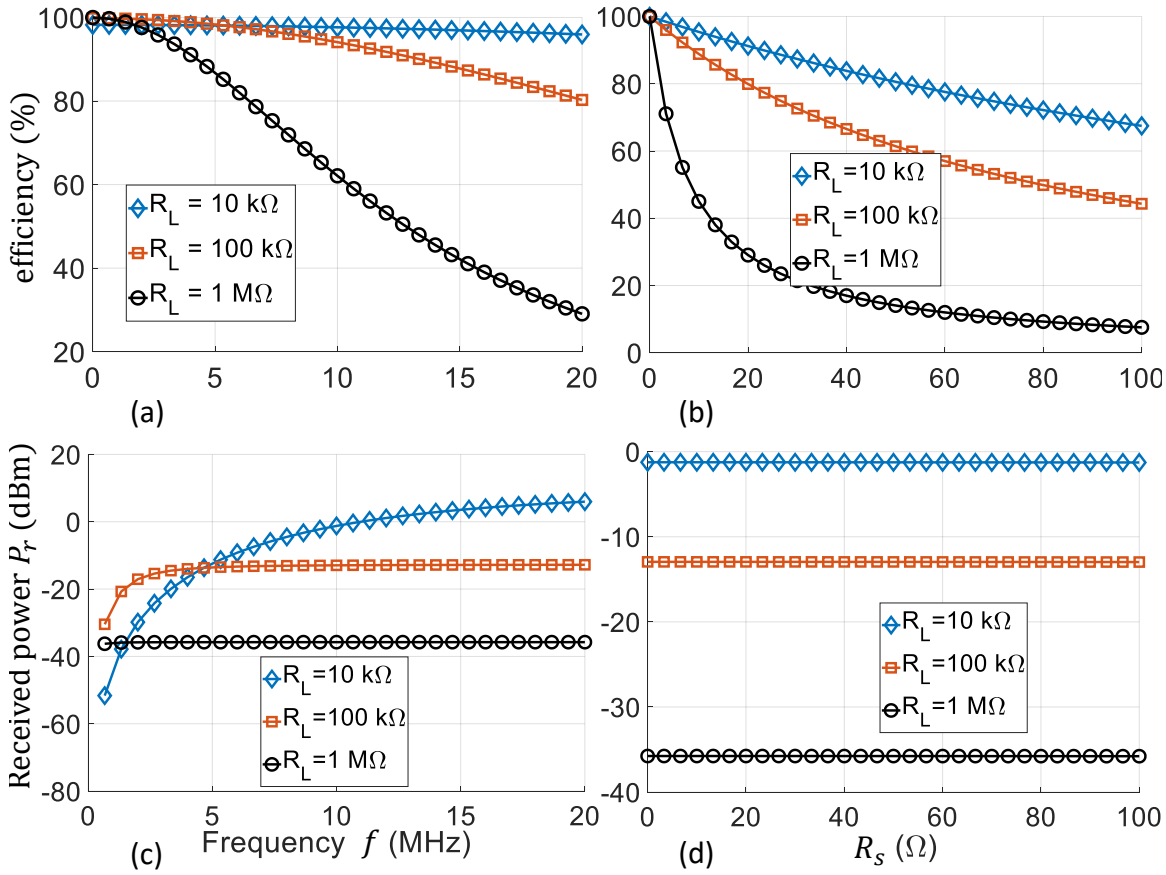

Figure 2.4: Estimated PTE (a)-(b) and received power P_r (c)-(d) as a function of delivery distance d, form factor a_r, frequency f and source resistance R_s respectively; (a) and (c) when $d = 0.1\ m$, $a_r = 10\ mm$ and $R_s = 5\ \Omega$, and (b) and (d) when $f = 10\ MHz$, $a_r = 10\ mm$ and $d = 0.1\ m$.

which leads to

$$\eta_{max} = \frac{1}{1 + 8\pi^2 \epsilon_0 f R_s (a_r + d + \frac{d^2}{2a_r})} \tag{2.8}$$

This maximum efficiency is achieved for the condition $R_L = \frac{1}{C_s\omega}$ and the corresponding power dissipated by the load R_L is given by :

$$P_{r,max} = \frac{C_s\omega {V_s}^2}{2\left(\frac{C_c+C_b}{C_c}\right)^2} = \frac{4\pi^2\epsilon_0 f a_r {V_s}^2}{\left(1+\frac{2\pi\epsilon_0 d}{C_c}\right)^2} \tag{2.9}$$

Note that in equation 2.9 we have assumed $R_s = 0$ since P_r is monotonic with respect to R_s.

The expressions in equations 2.8 and 2.9 have been used for comparing the PTE of the SC-based approach with other WPT approaches, and is summarized in Figures 2.5 and 2.6. For other WPT methods, we have used standard mathematical models as reported in literature [27–33]. Note that in the case of RF-based WPT, as shown in Figure 2.2 (b), the energy is delivered over the air, rather than through the substrate, where as in the case of inductive and ultrasound based WPT the power is delivered through the medium, as shown in Figure 2.2 (b) and (c). The expressions for the power transfer efficiency η for each of the WPT approaches (Ind: inductive, RF: far-field radiofrequency and US: ultrasound) are given by:

$$\eta = \begin{cases} Q_r Q_t \eta_r \eta_t \frac{{a_r}^3 {a_t}^3 \pi^2}{({d^2}+{a_t}^2)^3} & Ind \\ \frac{G_r G_t}{4}\left(\frac{2a_r}{\pi d}\right)^2 & RF \\ \frac{{a_r}^2}{{a_t}^2} e^{-2\alpha f^\beta d} & US, \end{cases} \tag{2.10}$$

where

Q_t = Quality factor of the transmitter coil.

Q_r = Quality factor of the receiver coil.

η_t = efficiency of the transmitter coil.

η_r = efficiency of the receiver coil.

a_t = radius of the transmitter.

a_r = radius of the receiver.

d = Distance between transmitter and receiver.

G_t = Gain of transmitter antenna.

G_r = Gain of receiver antenna.

f = frequency of US wave (Hz).

α = Attenuation Parameter ($neper/mMHz^{-\beta}$).

β = Attenuation Coefficient.

The respective parameters used for this comparative study are summarized in Table 2.1. Figure 2.5 shows that as the transmission distance increases, the SC-based WPT demonstrates a superior PTE compared to the other WPT techniques. In this comparison, the diameter of the receiver transducer (coil or antenna size) was chosen to be $a_r = 10\ mm$. In Figure 2.6 we compare the PTE for different WPT approaches as the transducer form-factor is varied while keeping the delivery distance constant at $d = 0.1\ m$. The results again show SC-based WPT demonstrates a superior PTE compared to other approaches. Note that for the other WPT approaches, the transfer frequency needs to be adjusted to ensure ideal impedance matching between the antenna/transducer to the substrate. Whereas, SC-based WPT is broad-band in nature (as will be verified in our experimental results), and therefore does not require any frequency adjustment when the transducer size or alignment changes.

Table 2.1: Parameters used for comparing different WPT methods [6].

Property	Description	Value
C_c	Source coupling capacitance	10 pF
α	Attenuation parameter	0.086 ($neper/mMHz^{-\beta}$)
β	Attenuation Coefficient	1.5
G_t	Gain of Tx antenna	7.5 dB
G_r	Gain of Rx antenna	7.5 dB

2.2.2 Generalization of Self-capacitance based Model

Using the self-capacitance based modeling, we can extend the framework to substrates with arbitrary shapes and comprising of heterogeneous materials. The approach is illustrated here using a mouse model as a substrate and is shown in Figure 2.7 (a). However, the approach can be easily extended to other animal models as well. As shown in Figure 2.7 (a), the power source is capacitively coupled (through capacitance C_c) to the tail of the mouse and the energy harvester is connected to one of the fore-limbs. The harvester in this example comprises of a rectifying diode bridge which drives the load resistance R_L and the reference terminal is connected to a floating-electrode. The self-capacitance of the mouse body is estimated by first segmenting different regions of the substrate and approximating each region using a simple shape, for example a sphere or a cylinder, as shown in Figure 2.7 (b). The closed-form expressions for self-capacitances in each of these simple 3-dimensional shapes are well documented in literature [26] and can be estimated as a function of their respective dimensions. For instance, the self-capacitance of a cylindrical shape is estimated as $C_{cylinder} = \frac{2\pi\epsilon h}{ln(\frac{r_2}{r_1})}$ where h is the length of cylinder, r_1 and r_2 are the inner and outer radius of the cylinder and ϵ is the permittivity of the substrate. Similarly, for a spherical

shape (modeling the head), the self-capacitance is given by $C_{spherical} = 4\pi\epsilon r_1$. With respect to the energy-harvester, each of these self-capacitances (C_{b1}, C_{b2}, C_{b3}, C_{b4}, C_{b5} and C_{b6}) can be considered to be in parallel to each other (independent path for displacement currents to flow-back to the source). If we ignore the capacitive cross-coupling between these different shapes, all of these elements could be lumped together into a single capacitance C_b to form the equivalent circuit shown in Figure 2.7 (c). Figure 2.7 (c) also shows a cross-coupling capacitance between the floating-electrode and the body self-capacitance. For all practical purposes if the size of the floating-electrode is small, the coupling capacitance could be ignored. The equivalent circuit in Figure 2.7 (c) also shows a lumped resistance R_s that models the resistivity between the coupling electrode and the harvester. In its exact form, R_s and C_b would comprise of distributed elements, but as we will show in our experimental results, $R_s \approx 0$, leading to the lumped equivalent circuit shown in Figure 2.7 (c).

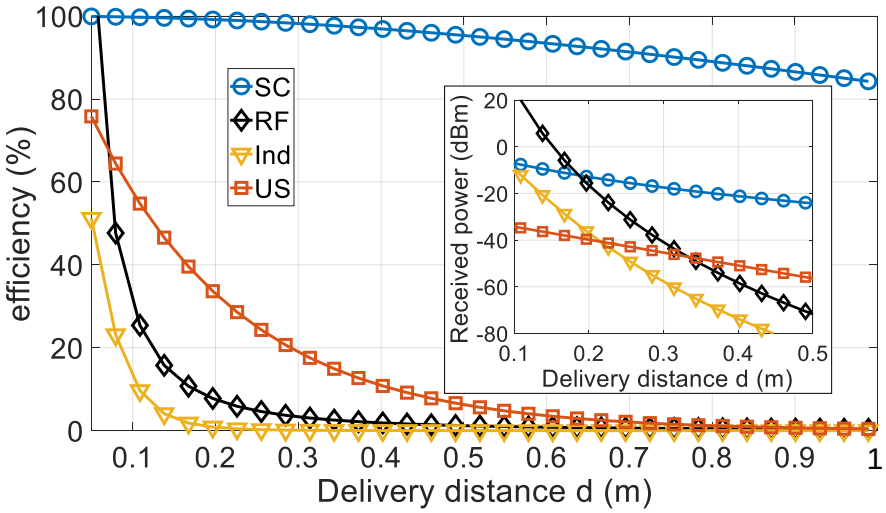

Figure 2.5: Comparison of PTE and received power P_r for different WPT methods when the receiver transducer dimension is chosen to be $a_r = 10\ mm$, $f = 5\ MHz$ and $R_s = 5\ \Omega$.

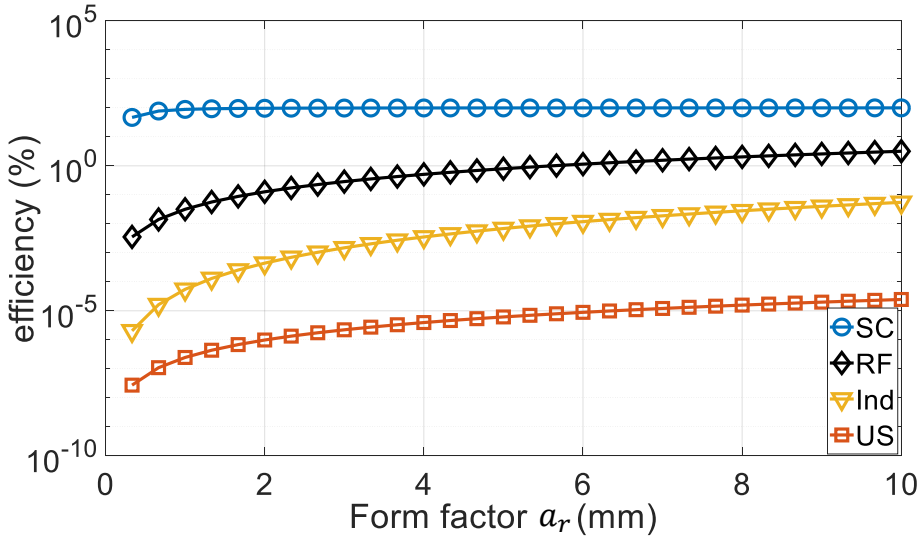

Figure 2.6: Comparison of PTE for different WPT methods when the transmission distance n is chosen to be $d = 0.1\ m$, $f = 5\ MHz$ and $R_s = 5\ \Omega$.

2.3 Experimental Results

2.3.1 Characterization of SC-based power delivery

In the first set of experiments, we used a mouse cadaver model to characterize the SC-based power delivery. The experimental setup is shown in Figure 2.8 (a) where the cadaver is kept electrically insulated from environmental factors to ensure a capacitive coupling between the body and return path (external ground in this case). The material and methods for storing and reviving the cadaver in this experiment is described in Appendix B. First, we used an impedance analyzer (Omics Bode 100 vector network analyzer) to measure the equivalent impedance between the source and the harvester. The resulting smith-chart corresponding to the frequency of 10 MHz is shown in Figure 2.8 (b) which shows that the substrate impedance is predominantly capacitive. This is true even when a resistive load is connected to the energy-harvester, as the body self-capacitance is much larger than the self-capacitance

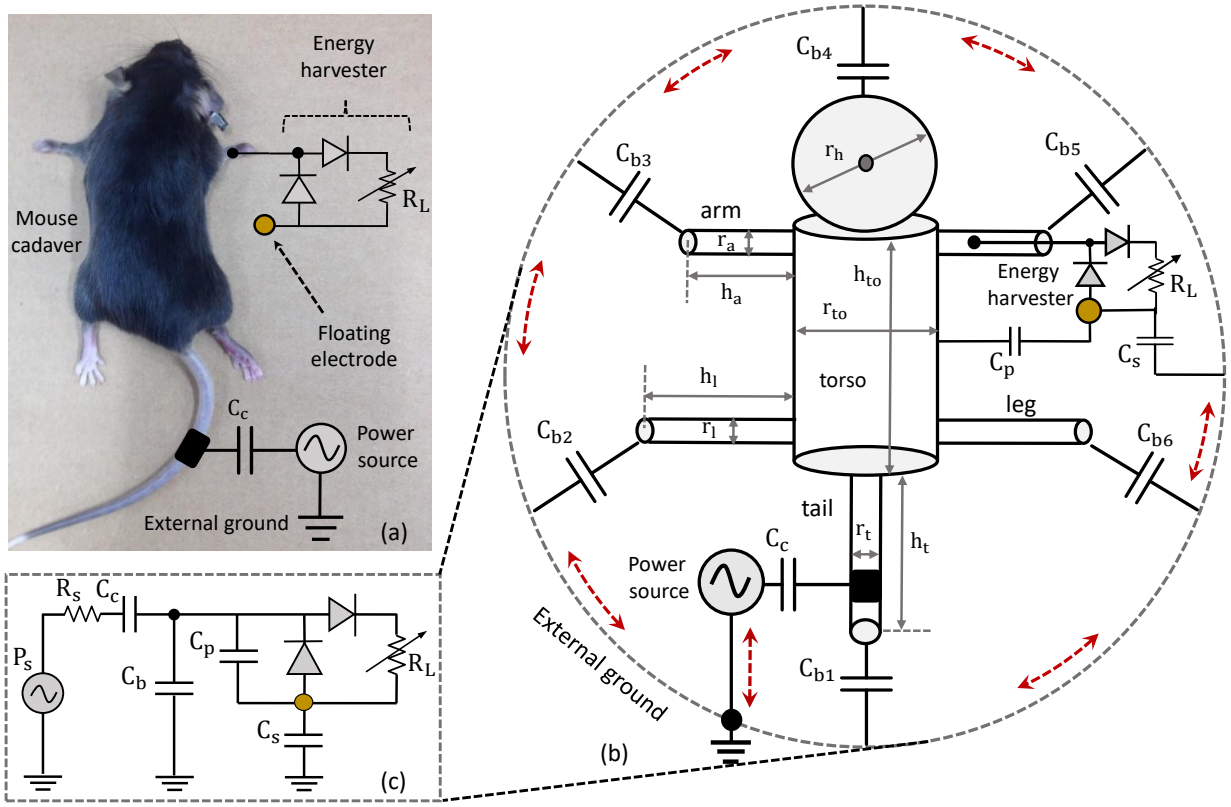

Figure 2.7: Generalization of self-capacitance modeling to substrates with complex geometries: (a) Case study based on a mouse cadaver model; (b) Approximation of the self-capacitance by decomposing different segment of the substrate into simple shapes; and (c) lumped-parameter equivalent circuit for SC-based WPT to a simple harvester circuit

of the floating-electrode. Next, a modulating energy source (an earth-grounded Tektronix DG4102 function generator) is capacitively coupled to the tail of the cadaver. The power source is programmed to generate a sinusoidal wave at a potential of 20 $V_{\mathrm{pk-pk}}$ and at variable frequencies. The harvester comprised of a single-stage diode bridge shown in Figure 2.8 (a) constructed using two Schottky diodes. The output of the diode bridge was measured using a battery-powered voltmeter with no direct conductive path to ground. Also, connected to the diode-bridge is a load resistor whose magnitude could be varied. Note that the other end of the diode bridge forms the floating-electrode providing a return path for the load-current to the source.

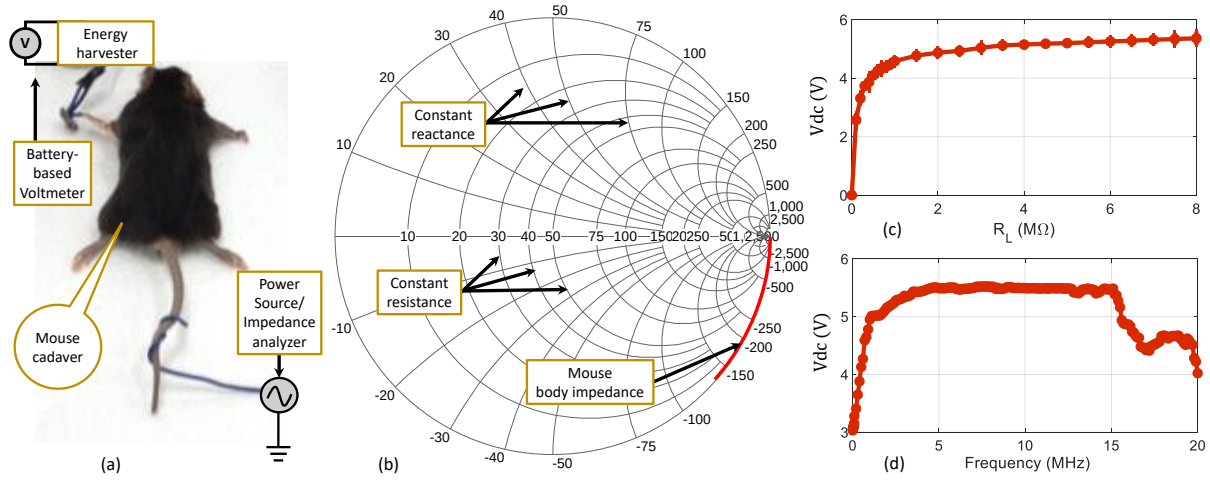

Figure 2.8: Experimental characterization of the cadaver mouse as a substrate: (a) Experimental setup; (b) Measured Smith-chart showing that the substrate is predominantly capacitive; (c) Measured voltage at the output of the harverster at an input frequency of $f = 10\ MHz$; and (d) Broad-band response of the SC-based WPT for a load $R_L = 1\ M\Omega$.

Figure 2.8 (c) shows the measured voltage across different the load-resistance as the resistance value is varied. For this experiment the source voltage was programmed to 20 V_{pk-pk} with an operating frequency of 10 MHz. Based on the plot in Figure 2.8 (c), one can estimate the delivered power to be approximately 45 μW. As described in equation 2.9, the delivered power could be increased by increasing the size of the coupling capacitance or by increasing the size of the floating-electrode's self-capacitance. In the next experiment, the voltage across the load $R_L = 1\ M\Omega$ was measured for different operating frequencies. The result is shown in Figure 2.8 (d), which shows a broadband response within the frequency range of $1-15\ MHz$. This result can be understood using the equivalent circuit model shown in Figure 2.7 (c). The input coupling capacitor C_c blocks low-frequencies where as the coupling capacitor C_p bypasses high-frequencies to the load R_L. Also, at higher frequencies the substrate itself acts as an antenna [10] and hence manifests as a radiation resistance in parallel with the load resistance R_L. environment.

2.3.2 Mouse-cage and Hybrid Telemetry Experiments

In this section, we demonstrate that the beneficial features of the SC-based WPT can be exploited for designing power-efficient animal cages for long-term and ambulatory monitoring applications. Previous designs of smart animal cages have used inductive coils embedded inside the flooring of the cage [34]. Since the SC-based WPT operates by capacitively coupling an energy source through the body of the animal, the insulated base of the cage can be directly used as the coupling capacitor. This is shown in Figure 2.9 (a), where the power is coupled through different body segments as the animal is moving around in the cage. Note that the series resistance of a thick conductive underlay R_s could be very small (in the orders of $2.65 * 10^{-8}$ $\Omega.m$), which implies that the PTE according to equation 2.8 could be close to 100%. However, due to the size limitations on the floating-electrode self-capacitance, only microwatts of power could be delivered to any ex-vivo part of the animal body. Here, we show that this limitation could be overcome by using a hybrid telemetry approach as shown in Figures 2.9. The power harvested from the SC-based WPT approach is used to modulate the impedance of an RF antenna on the device S, in Figure 2.9 (a). This modulation is then received as a backscattered RF signal emitted by the transmitter antenna T_x and received by the receiver antenna R_x. In literature, this approach has been effectively used for backscattering WiFi signals [35,36] and for biotelemetry applications [37]. Two examples of the biotelemetry interface is shown in Figures 2.9 (b) and (c). In both the designs, a low-power oscillator T is used to switch the impedance of the antenna B. The frequency of the oscillator and hence the modulation frequency of the antenna is determined by a resistor R_L whose value changes according to the sensor signal being sensed. Thus, the sensor signal is effectively backscattered on the signal received by the receiver R_x. Figure 2.9 (b) represents a battery powered variant of the telemetry interface and has been used for

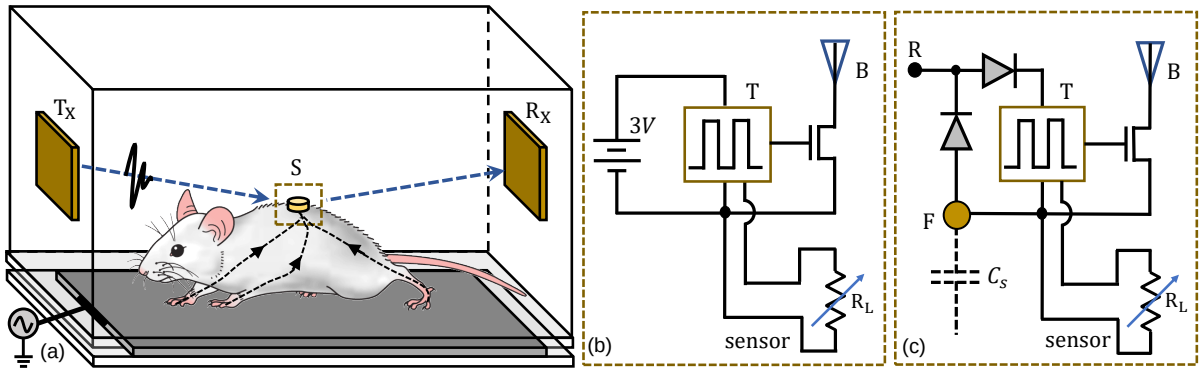

Figure 2.9: Hybrid telemetry experimental setup: (a) The insulated underlay of the cage is powered and delivers power to an implant or a head-stage that communicates with the receiver using RF-backscattering; (b) Schematic of a battery-based backscattering interface used as a control; and (c) Schematic of the sensing/telemetry interface powered using SC-based WPT.

control experiments, where as Figure 2.9 (c) represents the variant that is powered using SC-based WPT approach.

The experimental setup used to verify the operation of the hybrid telemetry system is shown in Figure 2.10 (a). Similar to the previous experiments, a mouse cadaver has been used to emulate the animal in a diagnostic cage. The bottom overlay of the cage, as shown in Figure 2.10 (b) is designed using an Aluminum sheet (6 Ω) that is sandwiched between two plexiglass insulators. The sheet is then connected to one of the outputs of a power source, as shown in Figure 2.10 (c). Two 915 MHz ultra-high-frequency (UHF) antennas, T_x and R_x were used for backscattering. Both the antennas were controlled by a Software Defined Radio (Ettus Research USRP N210) and was programed to transmit a carrier frequency and to receive the backscattered signal. The mouse cadaver was implanted with a device that can monitor variations in temperature at target locations in-vivo and then backscattering the measurements to the receiver R_x. The surgical set up is shown in Figure 2.11 (a) and the surgical protocol is described in Appendix B. The two types of implants (powered using a battery and powered using SC-based WPT) is shown in Figure 2.11 (b) and (c).

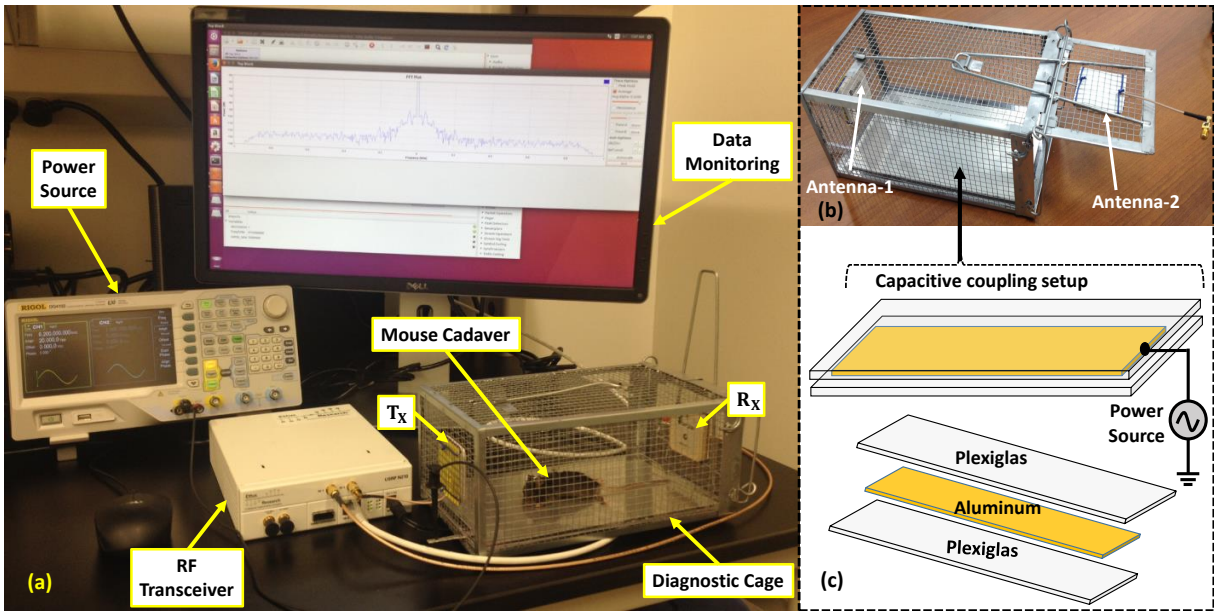

Figure 2.10: Experimental setup using a cadaver mouse housed in a diagnostic cage retrofitted with the backscattering RF antennas; (a) Setup for measuring the backscattering signal; (b) wireless diagnostic cage; (c) schematic for SC-based WPT.

The temperature sensor was implemented using a (NCP15WM474E03RC) thermistor whose temperature sensitivity is given by (5.1 $kOhm/°C$). The tip of the thermistor was surgically implanted at a depth of 3 cm. The output of the thermistor was used to bias a TS3006 timer that implemented the backscatter according to the schematic described in Figure 2.9. The backscatter was designed to operate on a single-supply voltage range between 1.55 V and 5.25 V with typical supply currents remaining below 2.4 μA. Figure 2.12 (a) shows the spectrum of the backscattered signal received at R_x, when centered around the 915MHz RF carrier. To locally heat the tissue we used another piece of wire was inserted in proximity to the area where the tip of the thermistor was located. Heat was applied to the other end of the wire externally which would lead to change in resistance at the output of the thermistor. This in turn would change the modulation frequency (labeled as A) in the received spectrum. Figure 2.12 (b) plots the change in the modulation frequency as a function of the temperature, measured using the SC-based implant. The result shows a monotonic

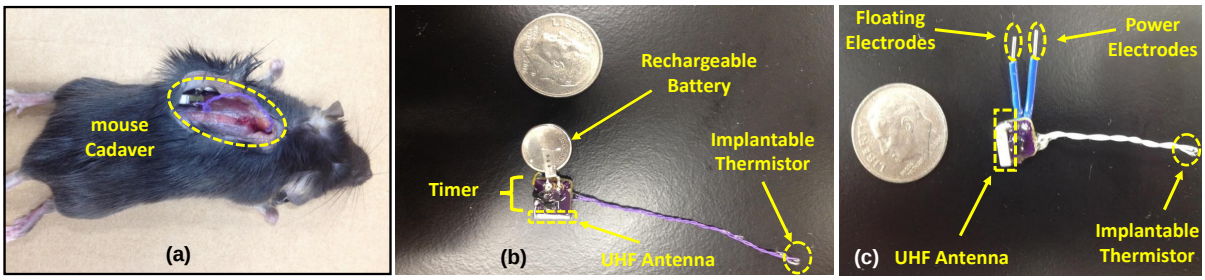

Figure 2.11: Assembly and surgical implantation of the sensor/energy-harvester/back-scattering circuit in the cadaver mouse model: (a) implantation of the temperature sensor at a specific location in-vivo; (b) Battery-powered control prototype; (c) Proof-of-concept prototype powered using SC-based WPT.

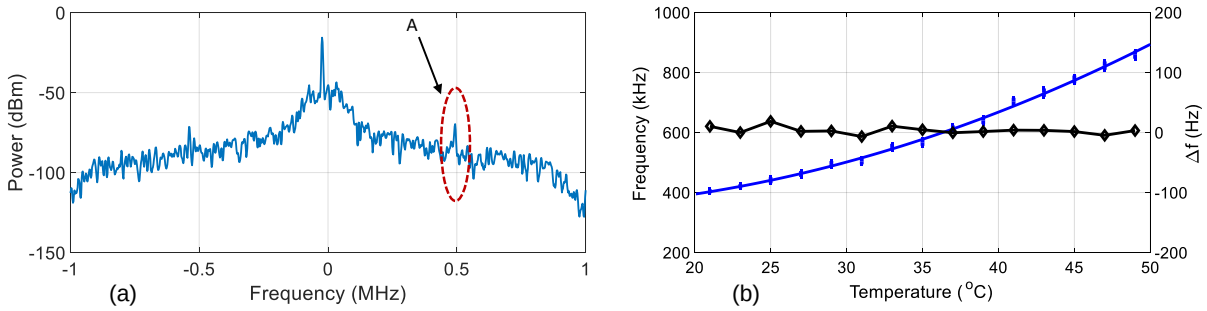

Figure 2.12: Measured results demonstrating the proposed hybrid telemetry approach; (a) Backscattered spectrum showing the data modulation peak corresponding to a specific in-vivo temperature; (b) Measured change in frequency as a function of temperature and the comparison of the measured result with the output of the control (battery-powered prototype).

response in the frequency shift with respect to temperature with less than 1% variance between the three trials. Thus, by measuring the frequency shift one could accurately infer the magnitude of the in-vivo temperature. The average measured response is compared against the average response measured from the battery-powered implant. The result shows that the error between the two outputs Δf is negligible.

Table 2.2: comparison of the proposed self-capacitance WPT and most recent work.

	Modality	Form Factor	Distance	Efficiency
[38]	Ind	$a_r = 40\ mm$ x $h = 115\ mm$	70 mm	70 %o
[39]	Ind	$a_r = 50\ mm$	120 mm	72 %
[40]	Ind	$a_r = 33\ mm$	6 mm	58.6 %
[41]	Ind	20 mm x 50 mm	N/A	15.92 %
[42]	US	N/A	7 mm	25 %
[43]	Rad	$a_r = 2\ mm$	40 mm	0.04 %
[44]	Cap	$a_r = 60\ mm$	7 mm	66 %
[45]	Cap	$a_r = 83\ mm$	15 mm	2.6 %
This work	Cap	$a_r = 10\ mm$	70 mm	90 %

2.3.3 Cadaver Material and Methods

As described earlier, two different experiments have been conducted on the mouse cadaver; one the first by surgically subcutaneously implanting a battery-based electronic circuit within the mouse body. The battery and circuit were placed subcutaneously along the dorsum of the back. The thermistor was implanted underneath the interscapular adipose tissue. The incision was closed with glue to prevent exposing the implant in order to do the measurements. We used the measured temperature data of the mouse tissue as a reference for the next second experiment in which the battery-less wearable electronic circuit that harvests the energy through the self-capacitance proposed was implemented. Three dead mice cadavers have were used to statistically verify the results and compare that with the reference data. There was no direct contact between the mouse body and the electric power source, but instead we used an insulated wire and wrapped it around the mouse tail to form a coupling capacitor.

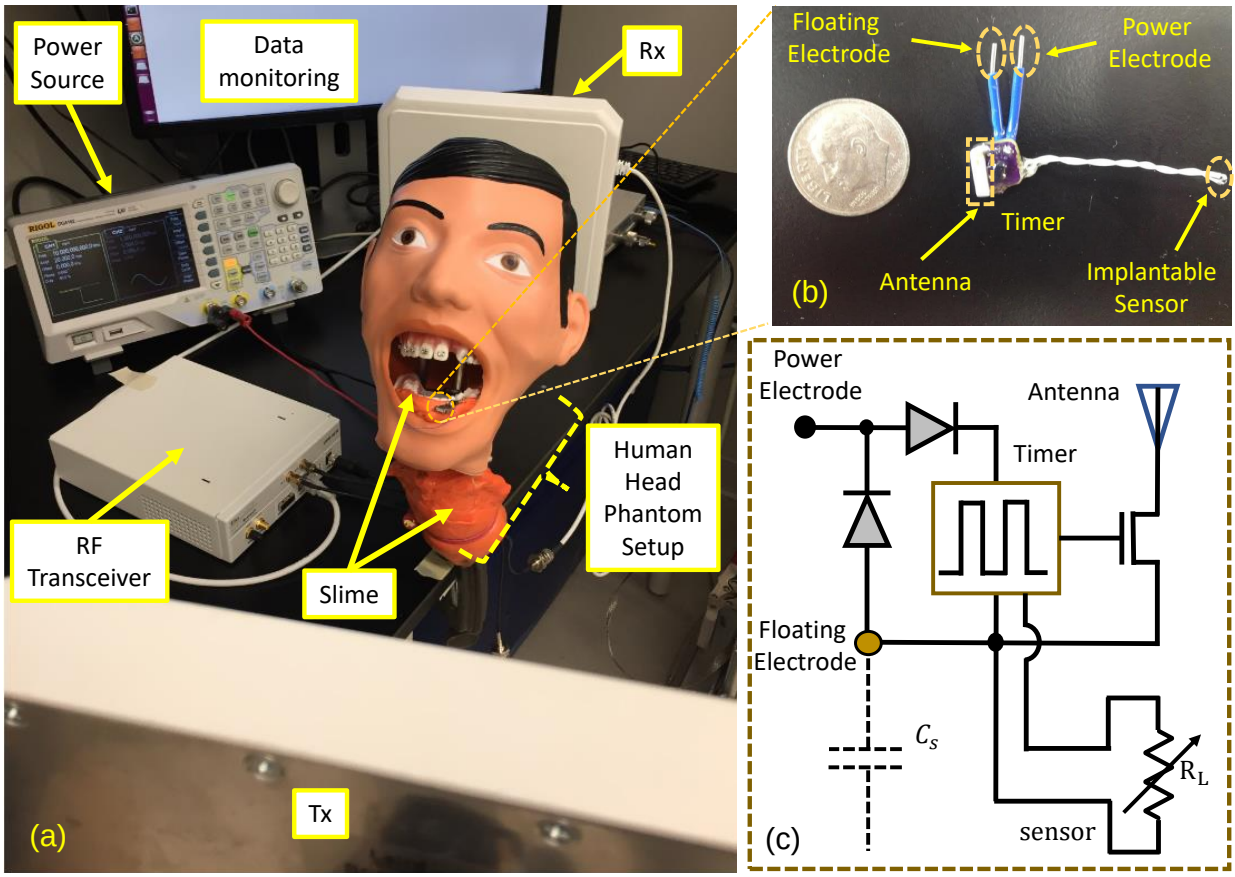

Figure 2.13: Experimental setup using a human head phantom setup retrofitted with the backscattering RF antennas; (a) Setup for measuring the backscattering signal; (b) Proof-of-concept prototype powered using SC-based WPT; and (c) Schematic of the sensing/telemetry interface powered using SC-based WPT.

2.3.4 Human Head Phantom Setup and Hybrid Telemetry Experiment

In this experiment, and as another possible application of the SC-WPT, we used the same prototype of Figure 2.11 (c) to characterize the performance of the SC-based wireless power transfer using human head phantom setup shown in Figure 2.13. Power source (an earth-grounded Tektronix DG4102 function generator) is capacitively coupled to the slime as

shown in Figure 2.13 (a) where the electric charge propagates through the slime to the implant shown in Figure 2.13 (b). A low-power timer oscillator shown in a block diagram in Figure 2.13 (c) is used to switch the impedance of the antenna and the frequency of the oscillator and hence the modulation frequency of the antenna is determined by a resistor R_L whose value changes according to the sensor signal being sensed. The power source is programmed to generate a sinusoidal wave at a potential of 20 V_{pk-pk} and at variable frequencies. The harvester comprised of a single-stage diode bridge shown in Figure 2.13 (b) constructed using two Schottky diodes, noting that the other end of the diode bridge forms the floating-electrode providing a return path for the load-current to the source. For this experiment the source voltage was programmed to 20 V_{pk-pk} with an operating frequency of 10 MHz. The spectrum of the backscattered signal received at R_x when centered around the 915MHz RF carrier was exactly the same as the previous experiment as shown in Figure 2.12 (a). Also, the monotonic change in the modulation frequency as a function of the externally applied temperature was plotted similarly as shown in Figure 2.12 (b). This experimental results show the validity of investing the SC-WPT to deliver the electric power wirelessly to the electronic devices implanted inside the oral cavity of the human head. The combination of the SC-based WPT functionality along with the bi-directional telemetry functions are needed to implement a complete transceiver for continuous health monitoring and substrate computing.

2.4 Summary

In this chapter we presented a wireless power transfer approach based on the intrinsic self-capacitances of substrates. Compared to other WPT approaches, SC-based WPT demonstrates higher PTE, when the target power-budgets are in the order of microwatts. In this chapter we also presented a tractable, lumped-parameter model for SC-based WPT that could be used for system optimization and comparison. This model has been validated using experimental results which demonstrate a broad-band response ($1 - 15\ MHz$) for harvestable power budgets of $20 - 200\ \mu W$. Furthermore, SC-based WPT can demonstrate PTE ($\eta > 90\%$) for distances greater than 10 cm which makes it attractive for large-scale power delivery.

It can be envisioned that the diagnostic cage, as shown in Figure 2.10 (b) could be scaled to larger dimensions, housing multiple ambulatory animals and each animal can wear multiple electronic devices as shown in Figure 2.14 (a) and (b) respectively. Also, the power source is capacitively connected to the body, which will obviate the initiation of any electrochemical reactions at the electrode surface [46]. Using the lumped-parameter model, we also showed in this chapter that the maximum harvestable power for SC-based WPT scales linearly with the dimensions of the receiver transducer. As a result, the size of the wearable or implant antenna could be reduced significantly. Note that the FDA limits on power dissipation for SC-based WPT is estimated to be 2.5 mW/mm^2 [47–49] which is significantly higher than the microwatts power-budget reported in this thesis. In Table 2.2 we compare the self-capacitance based WPT with the most recent related WPT technologies. Note that the inductive and ultrasound WPT are used for delivering power in-vivo, and hence the powering distances are relatively small. However, as the table shows, that the key advantage of the self-capacitance based WPT is its power transfer efficiency.

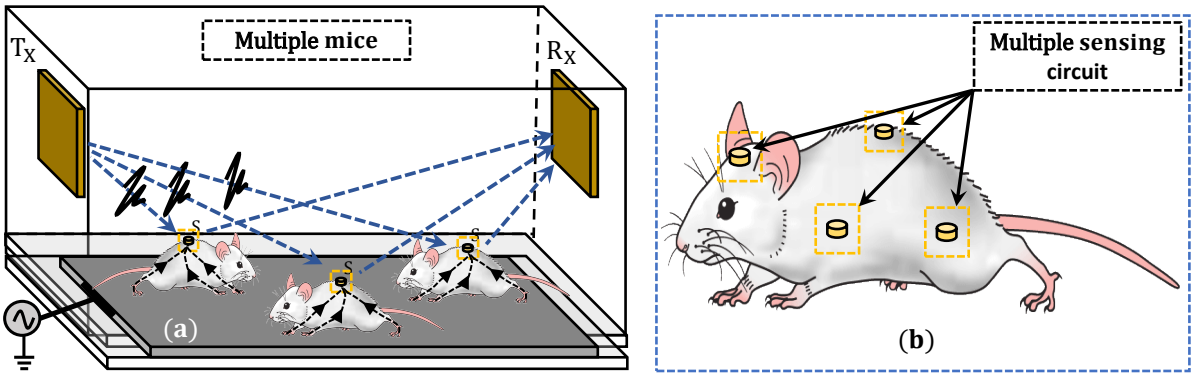

Figure 2.14: Large scale of diagnostic cage with hybrid telemetry: (a) The insulated underlay of the cage is powered and delivers power to wearable electronic devices for multiple mice; (b) Multiple wearable electronic devices for one mouse.

While in this work, we have only focused on delivering microwatts of power, there could be several approaches to boost the power that can be delivered to the load using the proposed SC-based WPT. Increasing the coupling capacitance C_c in the equivalent model in Figure 2.7 (c) is one possible approach, however, this might require modifying the dielectric property of the substrate or the body. The power could be boosted by increasing the open-load voltage of the source as described by equation 2.9. Note that this is viable option as long as the voltage is within the limits of the dielectric breakdown of the material forming C_c. The last option to boost the delivered power would be to increase the size of the self-capacitance of the energy harvester C_s, described by the equation 2.9. However, the received power only scales linearly with the dimensions of the receiver transducer/antenna, as a result beyond a certain form-factor other WPT approaches might be more attractive compared to the proposed SC-based approach. It is worth mentioning that self-capacitance C_s is a parasitic element that will change based on the distribution of the fringe electric-field. However, given a specific form-factor a_r and the shape of the floating-electrode, one could lower-bound the size of C_s using a close-form expression as shown in equation 2.2 for a spherical geometry. This therefore signifies the worst-case C_s for which the load resistance R_L and minimum

delivered power could be estimated. However, to further enhance the delivered power, we would need to do a post-deployment calibration and adjust R_L according to the actual self-capacitance value. Also self-capacitance might lead to an electrostatic charge build up due to floating-electrodes. However, note that the WPT method using ($1MHz$-$15MHz$) AC and the DC potentials at the source and the remote device are decoupled from each other. So, the change in DC potential will not affect the WPT. In terms of safety, the self-capacitance of the floating-electrode is in the order of pico-farads or less. Therefore, the charge build-up at the device should be relatively small. Safety related to electrostatic charge buildup on the body self-capacitance is similar to electrostatic discharge (ESD) safety, a topic that has been extensively studied in the literature [50]. The proposed method is expected to apply to ambulatory animal or human body, however and as a proof of concept the study has been made on mouse cadavers because they are easy to work with to verify the concept. Also, the cadaver accurately models the electrical characteristics of a live animal, provided they have been stored and revived properly. Since the live animal and the cadaver will both have capacitive coupling to the floor of the mouse cage, the WPT mechanism should translate between the two set ups. Motion artifacts or intermittent brown-outs are generally not an issue for energy harvesting as long as the voltage on the harvester is regulated or filtered, and on an average the harvester is receiving microwatts of power. Furthermore, the beauty of the self-capacitance based WPT is that the efficiency degrades only linearly with distance (as shown in Figure 2.5), so the approach should be robust to ambulatory artifacts. The worst-case configuration would be when only the tail of the mouse is in contact with the floor and experimental setup in Figure 2.8 verified the WPT for that configuration. Note that in all other ambulatory states, there will always be an additional capacitive coupling path to the body (unless the animal is in the air). Also, any energy fluctuations due to motion artifacts can be filtered out by the energy regulation unit on the harvester.

Chapter 3

Self-capacitance based Wireless Power Broadcasting for Internet of Medical Things (IoMT)

In chapter 2, We demonstrated the feasibility of exploiting the body's self-capacitance to wirelessly deliver electrical power to a wearable device. In this chapter we extend the previous work to report a wireless power broadcasting (WPB) framework that can simultaneously power multiple devices worn by multiple human subjects. The framework overcomes the efficiency limitations of other WPB approaches that require sufficient power to be broadcast at all times because the number and location of the wearable devices are not known in advance. We investigate the performance and design trade-offs involved when designing a self-capacitance based WPB system. Using a phantom setup we verify the WPB results for different experimental conditions ranging from different numbers of human subjects, human body posture and the geometry of the setup. The results of this chapter are based on [51].

3.1 Introduction

Wireless power broadcasting (WPB) refers to a framework of remotely and simultaneously delivering power to multiple devices. While the concept of WPB has existed for more than

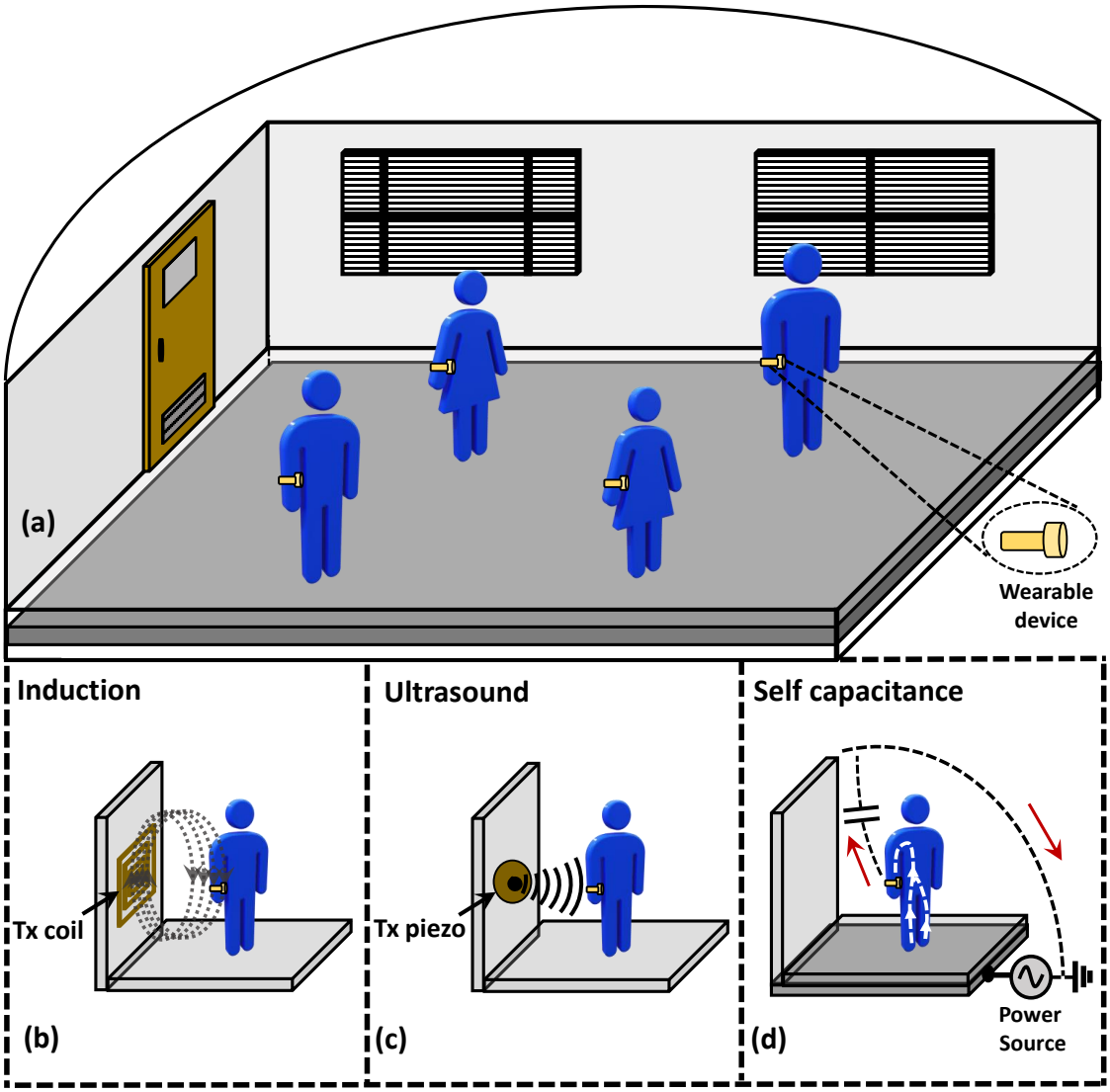

Figure 3.1: Wireless power broadcast (WPB) modalities for smart home/room applications: (b) Induction-based WPB, where the power is transferred magnetically from an embedded transmitter (Tx) coil to a wearable device; (c) WPB through air by means of ultrasound transmitted from an embedded Tx piezo; (d) Self capacitance (SC)-based WPB to a wearable device, where the displacement current is capacitively coupled via an electrically isolated floor with an embedded plate that is excited by an AC source.

a hundred years [52], the proliferation of Internet of Medical Things (IoMT) and wearables has highlighted the challenges related to continuous powering and monitoring, and the need for better WPB [53]. Remote powering of IoMT (e.g. health monitors or smart-patches) alleviates the need for periodic recharging of batteries, hence improving patient compliance for long-term monitoring applications.

For smart room applications as shown in Figure 3.1 (a), a couple of existing WPB approaches have been reported in literature which includes inductive powering as shown in Figure 3.1(b) or acoustic energy transfer using ultrasound as shown in Figure 3.1c [38, 54]. For instance, Rekhi *et al.* [55] proposed the use of ultrasound for WPB to energize a millimeter-sized device and the reported simulation study demonstrated that it was possible to deliver 50 µW over-the-air at a distance of 0.88 m using a 25 cm^2 transmitter array tuned to 48.25 kHz. However, for ambulatory subjects these types of WPB (inductive and ultrasound) are vulnerable to low power transfer efficiency (PTE) due to transducer misalignment artifacts [8, 21–23, 29]. Since neither the location or number of subjects and IoT devices are known *a priori*, these WPB sources must constantly broadcast power in excess of the amount required for sufficiently energizing the devices. As a result, the subjects in the room could be exposed to unnecessary EM or ultrasonic radiation (i.e. the reported ultrasound frequencies would be a disturbance to common household pets). The low PTE will also result in a significant amount of power dissipation at the power source for the source to provide meaningful power to millimeter-scale IoTs with small antennas (or transducers). This is specifically problematic for IoMTs like smart-patches where batteries are unable to buffer sufficient energy for continuous operation [56].

In this chapter, we overcome these challenges by extending our previously reported self capacitance (SC)-based wireless powering technique [7] for WPB. Figure 3.1 (d) shows the

SC-based WPB framework in the context of a smart room. Self capacitance is an intrinsic property of any electrically isolated body which arises because there exists fringe electrostatic fields between a body and a theoretical, but omnipresent, infinitely-large ground plane. Rather than considering the self capacitance as a parasitic element, SC-based power transfer exploits this element as a path for a displacement current emanating from a power source; propagating through the body channel to return back to the power source. This is illustrated in Figure 3.1 (d), where an alternating-current (AC) power source connected to a floor-plate is capacitively coupled to the human body. It was shown in [7], using an animal cadaver, that SC-based method can wirelessly deliver up to 100 µW of power with PTE higher than 99%.

This chapter investigates the trade-offs involved in using a SC-based approach for WPB, with respect to the number of human subjects, body posture, proximity between the subjects, number of wearables and system geometry and configuration.

3.2 Self-Capacitance-based WPB Model

3.2.1 Basic SC-based WPT Model

The fundamental theory and analysis of SC-based wireless power transfer has been reported in [7], which we summarize in this subsection for the sake of completeness. Also, we will formulate the equivalent WPT model for powering a wearable device on a human subject, as illustrated in Figure 3.2 (a). A person is assumed to be standing on an electrically insulated floor (F) with an embedded conductive plate (C). The conductive plate is connected to one end of a two-terminal AC source, with the other end of the source connected to the

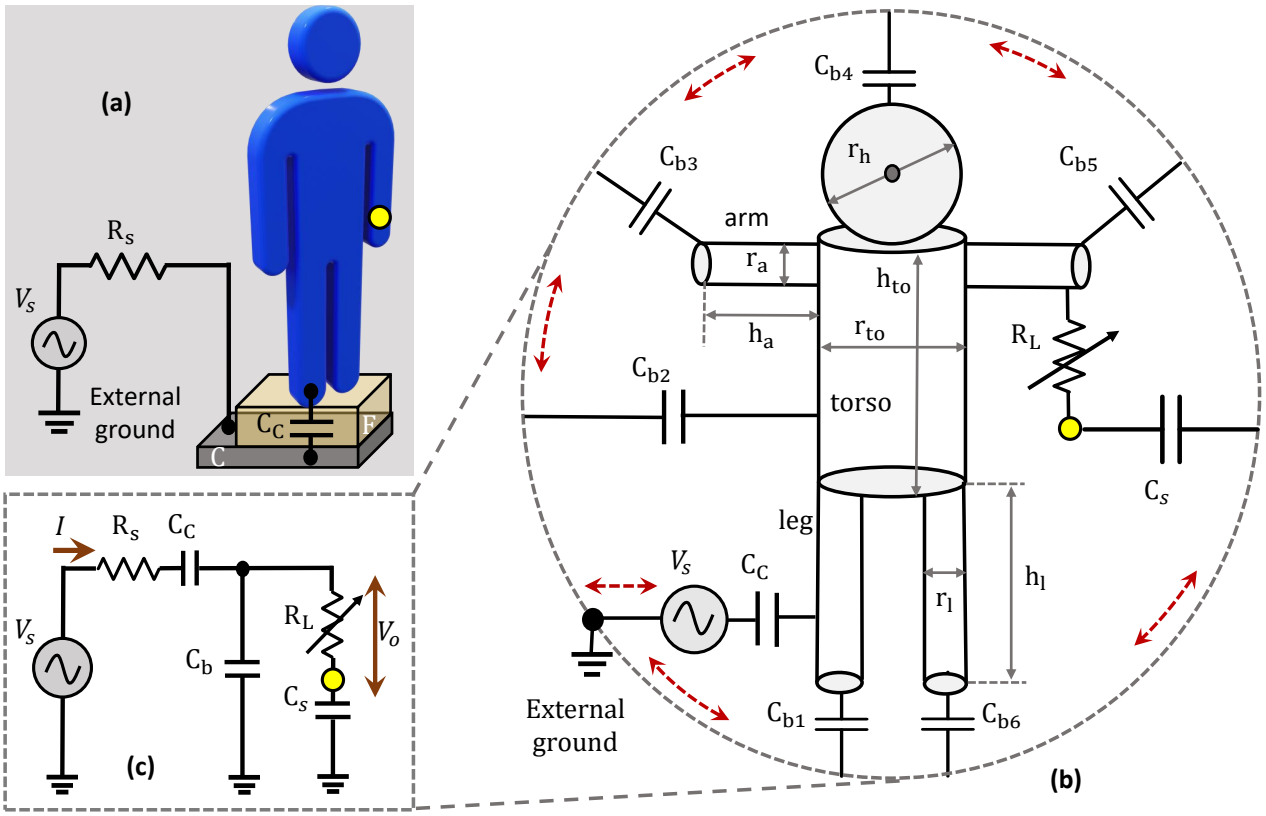

Figure 3.2: Approximation of the Self-Capacitance based WPT for the Internet of Things for the human body; (a) Schematic of a single human body capacitively coupled to the power source for SC-based WPB; (b) Approximation of the self-capacitance by decomposing different segment of the human body into simple shapes; and (c) Lumped-parameter equivalent circuit for a single human body objects having one defined load R_L.

building ground. We will also assume that the wearable comprises of an electrode that is in direct contact with the skin of the subject, whereas the ground reference of the wearable is kept floating in reference to the person. Since the form factors of the human body and the wearable can be considered as being much smaller than the effective wavelength of the AC source (e.g. a 1 MHz signal would have a $\frac{1}{4}\lambda$ of 75 m), the underlying electrical property can be modeled using lumped circuit elements.

The power dissipated at the wearable is modeled using an equivalent load resistance R_L and the self-capacitance between the floating-electrode and the omnipresent ground is denoted

as C_s. Even though the human torso can be modeled as a combination of different shapes, as shown in Figure 3.2 (b), the self capacitance from each of those shapes are combined into a single lumped capacitance, C_b, similarly connected to the omnipresent ground as shown in the lumped parameter equivalent circuit of Figure 3.2 (c). From literature [26], the expression of each shape can be estimated as a function of their respective dimensions. For instance, the self-capacitance of a cylindrical shape is estimated as $C_{cylinder} = \frac{2\pi\epsilon h}{ln(\frac{r_2}{r_1})}$ where h is the length of cylinder, r_1 and r_2 are the inner and outer radius of the cylinder and ϵ is the permittivity of the substrate. Similarly, for a spherical shape (modeling the head), the self-capacitance is given by $C_{spherical} = 4\pi\epsilon r_h$. C_c is the capacitance that models the coupling between the conductive plate C and the feet of the human subject. This assumption is driven by the fact that the body parts closest to the conductive plate will have the largest capacitance and dominate the equivalent circuit. This assumption would not hold if the subject were lying down on the floor, as we will consider in a later example. A detailed derivation of the maximum PTE to the load R_L is available in [7], with the final form given as:

$$\eta = \frac{1}{1 + R_L R_s (C_b\omega)^2 + \frac{R_s}{R_L}(1 + \frac{C_b}{C_s})^2} \tag{3.1}$$

3.2.2 SC-based WPB Equivalent Circuit Model

To extend the self-capacitance-based wireless power transfer (WPT) into wireless power broadcasting (WPB), we consider three people ($n = 3$), in a standing posture, wearing different shoes that can be modeled using coupling capacitors C_{c1}, C_{c2} and C_{c3}, respectively. The shoe material will affect the coupling ratio to the embedded, conductive substrate that

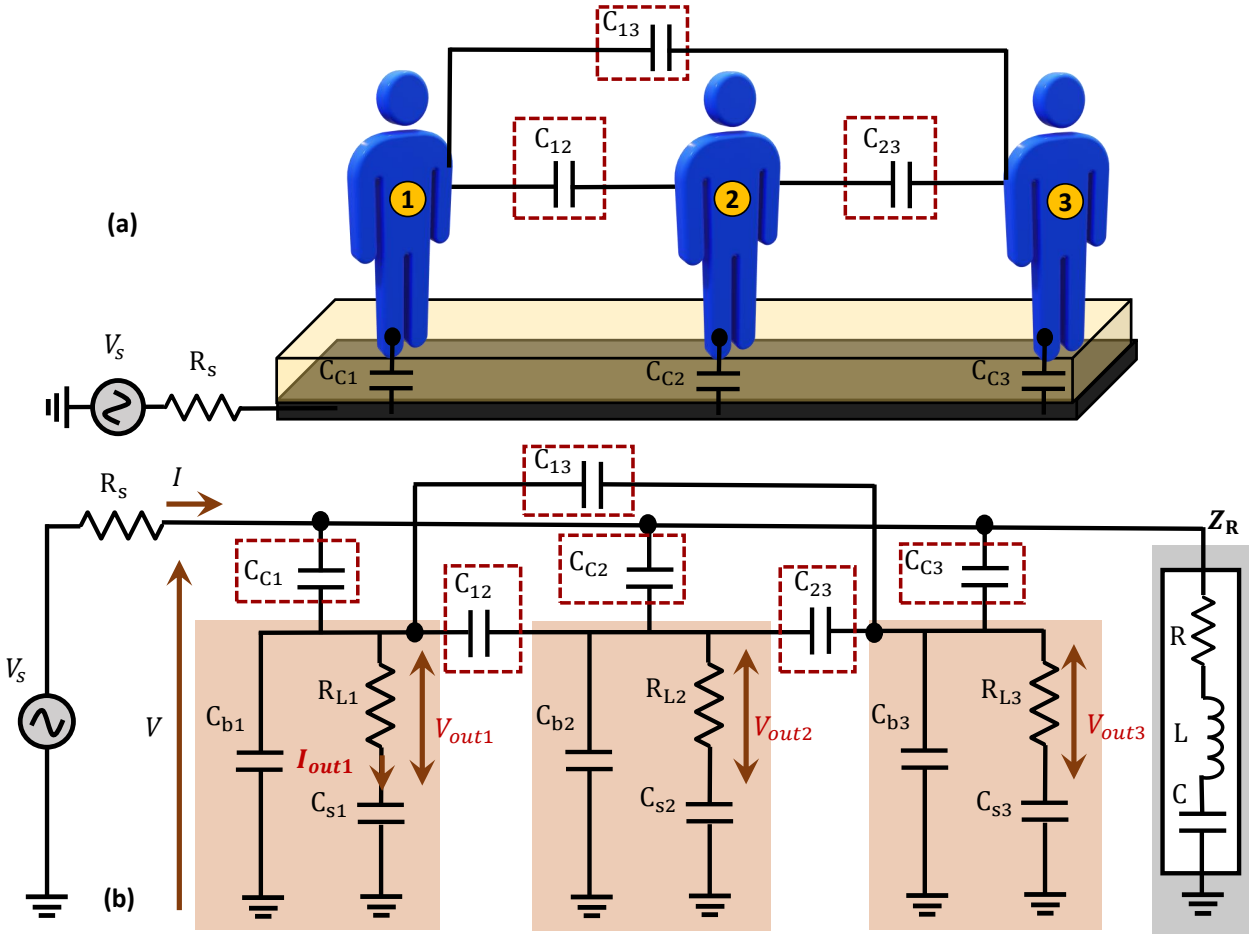

Figure 3.3: Self-capacitance based wireless power broadcasting (WPB) for three persons ($n = 3$) in standing posture; (a) Three human bodies in standing posture wearing three different shoes represented by different coupling capacitors (C_{ci}); (b) Equivalent circuit showing the coupling capacitances (C_{ij}) due to the bodies proximity, where i and $j = 1, 2, 3.....N$ and N represents the number of human bodies involved (Noting that Z_R represents the characteristic impedance of the plate in free space at a specific frequency bandwidth).

is driven by an AC power source, as illustrated in Figure 3.3 (a). The simplified equivalent circuit, including the characteristic impedance Z_R of the conductive substrate's dissipative EM properties, is shown as Figure 3.3 (b). For properly selected conductive substrate sizing and AC frequencies, Z_R is large enough that it can be ignored for a first-order estimate, thus reducing the equivalent model to a capacitor network that can be described using charge.

The inter-body coupling capacitances are defined as C_{ij} for $i, j \in (1, 2, \ldots, n)$ and $i \neq j$, which for this example are simply: C_{12}, C_{23} and C_{13}. The value of the inter-body coupling capacitances will vary based on the proximity of the bodies to each other and will have a direct effect on the received power. Using i to denote a person's index, the received power is P_{ri}. In the next section, we will derive the matrix form expression of the three nodal charge equations of Figure 3.3 (b).

3.3 Analysis of a Three Person Case Study Model

Using the charge conservation law, the three nodal charge equations of Figure 3.3 (b) can be expressed in matrix form as follows:

Simplifying the equivalent circuit model of Figure 3.3 (b) after neglecting the effect of the source resistor R_s results in the equivalent circuit model shown in Figure 3.4.

Considering the human bodies as nodes 1, 2 and 3, and applying the charge conservation law, we get :

$$\begin{aligned} C_{c1}(V_1 - V_s) + C_{b1}V_1 + C_{s1}(V_1 - V_{out1}) \\ +C_{12}(V_1 - V_2) + C_{13}(V_1 - V_3) = 0 \end{aligned} \tag{3.2}$$

$$C_{c2}(V_2 - V_s) + C_{b1}V_2 + C_{s2}(V_2 - V_{out2}) \\ +C_{12}(V_2 - V_1) + C_{23}(V_2 - V_3) = 0 \tag{3.3}$$

$$C_{c3}(V_3 - V_s) + C_{b3}V_3 + C_{s3}(V_3 - V_{out3}) \\ +C_{13}(V_3 - V_1) + C_{23}(V_3 - V_2) = 0 \tag{3.4}$$

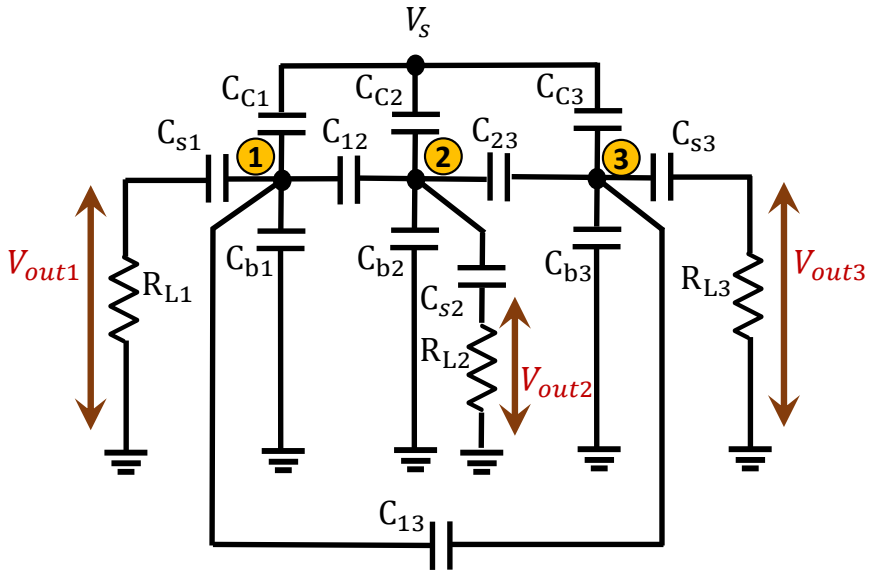

Figure 3.4: Simplified equivalent circuit model for a three person case study of Fig. 3.3 (b).

And from the voltage divider between each node and load R_i, we get in Laplace form :

$$V_{out1} = V_1 \frac{R_{L1}}{R_{L1} + 1/sC_{s1}} \tag{3.5}$$

$$V_{out2} = V_2 \frac{R_{L2}}{R_{L2} + 1/sC_{s2}} \tag{3.6}$$

$$V_{out3} = V_3 \frac{R_{L3}}{R_{L3} + 1/sC_{s3}} \tag{3.7}$$

Now substituting (3.5), (3.6), and (3.7) into (3.2), (3.3) and (3.4), respectively and solving for V_{outi}, we get:

$$\begin{aligned}\left[C_{s1} + (C_{c1} + C_{b1} + C_{s1} + C_{12} + C_{13})\left(1 + \frac{1}{sR_{L1}C_{s1}}\right)\right]V_{out1} \\ -C_{12}\left(1 + \frac{1}{sR_{L2}C_{s2}}\right)V_{out2} \\ -C_{13}\left(1 + \frac{1}{sR_{L3}C_{s3}}\right)V_{out3} = C_{c1}V_s\end{aligned} \tag{3.8}$$

$$\begin{aligned}\left[C_{s2} + (C_{c2} + C_{b2} + C_{s2} + C_{12} + C_{23})\left(1 + \frac{1}{sR_{L2}C_{s2}}\right)\right]V_{out2} \\ -C_{12}(1 + \frac{1}{sR_{L1}C_{s1}})V_{out1} \\ -C_{23}(1 + \frac{1}{sR_{L3}C_{s3}})V_{out3} = C_{c2}V_s\end{aligned} \tag{3.9}$$

$$\begin{aligned}\left[C_{s3} + (C_{c3} + C_{b3} + C_{s3} + C_{23} + C_{13})\left(1 + \frac{1}{sR_{L3}C_{s3}}\right)\right]V_{out3} \\ -C_{13}(1 + \frac{1}{sR_{L1}C_{s1}})V_{out1} \\ -C_{23}(1 + \frac{1}{sR_{L2}C_{s2}})V_{out2} = C_{c3}V_s\end{aligned} \tag{3.10}$$

In general, the capacitively coupled human network with an arbitrary number of people, n, can be generalized with the following expression:

$$\sum_{j=1}^{n}\sum_{i=1}^{n}\Big[C_{sj}+(C_{cj}+C_{bj}+C_{sj}+C_{ij})\big(1+\frac{1}{sR_{Lj}C_{sj}}\big)\Big]V_{outj} \\ -C_{ij}\big(1+\frac{1}{sR_{Li}C_{si}}\big)V_{outi}=C_{cj}V_s,\quad i\neq j \tag{3.11}$$

where the connections are assumed to be undirected, i.e., $C_{ij}=C_{ji}$.

In a matrix form, (3.8), (3.9), and (3.10) can be represented as :

$$\big[A\big]\{V_{out}\}=\big[C_c\big]V_s \tag{3.12}$$

where, the matrix [A] is defined as below,

$$[A]=$$

$$\begin{bmatrix} C_{s1}+(C_{c1}+C_{b1}+C_{s1}+C_{12}+C_{13})\,(1+{}^{1}/_{R_{L1}C_{s1}s}) & -C_{12}\,(1+{}^{1}/_{R_{L2}C_{s2}s}) & -C_{13}\,(1+{}^{1}/_{R_{L3}C_{s3}s}) \\ -C_{12}\,(1+{}^{1}/_{R_{L1}C_{s1}s}) & C_{s2}+(C_{c2}+C_{b2}+C_{s2}+C_{12}+C_{23})\,(1+{}^{1}/_{R_{L2}C_{s2}s}) & -C_{23}\,(1+{}^{1}/_{R_{L3}C_{s3}s}) \\ -C_{13}\,(1+{}^{1}/_{R_{L1}C_{s1}s}) & -C_{23}\,(1+{}^{1}/_{R_{L2}C_{s2}s}) & C_{s3}+(C_{c3}+C_{b3}+C_{s3}+C_{23}+C_{13})\,(1+{}^{1}/_{R_{L3}C_{s3}s}) \end{bmatrix}$$

$\{V_{out}\}$ represents the output voltages vector, and $[C_c]$ contains only real-valued time invariant elements. The corresponding power (P_{ri}) dissipated by the load (R_{Li}) is given by:

$$P_{ri}=\frac{(V_{outi})^2}{R_{Li}} \tag{3.13}$$

Table 3.1: Show Sole Materials Properties and their effect on the coupling capacitance C_c.

Shoe Sole Material	Electrical Properties	Dimensions	Capacitance
Rubber	$\epsilon_r = 7$ [57]	A $= 30 - 160\ cm^2$, t $= 2 - 5\ cm$	$3.7 - 50\ pF$
Leather	$\epsilon_r = 3.4$ [58]	A $= 30 - 160\ cm^2$, t $= 2 - 5\ cm$	$1.8 - 5\ pF$

And the total power dissipated at the entire module load is the summation of the individual power dissipation at the load of each circuit branch, and is given by

$$P_r = \sum_{i=1}^{n} P_{ri} \tag{3.14}$$

The range of the capacitance values depends on variables such as the material of the shoe's sole and the size of the shoe. Table 3.1 shows representative values of the coupling capacitance range.

There are many important parameters in (3.12) that have a direct effect on the received power P_r. Shown in Figure 3.5 (a) and (b) are the simulated received powers for each person, as a function of the coupling capacitance C_{c3}, for two cases of inter-body coupling between person 1 and person 3, $C_{13} \in (1\ fF - 100\ pF)$. In the case of Figure 3.5 (a), a weak inter-body coupling C_{13} =1 fF, means that changing coupling capacitance of person 3 to the conductive substrate (i.e. sweeping C_{c3}) does not significantly affect the power delivered to person 1 or 2. However, in Figure 3.5 (b), person 1 and 3 were modeled as being close to each other, hence a larger C_{13} of 100 pF is used in the simulations. This yields improved power transfer for person 3, even when they have a small coupling to the conductive substrate (C_{C3} <25 pF, since the power can traverse a capacitively coupled path through person 1. This results in

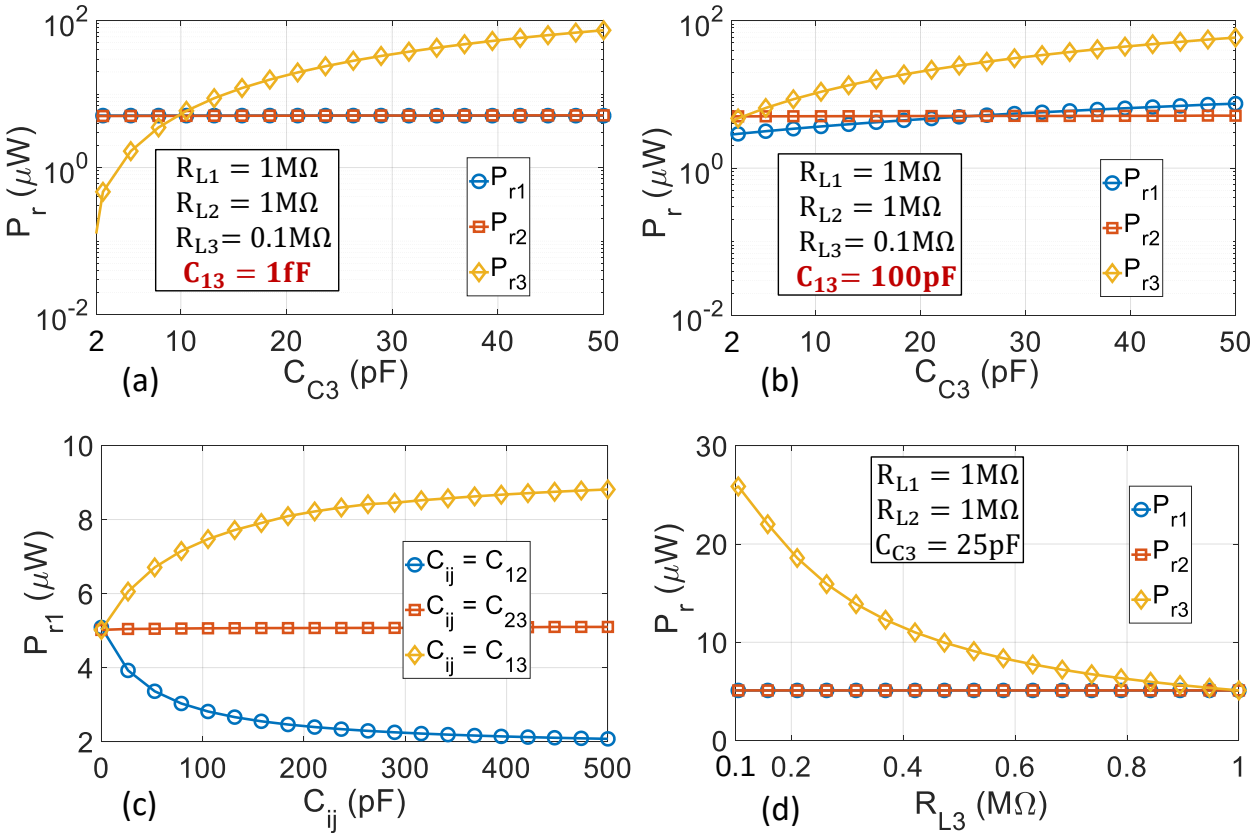

Figure 3.5: Simulated power received, P_r, as a function of coupling capacitance C_{ci}, separation distance between two human bodies represented by C_{ij}, and load resistance R_{Li}; (a) P_{ri} as a function of C_{c3} for large separation between person 1 and person 3 simulated with C_{13} =1 fF; (b) P_{ri} as a function of C_{c3} for small separation between person 1 and person 3 simulated as C_{13} =100 pF; (c) P_{r1} as a function of C_{ij} for constant load resistance R_{L1} =1 $M\Omega$, C_{c1} =25 pF, C_{c2} =2 pF and C_{c3} =50 pF; (d) P_{ri} as a function of the load resistance R_{L3} with constant coupling capacitance C_{c3} =25 pF and C_{13} =1 fF.

the received power of person 1 being negatively affected when person 3 is weakly coupled, but also allowing greater power delivery when the shared coupling capacitance of the two subjects is greater. In this example, the received power for person 2 remains constant since it is not affected by the swept capacitance, nor the change in inter-body capacitance from Figure 3.5 (a) to Figure 3.5 (b) as $C_{12} = C_{23} = 1\ pF$. Figure 3.5 (c) shows the received power by person 1 ($C_{c1} = 25\ pF$, $R_L = 1\ M\Omega$ when sweeping the inter-body capacitance C_{ij}, assuming that person 2 has a small coupling capacitance to the conductive substrate ($C_{c2} = 2\ pF$, while person 3 is larger ($C_{c3} = 50\ pF$. Again, we see that changing the inter-body capacitance of non-person 1 subjects, C_{23}, does not adversely affect the received power for person 1. We can also observe that a stronger coupling between person 1 and 2 reduces the received power of person 1, due to a larger portion of the total delivered power to person 1 and 2 being shared to person 2. Conversely, a stronger coupling to person 3, with a larger coupling capacitance, allows person 1 to receive additional power. Figure 3.5 (d) shows the variation of the received power P_{ri} as a function of the load resistance R_{L3}, where it is clearly shown that the loading on any branch of the setup does not affect the received power of other branches.

3.4 Experimental Results

The system prototype of the proposed WPB module for a smart room application is composed of three main parts: AC source, conductive substrate, and portable multimeters for measurement and characterization purposes as shown in Figure 3.6 (a). The AC source (a mains-grounded Tektronix DG4102 function generator), provides power to the self-capacitance-based WPB by connecting its positive terminal to a conductive substrate. In this setup, the

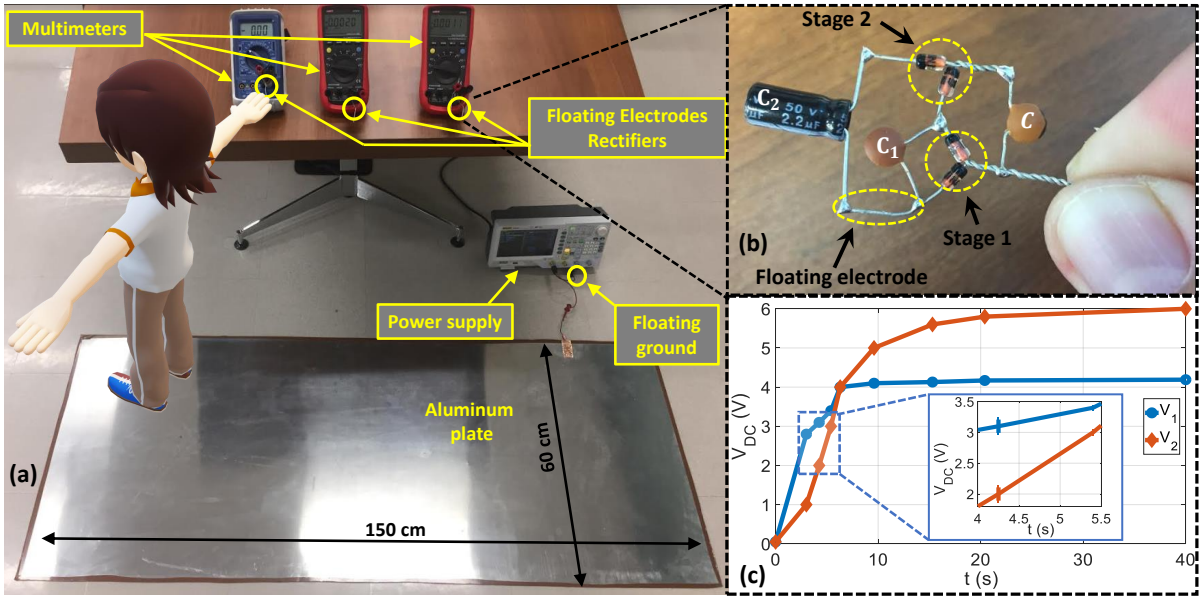

Figure 3.6: Experimental setup: (a) a sketch showing an SC-WPT configuration for a human body; (b) Two-stage Dickson multiplier (AC-DC rectifier and charge pump) that is conductively connected to a human body and charges a 2.2 μF load capacitor; (c) Output voltage versus time of the two-stage multiplier across C_1 and C_2 capacitors.

substrate is a 60 $cm \times 150$ cm aluminum sheet. The negative terminal of the function generator, which is internally connected to mains ground, is otherwise kept floating. When a human subject stands on the sheet wearing shoes, the soles provide an insulating layer between the conductive substrate and the human body. This is conceptually equivalent to a capacitor that is directly proportional to the area of the sheet/human body overlap area and inversely proportional to the sheet/body separation distance.

When an alternating current is applied to the sheet, a displacement current flows through the structure which capacitively couples energy to the human body. SC-based WPB will be affected by different postures (standing, sitting, or laying on the plate) which is simply described as one node of the equivalent electric circuit [59], and the insulated base of the shoes or any other electrically insulator can be directly used as the coupling capacitor. In practice, the conductive substrate could be placed under an insulating floor layer (tile,

concrete, wood subfloor, etc) which would also dictate the coupling capacitance. A simplified device is comprised of a two-stage Dickson multiplier charging a 2.2 μF load capacitor, as shown in Figure 3.6 (b). The device was not optimized for performance and used off-the-shelf 1N4002 diodes and 10 pF ceramic capacitors. The charging curve of the load capacitors at the two stages of the multiplier are presented in Figure 3.6 (c) for a 1 MHz, 20 V_{pk-pk} AC excitation being applied to the conductive substrate. Measurements are obtained from battery-powered multimeters with no direct conductive path to mains ground. The floating-electrode's return path for the load current to the source must go through the omnipresent capacitance to ground. A two-stage example was used for simplicity, but multiple charge pump stages, or switching regulators could be employed to achieve a target DC voltage level.

Four experimental configurations were tested to characterize the proposed self-capacitance based WPB setup, and in each experiment the voltage across the load R_L =1 $M\Omega$ was measured for different operating frequency since frequency is one of the critical parameters for identifying the limitations, robustness, and achievable physical range of the power transfer. All experiments involving human subjects were performed under approved IRB protocol #201907109. The first experiment is to characterize the posture effect of the human body (standing, sitting and laying down) on the received power and the result is shown in Figure 3.7 (a), where, as expected, larger power delivery occurs in a laying down posture because of the bigger coupling capacitance C_c it constructs compared with the other two postures. For all postures, an insulative layer between the human body and the conductive substrate was maintained.

In a second set of experiments, we used one human body in a standing posture holding either one or two resistive loads of 1 $M\Omega$. When holding two 1 $M\Omega$ loads in parallel, the effective load to be driven by the person becomes 500 $k\Omega$ and that increased loading

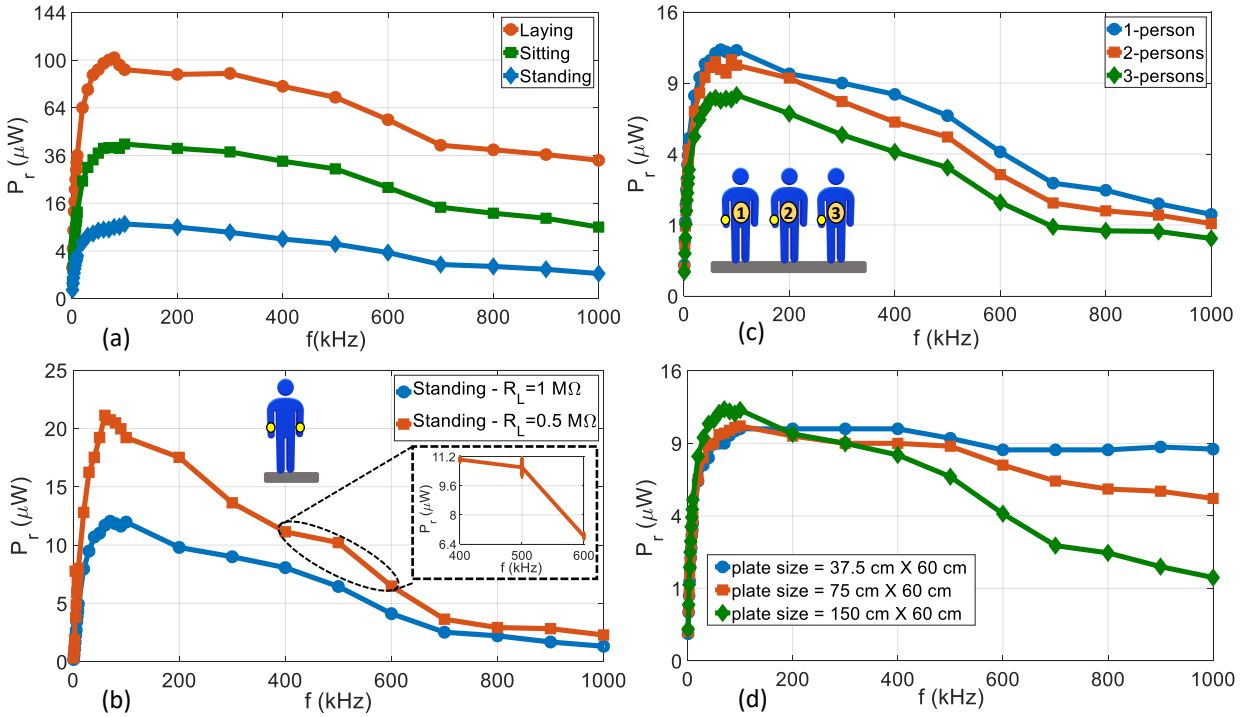

Figure 3.7: Experimental results showing prototype setup characterization for different conditions: (a) Human body posture (Supine, Sitting and Standing), (b) One person in a standing posture, driving one or two 1 $M\Omega$ loads, (c) WPB situation with multiple people, (d) Effect of conductive substrate size.

causes significant increase in the received power per load (total received power for the person increases) as shown in Figure 3.7 (b). Figure 3.7 (c) shows the measured effect of WPB to multiple humans using the same conductive substrate. Increasing the number of bodies (hence increasing the total loading as each person is driving a 1 $M\Omega$ load), reduces the received power at each load.

As shown in Figure 3.7, the received power shows a strong dependence on the AC source frequency; this is partially due to the large size of the conductive plate causing it to act as a radiative antenna, thus dissipating some of the input energy as electromagnetic (EM) waves. The EM waves effectively add a parallel load to the wearable load R_L of the human subjects. The amount of EM radiation increases as the source frequency increases, or as the

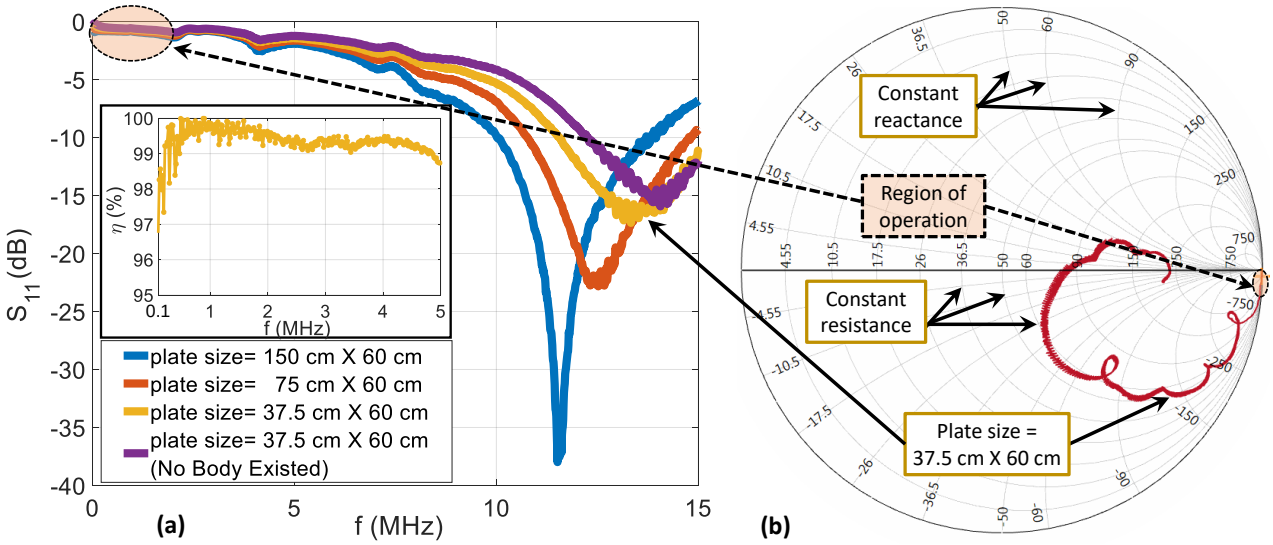

Figure 3.8: Experimental results showing the effect of sheet sizing for WPT to a single person: (a) Power transfer efficiency (PTE) as measured by the reflection coefficient S_{11}; (b) Smith chart measurement for power radiation at higher frequencies on a 37.5 $cm \times 60$ cm sheet.

conductive substrate size increases, as shown in Figure 3.7 (d) for a single human body in a standing posture driving R_L =1 $M\Omega$.

In the final set of data shown in Figure 3.8, we replaced the function generator with a Vector Network Analyzer (VNA) for the AC source. This setup allows us to measure the amount of power dissipation due to EM radiation and to demonstrate the high PTE potential, as measured using the S_{11} parameter. Three different sheet sizes were used to verify the effect of EM losses, which confirmed that for frequencies less than 1 MHz there was no significant loss to EM radiation. The existence of a human body loading the conductive substrate did cause measurable shifts in the location of the peak EM radiation, but those occurred for frequencies larger than 10 MHz and only had a marginal influence for the frequencies of interest in SC-based WPB. Figure 3.8 (b) shows the measurements for the 37.5 $cm \times 60$ cm sheet in a conventional Smith chart.

3.5 Summary

In this chapter we extended the results of our previous work illustrated in chapter 2, regarding self-capacitance-based wireless power transfer (WPT), to a wireless power broadcast (WPB) approach. We have implemented a small-scale prototype WPB for smart room applications as shown in Figure 3.9 (a) to deliver energy through an electrically isolated conductive substrate to the human body for levels of power required by Internet of Medical Things (IoMT) applications such as remote health monitoring or fitness tracking. We characterized the prototype by verifying the effect of including more human bodies, differing load resistances, the human posture, and the substrate size on the amount of the received power at each load. Compared to other WPB approaches, SC-based WPB demonstrates higher PTE and a better solution of delivering the power to the small size wearable electronics without orientation losses.

In this chapter we also presented a lumped-parameter model in which we identified two model scenarios; one is the model for adding more human bodies to the system configuration, and the other is of adding more load or wearable electronics to each individual body. We showed that the addition of more human bodies causes voltage decay at each individual circuit branch, especially at high frequencies, but holistically this increases the amount of power delivered due to the increase in the total coupling capacitance C_c which has been proven in chapter 2. The prototype results showed that the received power can be improved by simply subdividing the floor into reasonably small sizes as shown in Figure 3.9 (b) in order to limit the losses to EM radiation whilst still providing full room coverage.

Future work will involve optimizing the setup to maximize usability of WPB regardless of the load configurations. It is also preferable to reduce the power consumption of wearable

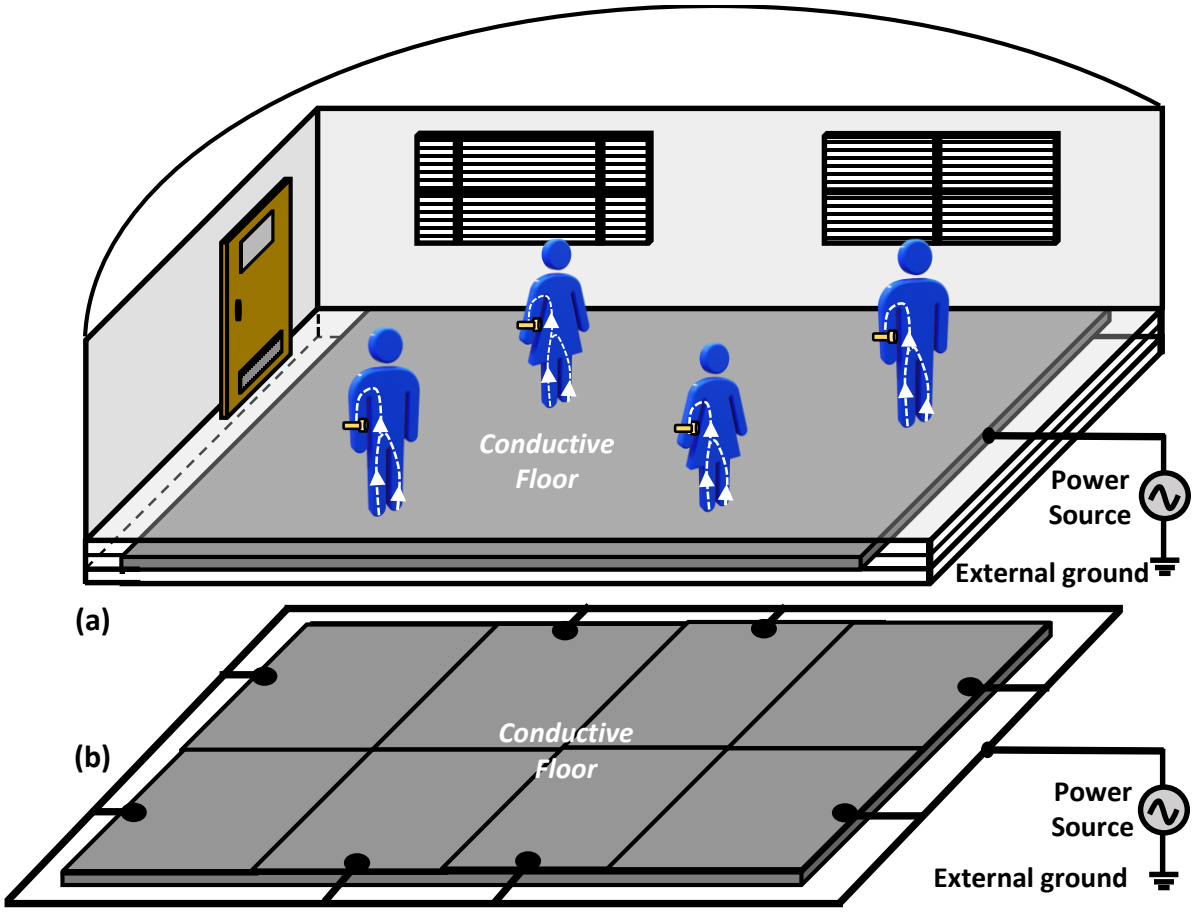

Figure 3.9: Modification of the smart home's floor for power transfer optimization: (a) Simplified, illustrative SC-WPB conductive floor design; (b) Subdivided conductive floor into many small and electrically isolated conductive floor segments to limit the RF power radiation and make construction modular.

electronic devices in addition to reduce their sizes while preserving good performance in order to improve the power transfer efficiency of the SC-WPT as we will see in the next chapter.

Chapter 4

A Compact and Energy-efficient Instrumentations using PTAT Reference Circuit

In this chapter, I present an energy-efficient ultrasound electronic receiver and general purpose sensor as electronic wearable devices that can operate over a wide range of input variables. I use the proportional-to-absolute-temperature (PTAT) reference circuit to directly inject the ultrasound signal, and hence eliminate the pre-amplification and rectification stages used in a conventional ultrasonic receiver which leads to a significant improvement in the system energy-efficiency. The results of this chapter are based on [60].

4.1 Introduction

Self capacitance based WPT for wearable or mountable devices demonstrates higher PTE compared with other WPT modalities, but that is true when the power budget of wearable devices is in the order of microwatts as I explained in chapter 2 and chapter 3. Therefore, wearable devices have to be energy-efficient in order to be powered by this WPT approach. Examples of wearable devices are the ultrasound receivers.

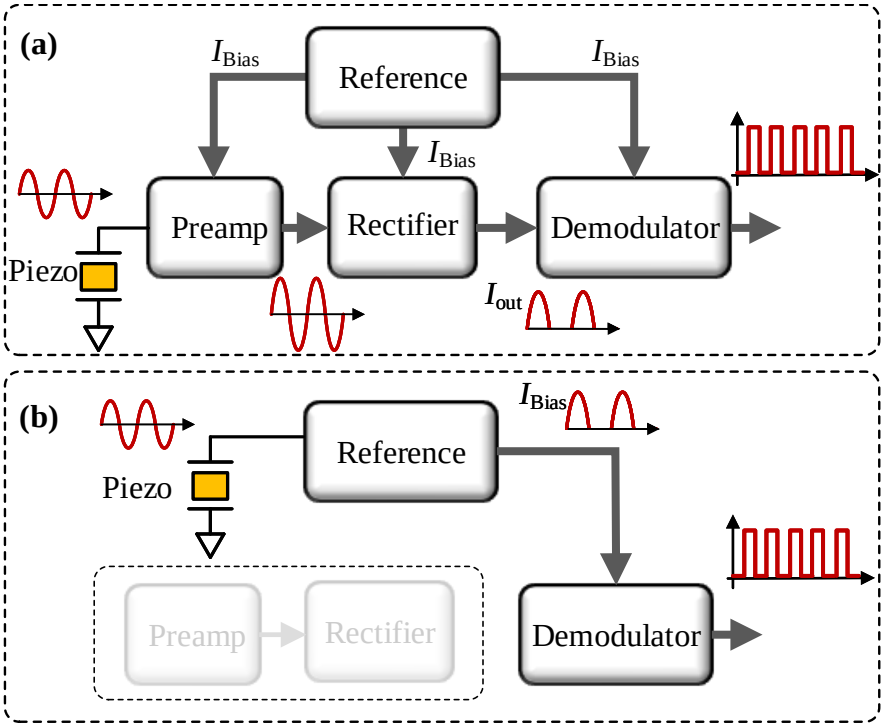

Figure 4.1: (a) Conventional ultrasonic receiver topology comprising of preamplification, rectification, demodulation and reference modules; (b) Proposed topology using only the reference circuit and demodulation modules.

Ultrasound transceivers are commonly used in many different applications ranging from biomedical imaging [33] to communications through different substrates [61, 62]. In these applications, portability and autonomy are some of the key requirements that requires the transceiver to be compact and energy-efficient. With regard to system energy-efficiency, the front-end circuits of a typical ultrasound receiver is important because these modules have to be active all the time for sensing, amplifying and detecting any incident ultrasonic pulses.

These front-end modules are shown in Figure 4.1 (a) and comprises of preamplification, rectification and demodulation stages. Also shown in Figure 4.1 (a) is a reference module that generates the bias signal for each of these modules. The pre-amplification stage amplifies

the incident ultrasonic signal (as generated by a piezoelectric transducer - labeled as *Piezo* in Figure 4.1 (a)), which is then rectified and filtered by the rectification stage. The demodulator compares the rectified energy with a threshold to determine the received symbol ('0' or a '1'). In this chapter we investigate if the pre-amplification and rectification stages can be eliminated by directly injecting the incident ultrasonic signal into the reference circuit, as shown in Figure 4.1 (b). As a result, the reduced topology in Figure 4.1 (b) would yield superior energy-efficiency compared to the topology shown in Figure 4.1 (a). Specifically, we show that a standard proportional-to-absolute temperature (PTAT) current reference circuit can be used as an ultrasonic receiver front-end. It can be noted here that for operation at a very low supply voltages, bandgap references like the PTAT are the most suited topologies among all other references [63]. By construction, the PTAT implements a fixed-point circuit [64, 65], that generates a constant current that is theoretically independent of the supply-voltage fluctuations. The location of the fixed point (and hence, the output reference current) can be modulated by changing the value of the PTAT resistor and in the proposed implementation (shown in Figure 4.2 (a)), the piezoelectric transducer is connected in parallel to the resistor R. The transduced ultrasound signal is therefore injected into the PTAT, resulting in the change in the output current. In this mode of operation, the magnitude of the PTAT current is constrained only by the maximum drain-current of the MOSFET transistors, as a result of which, the output current can vary depending on the magnitude of the signal injected into the PTAT. This overcomes the dynamic-range limitations exhibited by most common pre-amplifier topologies used in ultrasound receivers that are based on transconductance [66–69] or transimpedance [70–73] elements, where the bias current determines the output dynamic range and the threshold of the rectifying diode determines the sensitivity of receiver.

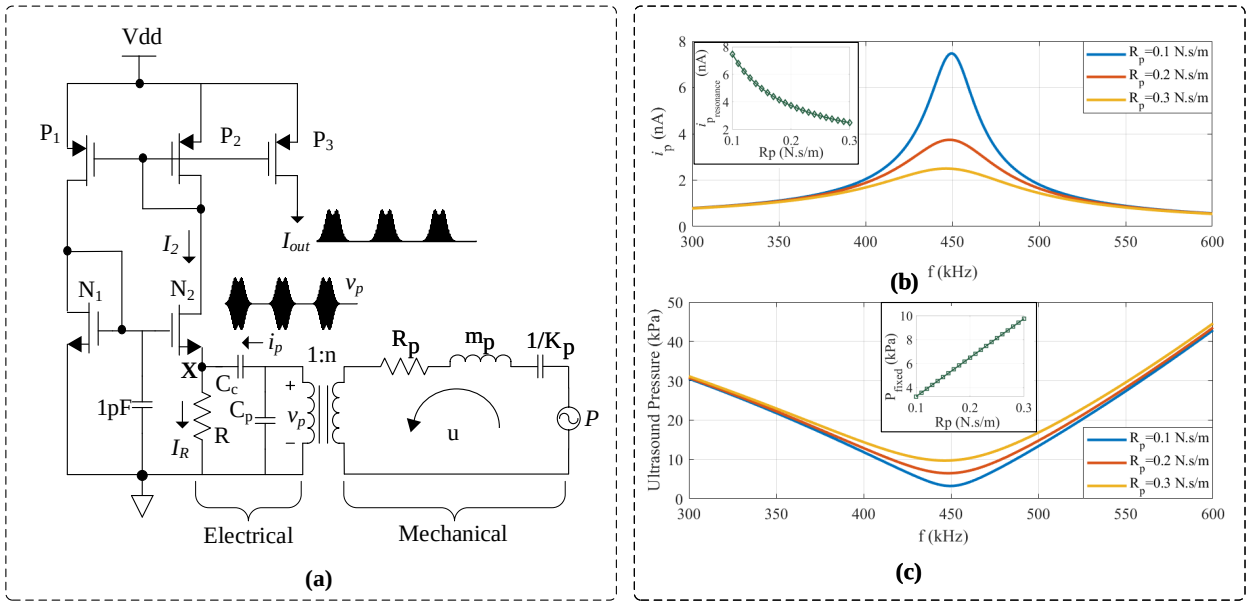

Figure 4.2: PTAT-based receiver circuit: (a) Interface between the PTAT and the piezoelectric transducer equivalent circuit; (b) Frequency response of the piezoelectric generated current i_p at different mechanical damping constant R_p values when the ultrasound pressure is fixed to 10 MPa;Inset shows the variation of i_p at resonance with R_p; (c) Frequency response analysis of the received ultrasound pressure P through the piezoelectric transducer at different values of mechanical damping constant R_p when the absolute value of i_p is fixed to $25mV/R$; Inset shows the variation of the fixed value of the pressure at resonance, P_{fixed}, with R_p.

4.2 Principle of Operation

4.2.1 PTAT Ultrasound Receiver

Since PTAT circuits have been extensively studied in literature [74, 75], in this section we only provide a brief summary of the principle of operation in the context of ultrasonic receiver design. A standard PTAT circuit, as shown in Figure 4.2 (a) operates on the principle of settling to a fixed operating point [76] which corresponds to the intersection between a linear function (implemented by transistors P_1 and P_2) and a nonlinear function (implemented by the transistors N_1, N_2 and the resistor R). When an external current i_p is injected into

the node X of the PTAT as shown in Figure 4.2 (a), the large-signal model governing the dynamics of the PTAT is given by

$$f^{-1}(\frac{I_2}{I_0}) - (I_2 + i_p)R = f^{-1}(\frac{I_2}{MI_0}) \tag{4.1}$$

where I_2 denotes the drain current through P_2. I_o denotes the specific current [77], M represents the ratio of the sizes of transistors N_1 and N_2, and $f(.)$ is a positive real-valued function, which depends on the operational regime of N_1 and N_2.

As i_p is varied about the biasing point, the fixed-point and hence the output current I_2 of the PTAT circuit also varies according to the solution of the Equation (4.1). We assume here that i_p changes quasi-statically with respect to the intrinsic time-constant of the PTAT [76], and that V_X remains clamped to $\eta U_T \approx 25\ mV$, thus acting as a virtual ground at which the current is rectified. Since Equation (4.1) above also has a trivial solution implying a no output case, we can write the solution to the above as follows:

$$I_{out} = I_2 = \begin{cases} 0 & i_p > \frac{25mV}{R} \\ g(i_p) & i_p \leq \frac{25mV}{R}, \end{cases} \tag{4.2}$$

where $g(\cdot) : \mathbb{R} \mapsto \mathbb{R}_+$ is any positive real-valued function of the input current i_p which corresponds to the non-trivial fixed point, and is parameterized by the properties of the circuit elements in the PTAT circuit. It can thus be observed from Equation (4.2) that irrespective of the polarity of i_p, the lower bound of the output current I_2 will always be clamped to zero and hence the PTAT acts as a current rectifier. When the transistors are biased in sub-threshold or weak-inversion, equation (4.1) reduces to

$$I_{out} = I_2 = \frac{\eta U_T}{R}\ln(M) - i_p. \tag{4.3}$$

where η denotes the subthreshold slope and U_T is thermal voltage which is approximately 25 mV at room temperature [77]. It should be noted here that since i_p can either flow into and out of the output node X, the output current I_{out} can take a wide range of values depending on the value of i_p. This, however, includes the pathological case when $i_p = -I_2$, resulting in no bias current being generated by the circuit.

By replacing the current source by a piezoelectric transducer, as shown in Figure 4.2 (a), the PTAT can be used to directly sense and rectify the current generated by the transducer. To simulate the functionality of this topology, we have used an equivalent circuit model of a piezoelectric transducer [78], where the mechanical and the electrical parameters of the transducer are coupled through a transformer. The representative electro-mechanical equation relating the change in the current output to the change in the ultrasound pressure sensed by the transducer is given by:

$$\Delta i_p = n\Delta u - C_p \dot{v}_p,$$

$$\Delta i_p = n\frac{\Delta F}{Z} - C_p \dot{v}_p, \tag{4.4}$$

where n denotes the electromechanical coupling factor of the transducer, $\dot{v}_p$ is the rate of change of voltage across the crystal, C_p is the intrinsic capacitance of the crystal, u is the rate of change of the transducer stain, ΔF represents the variation in ultrasound pressure ΔP over the surface area A of the transducer, and Z is the mechanical impedance of the piezoelectric transducer. The mechanical impedance Z is given by ($Z = R_p + j(\omega m_p - K_p/\omega)$)

Table 4.1: Parameters used to analyze the frequency response of the PTAT receiver.

Parameter	Description	Value
m_p	piezoelectric mass	0.075 g
k_p	piezoelectric stiffness	0.0477 GN/m
n	electromechanical coupling	0.75
C_c	Coupling capacitance	15 pF
C_p	piezoelectric intrinsic capacitance	1 nF
d	piezoelectric diameter	5 mm
t	piezoelectric thickness	0.4 mm

as shown in Figure 4.2 (a), where R_p is the damping constant, m_p is the mass and K_p is the stiffness of the piezoelectric transducer, and ω is the frequency of the mechanical vibration.

At resonance, the reactive part of the mechanical impedance vanishes leading to $Z = R_p$. Assuming that the voltage at node X shown in Figure 4.2 (a) is constant and the transistors are biased in sub-threshold regime, we arrive at the following two equations:

$$C_p \dot{v}_p + C_c \dot{v}_p = nA\frac{\Delta P}{R_P}, \tag{4.5}$$

and

$$\Delta I_2 = -\Delta i_p \tag{4.6}$$

The change in the output current with respect to the change in the ultrasound pressure is given by

$$\frac{\Delta I_2}{\Delta P} = \begin{cases} -\dfrac{nAC_c}{R_P(C_p + C_c)} & P > P_{fixed} \\ 0 & P \leq P_{fixed}, \end{cases} \tag{4.7}$$

where P_{fixed} represents the lower bound of the fixed ultrasound pressure corresponding to the non-trivial fixed point of the circuit. Figure 4.2 (a) also leads us to the following expression for the ultrasound pressure applied to piezoelectric receiver by considering the constituent equation of the piezoelectric transducer [79, 80] at resonance:

$$P = \frac{R_p}{A}u + \frac{n}{A}\left(V_X + \frac{i_p}{C_c f}\right) \tag{4.8}$$

In the next section, we will derive the expression of the frequency response transfer function of the piezoelectric transducer connected to the PTAT receiver.

4.2.2 Derivation of the ultrasound receiver transfer function

For the circuit shown in Fig. 4.2 (a), the constituent equations of the piezoelectric transducer are given by:

$$i_p = nu - C_p\dot{v}_p \tag{4.9}$$

$$PA = Zu + nv_p, \tag{4.10}$$

where Z and i_p from the Fig. 4.2 (a) can be represented as:

$$Z = R_p + j(\omega m_p - K_p/\omega)$$

$$i_p = C_c(v_p - V_X)^{\cdot}$$

Substituting $\dot{v_p} = \frac{i_p}{C_c}$ in Equation (4.9) and Z in Equation (4.10) in time domain leads to the following:

$$i_p = nu - \frac{C_p}{C_c} i_p \tag{4.11}$$

$$m_p \dot{u} + R_p u + K_p \int u dt = PA - n v_p \tag{4.12}$$

Equation (4.11) can be rewritten as:

$$u = \frac{1}{n}(1 + \frac{C_p}{C_c}) i_p \tag{4.13}$$

Also, since

$$v_p = \frac{1}{C_c} \int i_p dt, \tag{4.14}$$

We can substitute Equations (4.13-(4.14) into Equation (4.12) to obtain the following frequency response:

$$(m_p j\omega + R_p + \frac{K_p}{j\omega})(\frac{C_c + C_p}{nC_c})I_P(\omega) = P(\omega)A - \frac{n}{C_c j\omega}I_p(\omega) \tag{4.15}$$

$$\implies [n^2 + (K_p - m_p\omega^2)(C_c + C_p) + jR_p\omega(C_c + C_p)]I_P(\omega)$$

$$= jnC_cA\omega P(\omega) \tag{4.16}$$

The transfer function is thus given by:

$$\left|\frac{I_p(\omega)}{P(\omega)}\right| =$$

$$\frac{nC_cA\omega}{\sqrt{[n^2 + (K_p - m_p\omega^2)(C_c + C_p)]^2 + [R_p\omega(C_c + C_p)]^2}} \tag{4.17}$$

Also, the lower band ultrasound pressure at resonance (P_{fixed}), can be obtained from Equation (4.10) when $i_p = \frac{25mV}{R}$, as follows:

$$P_{fixed} = \frac{R_p}{A}u + 0.025(1 + \frac{1}{RC_cf})\frac{n}{A} \tag{4.18}$$

It can be seen from Figure 4.2 (b) that for a fixed pressure amplitude value of 10 kPa, at resonance, the peak value of the generated current I_p significantly changes with R_p using the parameter values shown in Table 4.1. P_{fixed} is thus linearly proportional to R_p, and the value of P_{fixed} corresponding to the non-trivial lower limit of the input current $i_p = 25\ mV/R$ for different values of R_P value can be obtained from Figure 4.2 (c) depending on the value of

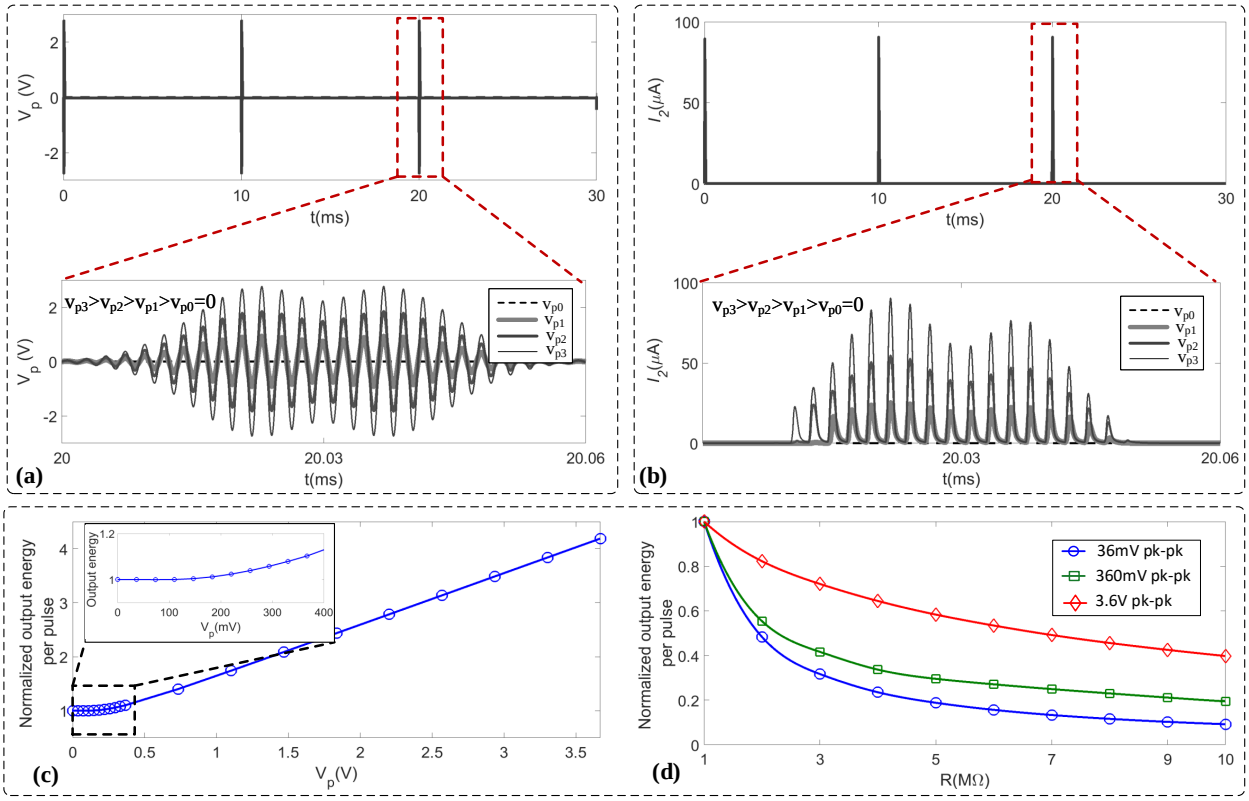

Figure 4.3: PTAT-based receiver circuit response: (a) Input voltage pulses of varying amplitude at 450 KHz and inter-pulse interval of 10 ms, when a coupling capacitor of 15 pF is used; (b) Corresponding PTAT output. Insets show the zoomed in versions of the different pulses; (c) Variation of the output energy per pulse with change in v_p, normalized with respect to the energy in the absence of any coupling input ($v_p = 0\ V$); (d) Variation of the output energy per pulse with change in the value of R for three different peak-to-peak amplitudes of the input voltage v_p, normalized with respect to the output energy when $R = 1\ M\Omega$ for each case.

R_p. The insets in Figures 4.2 (b) and (c) also show the variation of i_p and P_{fixed} respectively with R_p.

Additionally, Figures 4.3 (a) and (b) show the simulation results corresponding to different amplitudes of the input signal, using a coupling capacitance $C_c = 15\ pF$. The simulations were performed by assuming the piezoelectric crystal to have a nominal capacitance of $C_p = 1\ nF$, with a 100 Hz signal being used to mimic the piezo output. Figure 4.2 (d) shows input pulses of different amplitudes, with a 450 kHz pulsating signal having an inter-pulse

interval of 10 ms, while 4.2 (e) shows the output current of the PTAT for the same. The waveform shown in Figure 4.3 (a) very closely resembles the actual piezo output, as shown later in Section 4.4. The proposed circuit can thus track the changes in v_p very faithfully, and also produces a rectified current output whenever $i_p \leq \frac{25mV}{R}$, thus obviating the need for a rectification circuit before interfacing to the actual system. Figure 4.3 (c) shows the variation of the output energy per pulse, normalized with respect to that obtained in the absence of any input injected at node X. It can be clearly observed that the output energy bears a monotonic relation to the amplitude (and hence, the energy) of the input signal, and becomes practically linear for higher values of the input signal amplitude. Additionally, the output does not saturate for higher voltages, unlike as in the transconductance and transimpedance based receiver topologies. Figure 4.3 (d), on the other hand, shows the variation of the output energy per pulse with change in the value of the resistor R for three different values of input signal amplitude, with each case being normalized with respect to the output corresponding to $R = 1$ MΩ. We observe that the energy decreases with increase in the value of R, and the energy corresponding to a particular value of R increases with increase in the input voltage amplitude.

Note that Equation (4.7) shows that the output current is theoretically independent of temperature even though the basic PTAT circuit shows a strong dependence with respect to temperature. This is because temperature variations are considered a relatively slow process and can be compensated using adaptive sampling.

It is worth mentioning that by considering the PTAT circuit poles and zeros, the proposed PTAT-based receiver has a band-pass frequency response as shown in Fig. 4.4, where the frequency bandwidth can be controlled by selecting the right value of the coupling capacitance C_c based on the required frequency range and the suppressing of the out-of-band

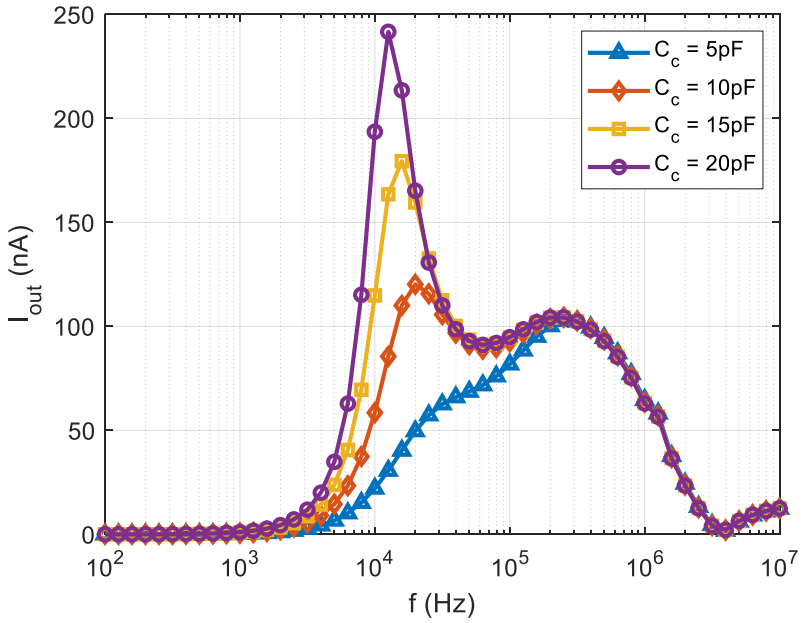

Figure 4.4: Simulation results of the frequency response of the PTAT-based receiver when its input is connected to the coupling capacitor Cc and the amplitude of the input voltage is 150 mV, with $R = 1M\Omega$.

components such as motion artifacts associated with the mechanical vibrations of the plate that can be picked up by the piezoelectric transducer. Figure 4.5 (a) and (b) show variation of the output current I_{out} of the PTAT-based and TCA-based receivers respectively with change in the value of input voltage V_{in} for four different values of the coupling capacitance C_c, when $R = 1M\Omega$ and the input frequency is 450 kHz. Whereas C_c does not have a significant effect on the sensitivity of the TCA-based receiver, it has a significant effect on the sensitivity of the PTAT-based receiver, especially at higher values of V_{in}. Figure 4.5 (c) and (d) similarly show variation of the output current I_{out} of the PTAT-based and TCA-based receivers respectively with change in the value of input voltage V_{in} for five different values of the resistance R, when $C_c = 15\ pF$. We can observe that, the same sensitivity value of $S = 0.11\ nA/mV$ can be achieved when $R = 15\ M\Omega$ for the PTAT-based receiver and

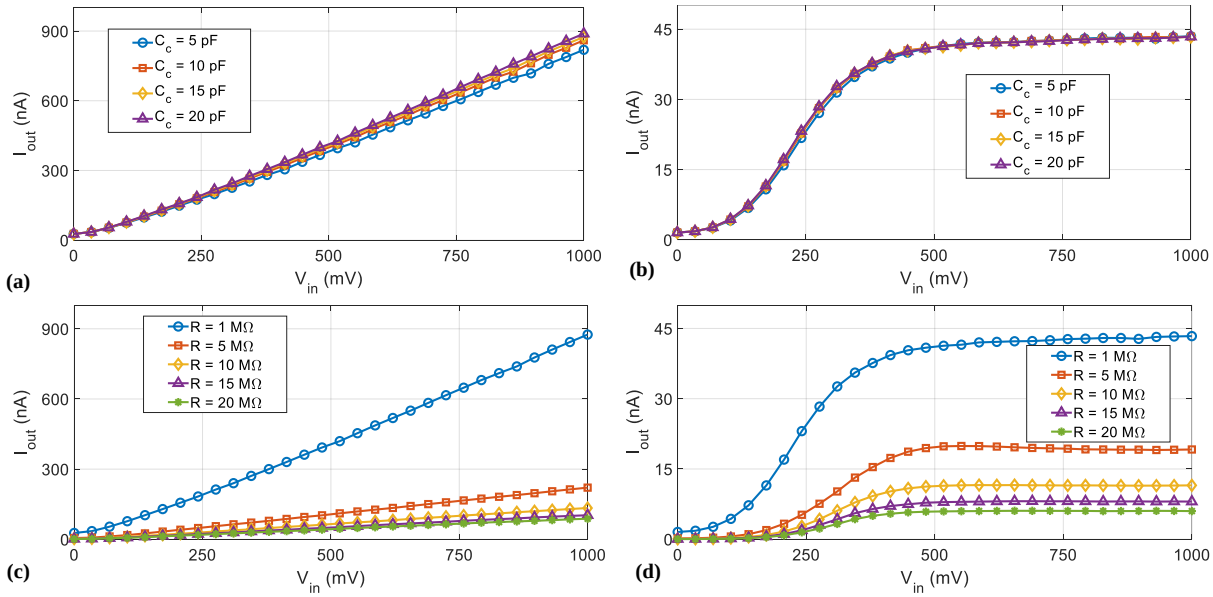

Figure 4.5: Simulation results showing the variation of the output current I_{out} of the PTAT-based and TCA-based receivers respectively with change in the value of input voltage V_{in}, for a signal frequency of 450 kHz: (a) I_{out} variation of the PTAT-based receiver for four different values of the coupling capacitance C_c when $R = 1\ M\Omega$; (b) I_{out} variation of the TCA-based receiver for four different values of the coupling capacitance C_c when $R = 1\ M\Omega$; (c) I_{out} variation of the PTAT-based receiver for five different values of the resistance R, when $C_c = 15\ pF$; (d) I_{out} variation of the TCA-based receiver for five different values of the resistance R, when $C_c = 15\ pF$.

$R = 1\ M\Omega$ for the TCA-based receiver configuration. This would lead to a power dissipation of 17 nW for the PTAT-based receiver, and a dissipation of 340 nW for the TCA-based receiver.

4.3 Circuit Implementation of PTAT receiver

We have prototyped an ultrasonic receiver based on the proposed PTAT configuration, as shown in Figure 4.6 (b). For purposes of comparison and benchmarking, I have also prototyped a TCA-based receiver [24, 81], as shown in Figure 4.6 (a) that I used it before for different substrate computing and ultrasound communication as I explained in chapter 3. Note that two stage operational transconductance amplifier (OTA) is the common modality used to design the operational preamplifier for ultrasound transducers [82, 83] However, since reducing the complexity and power consumption of the OTA is the main goal of this paper, we have used a telescopic cascode OTA (TCA) to compare it with the proposed PTAT-based receiver topology. The die micrograph of the fabricated chip (0.5 μm CMOS process) containing both the receiver topologies is shown in Figure 4.7.

The TCA-based receiver circuit topology shown in Figure 4.6 (a) consists of a current reference circuit shown in Figure 4.6 (b) which generates the bias current for the transconductor formed by the pMOS transistors $P_1 - P_5$ and the nMOS transistors $N_1 - N_4$. Diodes D_1 and D_2 implement a rectifying operation to produce the I_{out}. Note that the input of the transconductor is biased using a resistive divider (R_1 and R_2), whose values need to be chosen to provide a good impedance match to the piezoelectric transducer. The PTAT-based receiver configuration, shown in Figure 4.6 (b) uses cascoded topologies to reduce the effect of output impedance and uses a standard startup circuit configuration formed by N_6, N_7 and

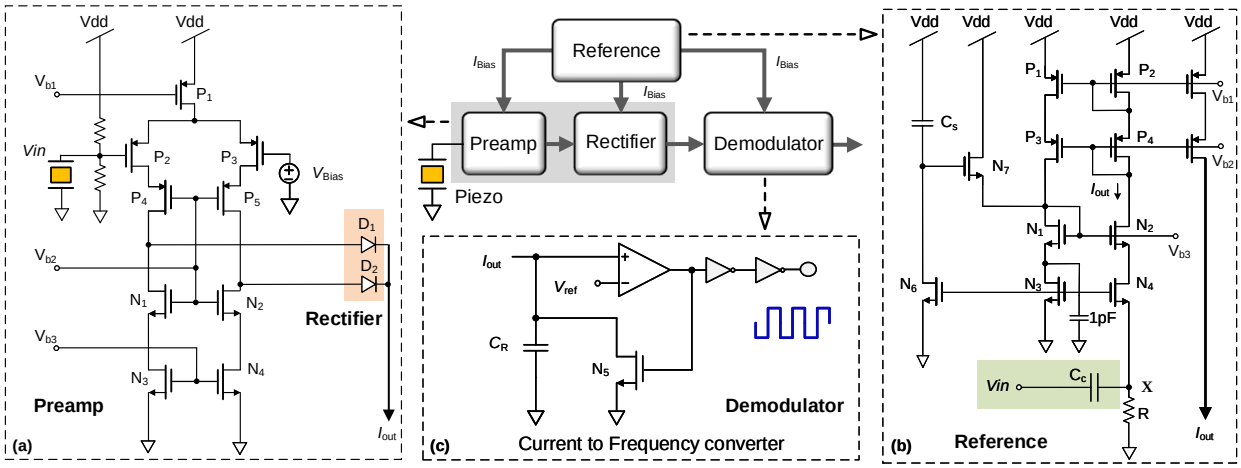

Figure 4.6: System level architecture of two different receiver circuit configurations (a) Transconductance based; (b) PTAT reference based receiver circuit topology, and (c) Current to frequency converter (Demodulator). The proposed PTAT based reference topology incorporates the preamplification and rectification stages directly within the reference circuit module.

the capacitor C_s. The piezoelectric transducer is interfaced to the PTAT resistor R through a coupling capacitor C_c. Both R and C_c can be adjusted to control the sensitivity of the receiver.

In each of the PTAT-based and TCA-based topologies, the output current is then integrated over the capacitor C_R (1 pF) shown in Figure 4.6 (c), and the integrated voltage thus produced is proportional to the total energy in the received ping. Once the integrated energy value exceeds the receiver voltage threshold V_{ref} (1.5 V), C_R is discharged by the nMOS transistor N_5. The frequency of the generated pulses is therefore proportional to the received energy and can be used to detect a received pulse. In both of these topologies, the sensitivity of the receiver can be adjusted by changing the biasing current or by varying V_{ref} or by adjusting the value of C_R [24]. Figure 4.8 shows the linear relationship between the demodulator output frequency and input current I_{out} when $R = 1\ M\Omega$ and $V_{ref} = 1.5\ V$.

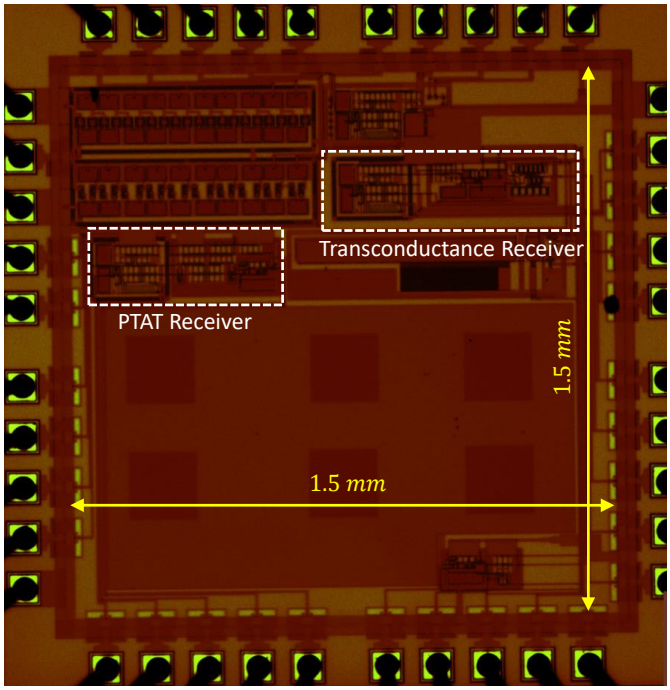

Figure 4.7: Micrograph of the prototypes for Fig. 4.6 fabricated in 0.5 μm CMOS process.

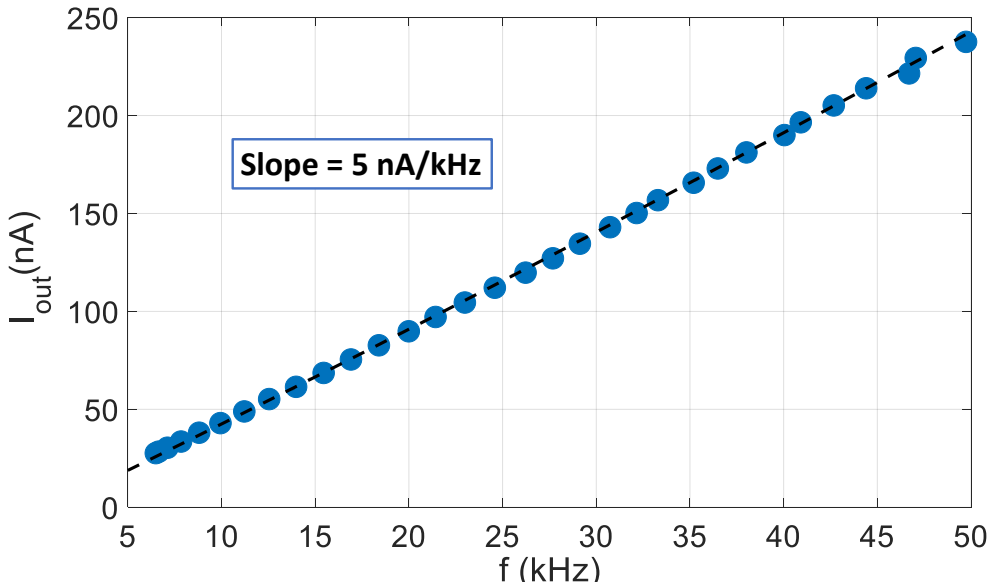

Figure 4.8: Simulation results of the input/output relationship of the modulator shown in Figure 4.6 (c), when $R = 1\ M\Omega$ and $V_{ref} = 1.5\ V$.

It should be noted here that for both the implementations, the PTAT current reference can be tuned by externally connecting a series or a parallel resistor to the internal resistor R (=1.5 MΩ). Since the output of both receivers is in the form of pulse trains, a digital signal processor can be used to decode the received digital data.

4.3.1 Noise Analysis of the PTAT Receiver Circuit

In this section, we present the noise analysis for the PTAT based receiver circuit and compare that with the TCA based receiver circuit using the models shown in Figure 4.6 (a) and (b) respectively, where the noise contribution of the cascoded transistors to the output is considered to be negligible, especially at low frequencies [77]. The 1pF capacitor of the PTAT receiver shown in Figure 4.6 (b) shunts the noise generated by the transistor N_3 to the ground. We will assume that the input referred noise will be dominated by only the thermal noise [84, 85], even though the effect of flicker-noise could also be incorporated [86, 87].

The input-referred noise voltage and noise current for the PTAT-based receiver circuit shown in Figure 4.6 (b) can be expressed as:

$$V_{n,in}^2 = 8kT\gamma\left(\frac{g_{mP2}}{g_{mN4}^2} + \frac{1}{g_{mN4}}\right) + \frac{4kT}{Rg_{mN4}^2}$$

$$I_{n,in}^2 = \frac{8kT\gamma}{R^2}\left(\frac{g_{mP2}}{g_{mN4}^2} + \frac{1}{g_{mN4}}\right) + \frac{4kT}{R^3 g_{mN4}^2} \tag{4.19}$$

Hence the total input referred noise voltage of the PTAT based topology due to $V^2_{n,in}$ and $I^2_{n,in}$ for a source impedance Z_s can be represented as:

$$V_{n,in,total} = \frac{V_{n,in}R + I_{n,in}Z_sR}{R + Z_s} \tag{4.20}$$

Notice that the input-referred noise voltage is independent of the preceding stage Z_s [77]. For typical values $(W/L) = 3$, $I_2 = 1.67\ nA$, $\mu_n C_{ox} = 50\ \mu AV^{-2}$, $\gamma = 1$, and $R = 15\ M\Omega$, the transconductance can be found to be $g_m = 0.708\ \mu AV^{-1}$, and the total input referred noise voltage therefore to the PTAT based receiver topology is $V_{n,in,total} \approx 35.3\ nV/\sqrt{Hz}$.

$$V^2_{n,in} = 8kT\gamma(\frac{1}{g_{mP3}} + \frac{g_{mN5}}{g^2_{mP3}}) + \frac{I^2_{n,PTAT}}{g^2_{mP3}} \tag{4.21}$$

where $I^2_{n,PTAT}$ is the PTAT reference output noise current given by

$$I^2_{n,PTAT} = 8kT\gamma(g_{mP2} + g_{mN4}) + \frac{4kT}{R} \tag{4.22}$$

For the same typical values of Equation (4.19), with the current $I_2 = 25\ nA$ and $g_m = 2.7386\ \mu AV^{-1}$ to achieve same sensitivity $(0.11\ nA/mV)$, the input referred noise from Equation (4.21) is $416.7\ nV/\sqrt{Hz}$.

In addition to higher level of input referred noise and lower energy-efficiency, the TCA circuit configuration also suffers from limited dynamic range leading to a non-linear output response. The performance comparison of the proposed PTAT-based receiver and the transconductance-based receiver is concluded in Table 4.2.

Table 4.2: Performance comparison of the proposed PTAT-based receiver and the TCA-based receiver.

Property	PTAT	TCA
Circuit dimensions	$0.55 \times 0.2\ mm^2$	$0.72 \times 0.2\ mm^2$
Power dissipation for same sensitivity ($0.11nA/mV$)	$0.017\ \mu W$	$0.34\ \mu W$
Circuit performance	linear	nonlinear
Input referred noise	$35.3\ nV/\sqrt{Hz}$	$416.7\ nV/\sqrt{Hz}$

4.4 Measurement Results

4.4.1 Experimental Setup

Characterization of the ultrasound receiver was performed using an experimental setup consisting of two 5 mm diameter, 475 kHz resonance frequency piezoelectric transducers (PZT-5H) implanted on a rectangular aluminum plate (300 mm x 200 mm x 1.5 mm). An illustration of the setup is shown in Figure 4.9 (a), where one of the piezo transducers was connected to a function generator (RIGOL DG4102, 100 MHz Arbitrary Waveform Generator) that emulates the transmitter Tx, while the other transducer was connected to an oscilloscope (Tektronix MSO 2004B, 70 MHz Mixed Signal Oscilloscope) to act as the receiver Rx. We characterized the effect of the separation d between the transmitter and receiver PZT transducers on the receiver voltage.

Figure 4.9 (b) shows the variation in the voltage at the receiver piezo crystal when the distance of transmitting crystal is varied from 5-40 cm for a 20 V, 450 kHz sine wave applied

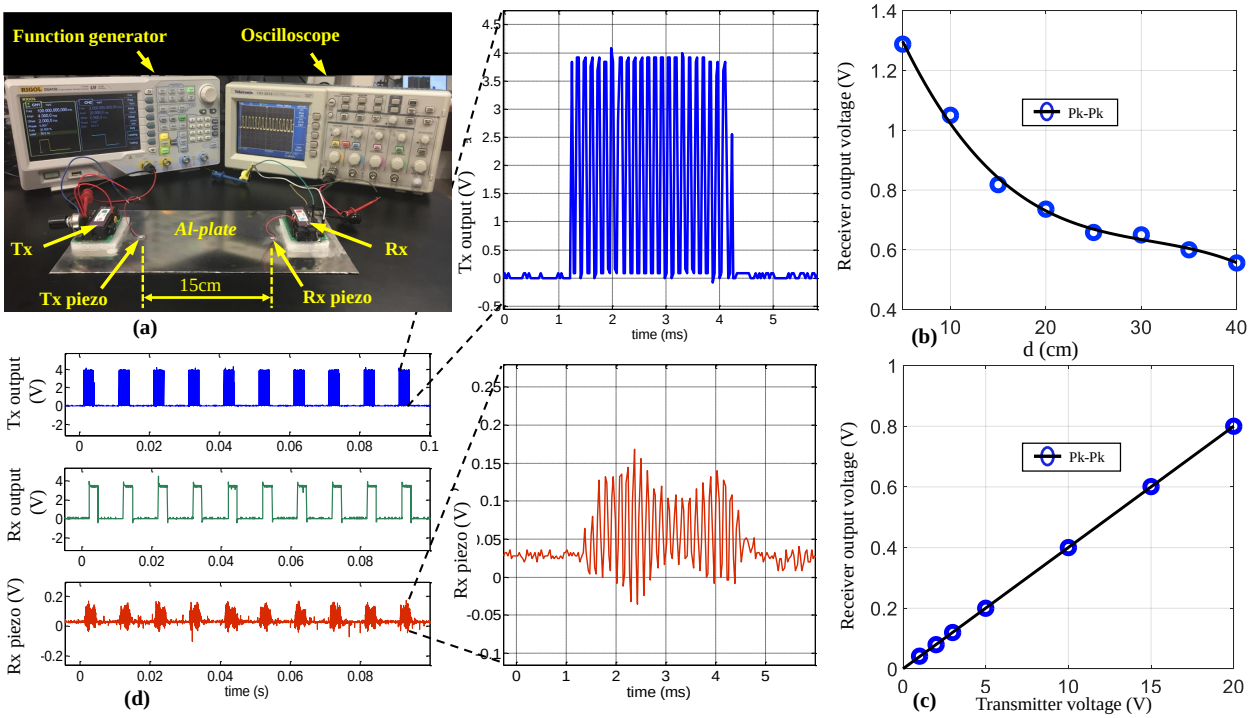

Figure 4.9: (a) Experimental setup consisting of aircraft grade aluminum plate with transmitter and receiver piezoelectric transducers, connected to the proposed receiver circuit; (b) The variation in the received voltage when the transducer distance is varied from 5-40 cm with 20 V peak-to-peak applied voltage; (c) Receiver voltage variation when the applied voltage is varied from 0-20 V with an inter-crystal separation of 15cm; (d) Transmitter and receiver pulses shapes.

as input to the transmitter. The variation in the receiver voltage when the applied voltage to the transmitter is varied from 0-20 V peak-to-peak , while maintaining a constant frequency of 450 kHz and a constant separation of 15 cm between the crystals is shown in Figure 4.9 (c). It is thus evident from Figure 4.9 (b) that an inter-crystal separation of 15 cm is enough to generate a detectable ultrasound wave by applying a short pulse at a specific frequency. The amplitude of the ultrasonic wave generated by the receiver is in the range of 150 mV, and the detection performance depends on the sensitivity of the receiver circuit.

4.4.2 Receiver Characterization

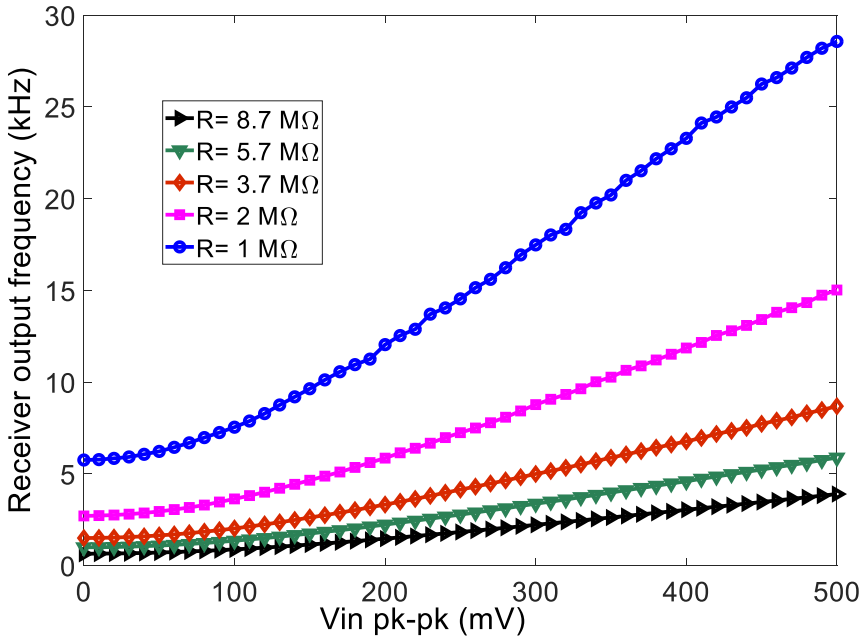

Figure 4.10: The sensing of the received signal at different resistance values.

The performances of the prototyped PTAT-based and TCA-based receiver circuits shown in the micrograph in Figure 4.7 were characterized using a similar methodology as described in the previous section. Figure 4.9 (d) shows the pulses generated by the PTAT receiver corresponding to data transmitted using ON-OFF keying, also illustrated in Figure 4.9 (d). For each case, the receiver output is encoded by the frequency of the waveform generated by the current to frequency converter. It can be seen from Figure 4.9 (d) (inset) that there is a latency of about 25 μs between the transmitted and received pulses, which confirms that ultrasound communication over a 15 cm link distance in the aluminum plate (through which sound travels at around 6000 m/s) is feasible. An MSP430 microcontroller (not shown in the figure) was used to generate the digital data for transmission and as well as for analyzing the received digital data from the receiver output, based on a preprogrammed protocol. Figure 4.10 shows the variation of the output frequency of the receiver with

variation in the transmitted signal for different values of internal resistance value of the PTAT. A comparison of the receiver response using the transconductance-based and PTAT-based topologies is shown in Figure 4.11. Figure 4.11 shows that the output frequency of the PTAT-based receiver for biasing current 25 nA is linearly proportional to the input signal and has a sensitivity of 21 Hz/mV, while the inset in Figure 4.11 for the same biasing current shows that the transconductor based topology exhibits saturation due to the dynamic range limitations of the transconductance amplifier, and has a much lower sensitivity of 4 Hz/mV. The experimental observations are consistent with the simulation results as well, thus proving the validity of the proposed circuit for deployment as an ultrasonic receiver. The sensitivity of the receiver can also be controlled by adjusting the external coupling capacitor and/or resistor in the high pass filtering module in the PTAT topology. It should however be noted that the receiver output for the PTAT based receiver will practically saturate due to limitations of the current to frequency converter circuit, and the sensitivity can be increased by improving the converter design.

4.4.3 Bit-Error-Rate Experiments

Bit error rate (BER) performance of the proposed receiver topology corresponding to different transmitted power levels were carried out based on experimental data collected at the output of a cleaning circuit in cascade with the current to frequency converter. The cleaning circuit outputs a high or a low pulse, depending on whether the frequency of the signal at the frequency converter output is above or equal to its baseline frequency. The results obtained (using the experimental setup described in Subsection (4.4.1) by transmitting 20 s of alternate high and low pulses at a frequency of 300 Hz have been shown in Figure 4.12, with the transmitted power being calculated in terms of the transmitter voltage normalized

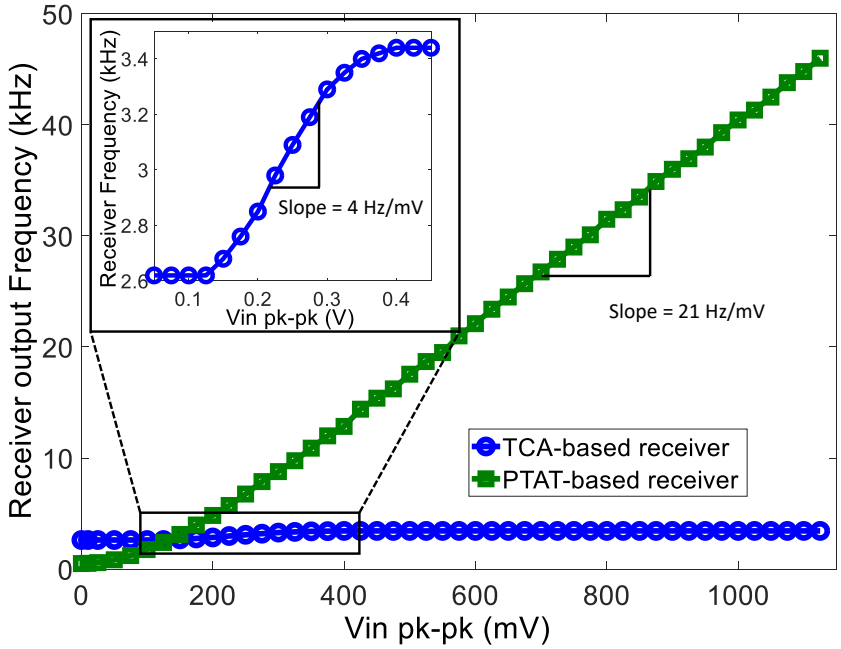

Figure 4.11: Comparison between PTAT and TCA based receiver responses; (inset is a zoomed in version of the TCA receiver sensitivity for lower voltages), for the same biasing current, when $I_{Bias} = 16.67nA$ (which corresponds to $R = 1.5M\Omega$).

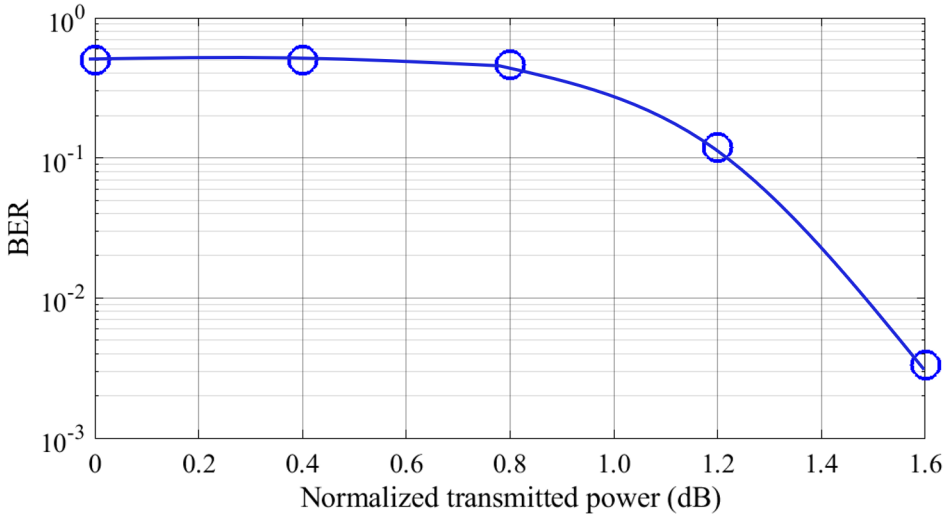

Figure 4.12: Variation of the BER with the SNR calculated using transmitter voltage values normalized with respect to a baseline level.

with respect to a baseline voltage of 2 V. It can be observed that the BER monotonically decreases with increase in the transmitted power, thus validating the feasibility of using the PTAT based receiver configuration for ultrasound communication.

4.5 Summary

In this chapter we presented the feasibility of using a PTAT-based current reference circuit as a wide-dynamic-range ultrasound receiver and low complexity biosensor. The dynamics of the receiver confirms to the dynamics of fixed-point circuits and thus the system stability is guaranteed at all points of time because of the inherent tendency of the network to settle to its fixed point(s). Compared to the standard ultrasonic receiver circuit topologies existing in the literature, the proposed PTAT-based receiver not only demonstrates significantly higher dynamic range, increased sensitivity, lower power dissipation and reduced form-factor, but also demonstrates increased linearity of operation. Additionally, it produces a rectified current output which can be readily fed to the frequency conversion circuitry, thus obviating the need for a separate rectification stage downstream from the PTAT circuit. The BER plots obtained from experimental results further corroborate the feasibility of using the proposed PTAT based receiver circuit in ultrasound communication.

It is envisioned that the receiver will be integrated with a digital processor which will be programmed to process the produced digital output. The processor will also be programmed to implement communication protocols that can be used to form a sensor network inside the substrate such that important information related to the health of the structure can be reliably communicated. On integrating our PTAT-based receiver with a digital processor programmed to implement communication protocols, each resulting module can be used

to form an independent node in a sensor network inside the substrate such that important information related to the health of the structure can be reliably communicated [81]. Moving forward, we would like to develop a decentralized substrate communication network with each agent communicating exclusively with the substrate for exchanging information, while maintaining the network stability. Also, we will optimize the biosening functionality in terms of stability and selectivity of the sensing element.

The PTAT circuit can also be used for designing a low complexity and compact sensing element for a wide range of applications. For example, in the future we will combine our proposed self-capacitance based WPT technology with a PTAT-based resistive and/or capacitive biosensor for measuring physiologically relevant data for the human oral cavity. Figure 4.13 shows a vision of an oral cavity wireless PTAT-based biosensor as an electronic-tooth to be used for sensing important biomarkers from the saliva and sending the data wirelessly to the reader for postprocessing purposes. The biosensor and the wireless demodulator are powered by the SC-based WPT shown from the figure.

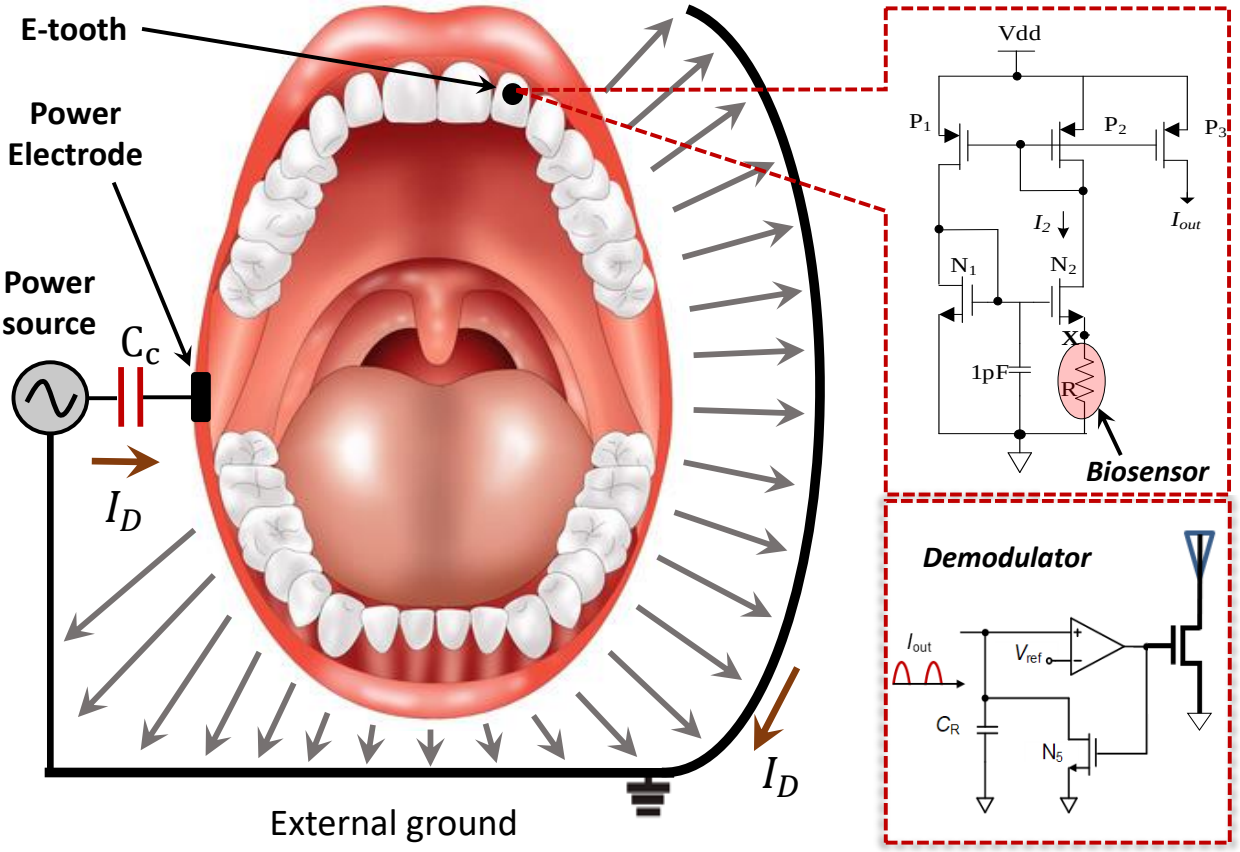

Figure 4.13: The concept of the Self-Capacitance based wireless power transfer WPT showing the flow of the displacement current I_D through the conductive part of the oral cavity feeding the PTAT-based biosensor mounted on a tooth and flows back through a fictitious ground [1].

Chapter 5

Extending SC-WPT for Substrate Computing

In chapter 2, we defined the self-capacitance as an intrinsic property of any electrically isolated body. The isolated body could be any conductive substrate. In this chapter, I show some examples of wearable and implantable electronic devices that are used for substrate computing (e.g. communications and sensing), and the substrate here represents any electrically isolated conductor (e.g. animal tissue or conductive metal) that can be used to deliver the power wirelessly to these wearables through the proposed self-capacitance based WPT technique. The results of this chapter are based on [24, 81].

5.1 Self-powered System-on-Chip for Substrate Computing and Ultrasonic Communications

Advances in miniaturization are enabling novel sensing technologies that promise breakthroughs in all areas of science and engineering. Nowhere is the impact more evident than in

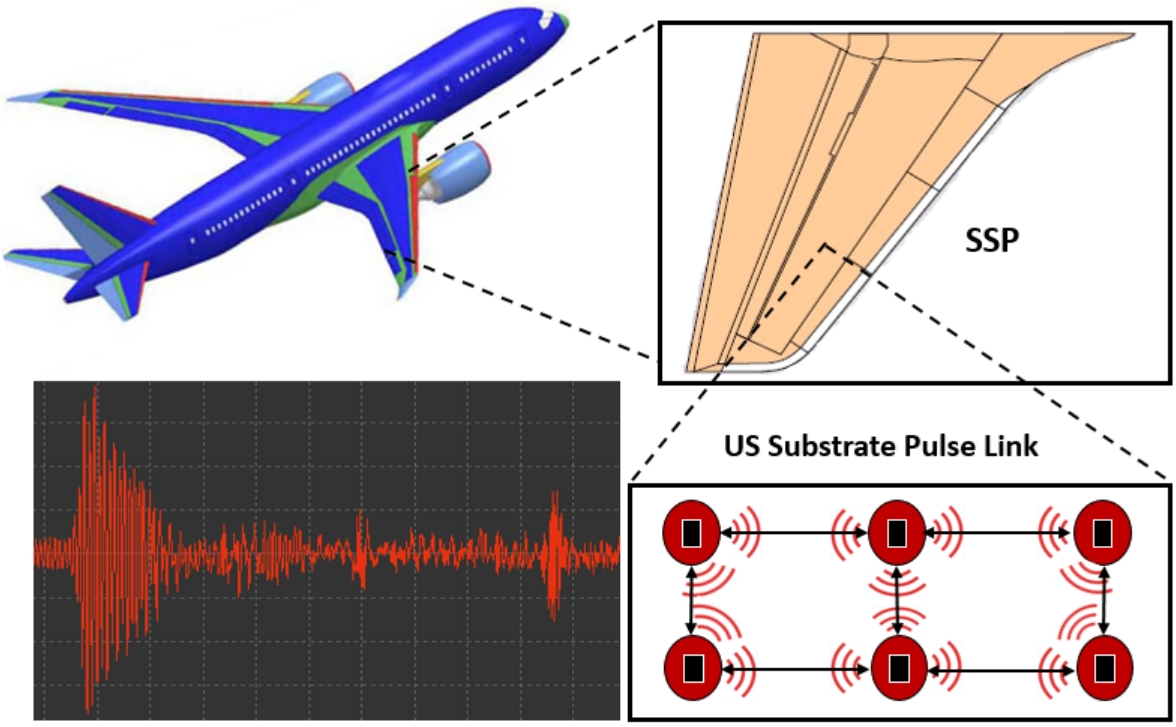

Figure 5.1: The concept of smart substrate plates (SSPs) with a fabric of embedded sensors. The sensors operate by harvesting energy from ambient vibrations in the substrate and communicate through the substrate using ultrasonic pulses. Large-structures like an aircraft wing can be assembled without the need to separate instrumenting the sensors. (Aircraft image source: Google image).

the area of structural engineering where the integration of "smart" sensors with novel materials fabrics is promising a new generation of "smart" structures that can potentially "sense", "feel" and "diagnose" its structural state [88]. The grand-vision, as illustrated in Figure 5.1, is that without the aid of batteries or remote powering, these sensors would harvest the power directly from the host structure and continuously monitor the statistics of different sensory conditions like localized strain, temperature, moisture content, aerodynamic shear stress and pressure [89]. Due to their low-cost and small form factor these micro-sensors could be embedded inside hard-to-access structural components such as rotors of aircrafts, aircraft wings, and turbine blades, without compromising the structural or aerodynamic integrity of

the host structure. The ubiquitous nature of these sensors will be complemented by their ability to compute, make decisions locally and transmit any impending mechanical failure events remotely. The fabric of embedded sensors will also facilitate organic assembly of such large synthetic structures through the use of "smart substrate plates" (SSPs) [90]. Without the need for post-construction subsystem enhancements like sensor deployment, wiring or wireless networking, these"plates" are able to compute, detect anomalies and communicate events seamlessly through the structure substrate. In this section we present the design of a CMOS transceiver that can be used for through-substrate communications in SSPs using an ultrasonic data link (i.e., without a separate medium such as radio or embedded wire) – all using harvested power from its own ambience such as mechanical vibration. The use of through-substrate communications also makes the design immune to electromagnetic jamming and interference and the ability to harvest its operational energy from ambient vibration obviates the need for sensor maintenance.

5.1.1 Circuit Implementation of SSP Transceiver

The system level architecture of a complete SSP transceiver is shown in Figure 5.2. The transceiver comprises of different energy harvesting and telemetry modules namely: (a) a voltage multiplier; (b) a voltage regulator; (c) an ultrasound transmitter; and (d) an ultrasound receiver. The circuit schematic of each of these modules are also shown in Figure 5.2. The transceiver interfaces with three piezoelectric transducers type Lead Zirconate Titanate (PZT), one for harvesting energy from mechanical vibrations and the other two are used for ultrasonic telemetry. A standard Dickson voltage multiplier (shown in Figure 5.2) is used for rectifying and boosting the output of the harvesting transducer onto a storage capacitor. A

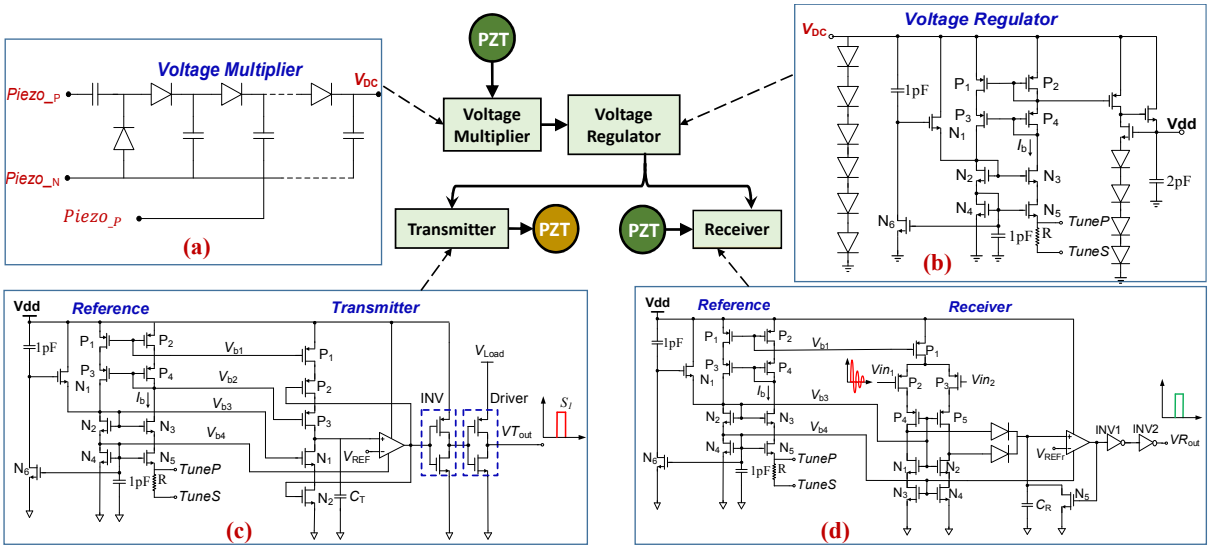

Figure 5.2: System level architecture of the SSP transceiver comprising of the voltage multiplier, regulator, piezoelectric driver and ultrasonic receiver. (a) a voltage multiplier; (b) a voltage regulator; (c) an ultrasound transmitter; (d) an ultrasound receiver.

linear regulator is then used to filter out the voltage ripples and deliver current to the transmitter and receiver modules. The implementation is based on a relaxation oscillator circuit which generates a sequence of ultra-wide-band (UWB) pulses based on an OOK modulation. A standard proportional to absolute temperature PTAT externally circuit topology has been used to generate the bias voltages V_{b1} - V_{b4} and also provide additional voltage regulation. Note that for this implementation, the PTAT can be tuned by externally connecting a series (to node TuneS) or a parallel resistor (to node TuneP) to the internal resistor R (1.5 MΩ). For the transmitter, the frequency of the output pulses is determined by the comparator reference voltage V_{REF}, the charging capacitor value C_T and by the magnitude of the bias currents generated by the reference circuit. When the integrated voltage on the capacitor C_T exceeds V_{REF}, the capacitor C_T is discharged by the transistors N1 and N2. The shape and

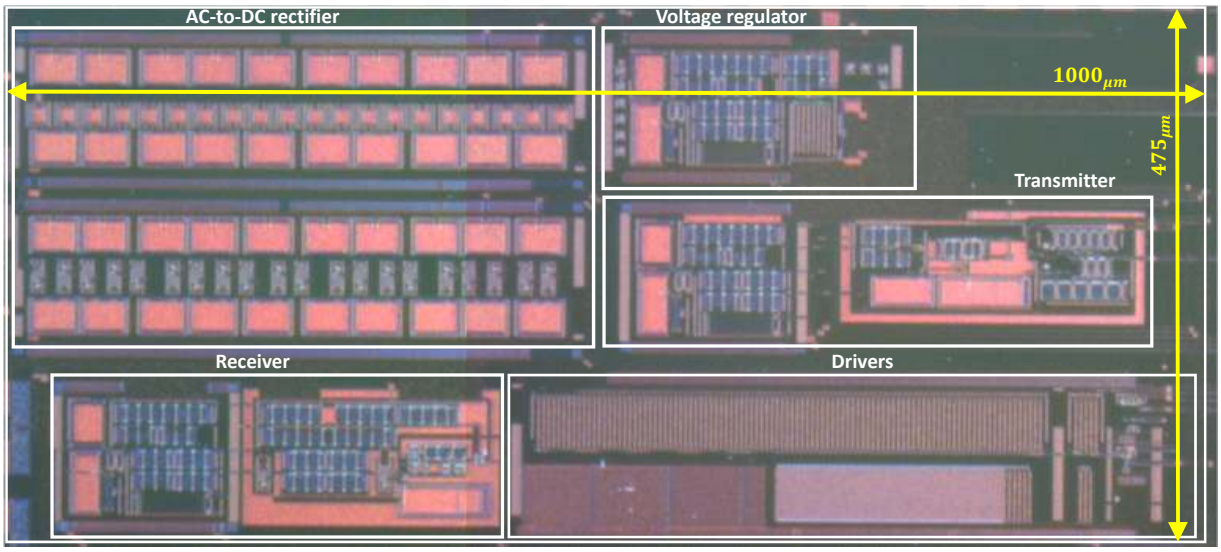

Figure 5.3: Micrograph of the prototype fabricated in 0.5μm CMOS process.

the duration of the UWB pulse is determined by the size of the discharging transistor and is important to ensure that sufficient energy is delivered by the driver to the piezoelectric transducer. The transducer forms a resonant circuit and naturally performs pulse-shaping and pulse-modulation when driven by UWB pulses.

The receiver circuit also comprises of a relaxation oscillator circuit except that the current charging the capacitor C_R is generated by a transconductor formed by the pMOS transistors P1 - P5 and the nMOS transistors N1 - N4. The two pMOS-based diodes implement a rectifying operation and the rectified current is then integrated on the capacitor C_R. Thus the integrated voltage on C_R is proportional to the total energy in the received ping. Thus, when the integrated energy crosses the threshold of the comparator, the receiver produces a digital pulse and the time interval between the pulses encodes the magnitude of the received

Table 5.1: Specifications of the self-powered transceiver.

Parameter	Specification
Circuit dimensions	$1000\mu m$ x $475\mu m$
Power dissipation	55 μW at $8KHz$ data rate
Generated DC voltage	$3.44V$
DC voltage settling time	$10s$
Regulator Dropout	$1V$
Transmitter pulse transition time	$2\mu s$
Received Voltage Range	350 mV
Receiver sensitivity	$4Hz/mV$
Material	PZT-5H Piezo-crystal
Resonance frequency	$230kHz$
Bandwidth	$\approx 200KHz$

energy. Note that the receiver transducer works as a tuned-circuit and naturally filters out-of-band interference.

5.1.2 Experimental Results

The proposed SSP transceiver circuit was prototyped in a 0.5μm CMOS process and Figure 5.3 shows the micrograph of the fabricated prototype. Each of the individuals modules were characterized and in Table 5.1 we summarize the measured specifications. In the first set of experiments we verified the functionality of the voltage multiplier and the voltage regulator. Figure 5.4 shows the measured result when the voltage multiplier is excited by a broad-band source of amplitude 800mV and with a load current of 15μA. The voltage ripples can be clearly seen around the multiplied voltage of 3.4V. The measured response of

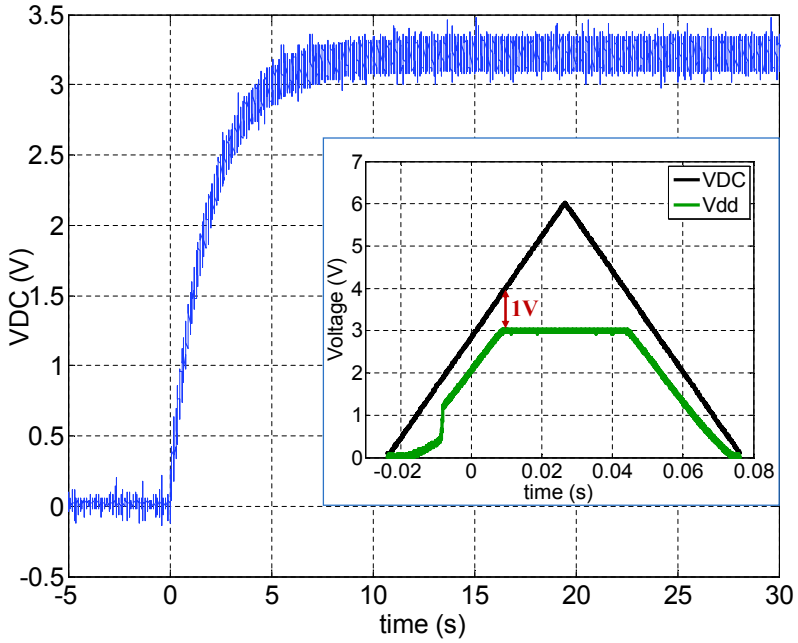

Figure 5.4: Measurement results of the voltage multiplier and drop-out regulator.

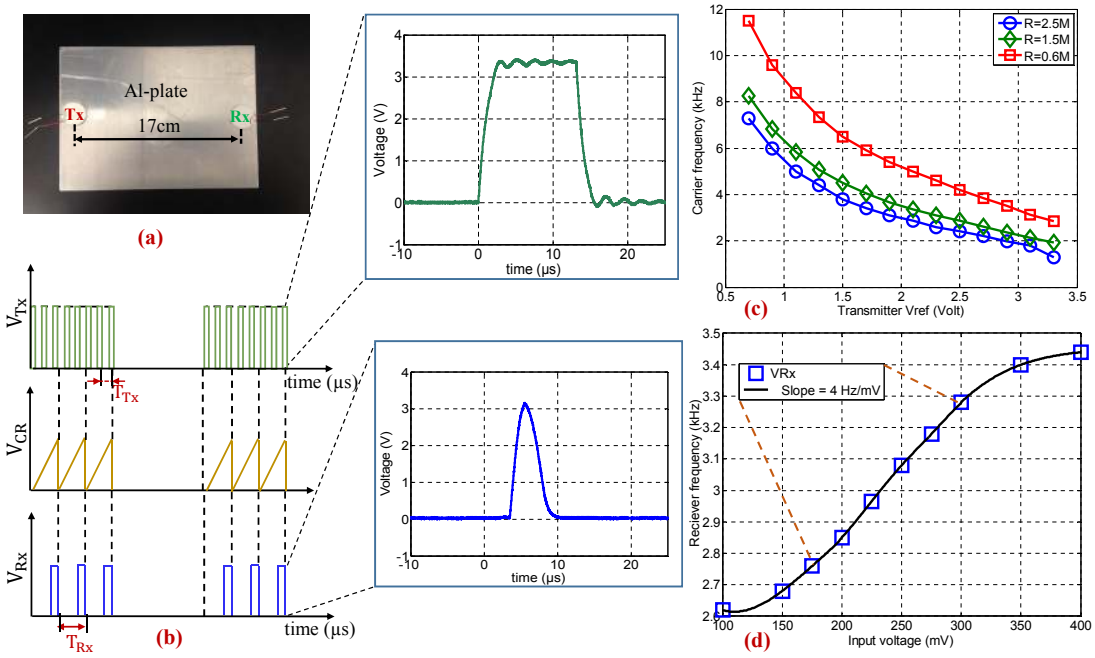

Figure 5.5: Measured results obtained using (a) prototype Aluminum SSP ; (b) transmitted and received pulse shapes ; (c) transmitter ; and (d) receiver characteristics.

the voltage regulator is shown in Figure 5.4 (inset) which exhibits a drop-out voltage of 3V at an input of 4V when driving a load of 10μA.

In the next set of experiments we characterized the performance of the telemetry circuits using a prototype of a SSP formed using an Aluminum plate shown in Figure 5.5 (a). Three 230kHz PZT-5H transducers (5mm diameter) were attached to the plate and used for harvesting and ultrasonic telemetry. The pulses generated by the transmitter and the receiver are shown in Figure 5.5 (b) (inset) in the context of data transmitted using ON-OFF keying also illustrated in Figure 5.5 (b). The frequency of pulses (inversely proprotional to T_X in Figure 5.5(b)) emitted by the transmitter can be controlled externally using the reference voltage V_{REF} as shown in the measured result in Figure 5.5 (c). Similarly, the sensitivity of the receiver can also be controlled by adjusting the external resistor of the PTAT. Figure 5.5 (d) shows the measured response of the receiver where the output frequency (directly proportional to T_R in Figure 5.5 (b)) is linearly proportional to the power of the input signal, measured at output of the receiver PZT transducer. The sensitivity of the receiver was measured to be $4Hz/mV$ which can also be controlled by adjusting the value of the resistor in the reference circuit.

5.2 Design of CMOS Telemetry Circuits for In-vivo Wireless Sonomicrometry

In this section we present the design of an integrated circuit (IC) that can be interfaced with a sub-millimeter-scale sonomicrometry crystal and can be used for bi-directional telemetry through different types of in-vivo structures (bones and tissues). In our previous work [91]

we demonstrated that a miniature piezoelectric transducer could be used to harvest energy from a diagnostic B-mode ultrasound scanner; and the harvested energy was shown to be sufficient to establish a telemetry link with the scanner. Implantation of millimeter-scale sonomicrometry crystals [92] for tissue tagging offers an advantage over echocardiography or magnetic resonance imaging in achieving a better trade-off between signal sampling rate and spatial resolution. Sonomicrometry has also been demonstrated for imaging mitral valve dynamics in the study of fine 3D geometric perturbations associated with ischemic mitral regurgitation (IMR) [2]. However, as shown in Figure 5.6 (a) [2], the current state-of-the-art sonomicrometry system requires hard-wiring of the crystals to an external data acquisition and a power source. This limits the number of sites that can be marked and also prevents the implantation of the crystals on moving structures, such as valve leaflets, and prevents implantation inside hard-to-access structures like bone-marrow. In addition, hard-wiring constrains the animals or subjects to be intubated and hence the current technology cannot be used for chronic, long-term studies.

In this section we explore interfacing the sub-millimeter sized sonomicrometry crystals with integrated circuits which will enable system miniaturization and implantation (scales of different components are shown in Figure 5.6 (b)). Figure 5.6 (b) also highlights another potential application of a wireless integrated sonomicrometry system in the area of wireless capsule endoscopy (WCE) [93]. For a WCE application, the crystal, the telemetry IC and a battery could easily fit within the size of a pill (shown in Figure 5.6 (b)) and the pill can easily be swallowed and can be made to wireless scan some vital parameters as it travels through the digestive tract. When compared to an RF based WCE, sonomicrometry based endoscopy obviates the need for aligning the transmission and receiving antennas/transducers. Also, the data from the pill can be easily integrated using a portable ultrasound device [91], leading to patient comfort. Yet another advantage of the proposed telemetry system is its ability to

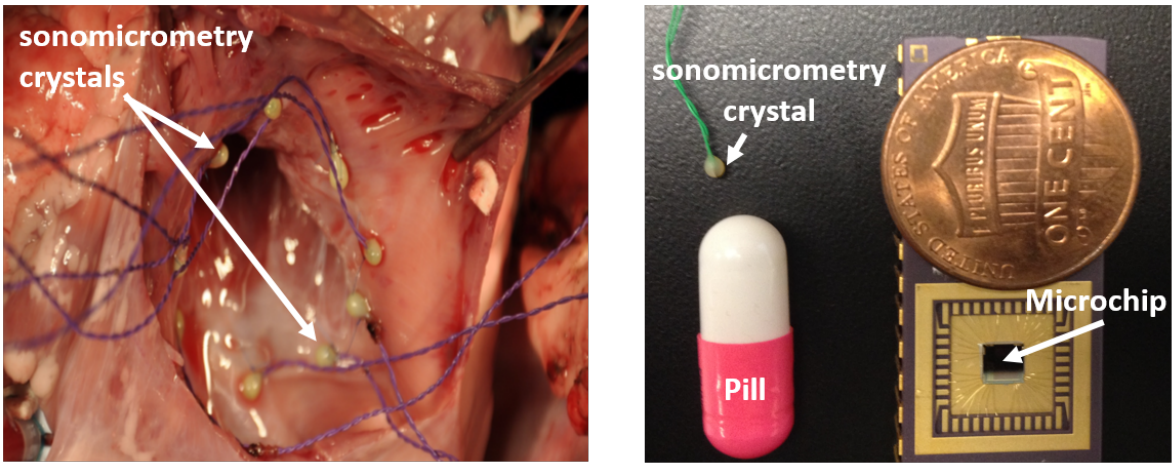

Figure 5.6: (a) Sonomicrometry crystals used for measuring mitral-valve dynamics [2]; (b) sizes of different components of a wireless sonomicrometry transceiver compared to a standard pill.

communicate with monitoring devices that could be implanted in hard-to-access regions of the body like the bone-marrow. Several studies have been reported to understand the effect of ambient conditions on the development of marrow cells, however, they have been limited to only cadavers or anesthetized animals [94].

5.2.1 Circuit Implementation

The schematic of the circuits implementing the telemetry functions are shown in Figure 5.7. It comprises of a transmitter and a receiver module as shown in Figure 5.7 (a) and Figure 5.7 (b) which are biased respectively by a reference circuit module as shown in Figure 5.7 (c). The implementation of the reference circuit follows a standard PTAT topology and generates voltage biases V_{b1}-V_{b4}. The detailed description of the PTAT reference has been omitted here for the sake of brevity. Note that for this implementation the PTAT can

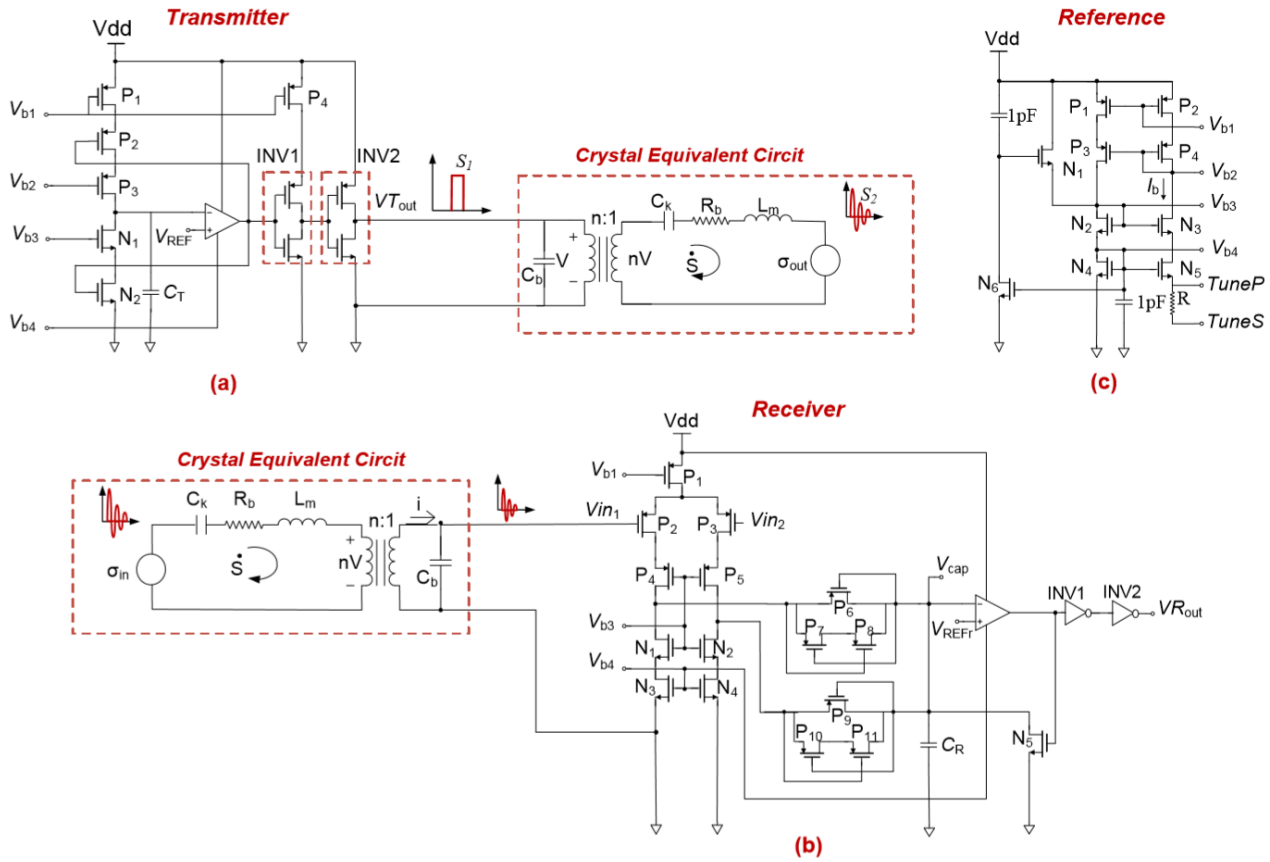

Figure 5.7: (a) Schematic of the transmitter circuit; (b) Schematic of the reciever circuit; (c) Schematic of the reference circuit.

be tuned by externally connecting a series (to node $TuneS$) or a parallel resistor (to node $TuneP$) to the internal resistor R. The architecture of both the transmitter and receiver circuits is based on our previously reported circuit topology in section 3.1 and is based on a relaxation oscillator circuit which has been modified to generate a sequence of ultra-wide-band (UWB) pulses.

For the transmitter the frequency of the output pulses is determined by the comparator reference voltage V_{REF}, by the charging capacitor C and by the bias currents generated by the reference circuit. When the integrated voltage on the capacitor C exceeds V_{REF}, the capacitor C_T is discharged by the transistor N_1. The shape and the duration of the UWB

Table 5.2: Specifications of the sonomicrometry transceiver.

Parameter	Specification
Resonant Frequency	$1.8MHz$
Material	PZT-5H Teflon coated
diameter	$1.0mm$
Crystal Capacitance	$120 - 250pF$
Bandwidth	$\approx 200KHz$
Circuit dimensions	$530\mu m$ x $600\mu m$
Received Voltage Range	$200\ mV$
Power dissipation	$611\ \mu W$ at $1KHz$ data rate

pulse is determined by the size of the discharging transistor and is important to ensure that sufficient energy is delivered by the driver chain (formed by two inverters INV1 and INV2) to the sonomicrometry crystal.

Note that the input equivalent circuit of the crystal can be modeled by a series RLC circuit with a transformer input. The transformer models the electro-mechanical coupling properties of the crystal where the load parameters is determined by the equivalent mechanical compliance of the crystal and the tissue's acoustical impedance. As illustrated in Figure 5.7 (a), the resonant circuit formed by the crystal shapes the UWB pulse S_1 into an ultrasonic ping S_2. The time interval between two acoustic pings can be controlled by the voltage V_{REF} which can be used to turn ON and OFF the transmitter.

The receiver circuit shown in Figure 5.7 (b) also comprises of a relaxation oscillator circuit except that the current charging the capacitor C_R is generated by a transconductor formed by the pMOS transistors P_1 - P_5 and the nMOS transistors N_1 - N_4. The diodes formed by transistors P_6 - P_{11} implement a rectifying operation and the rectified current is then

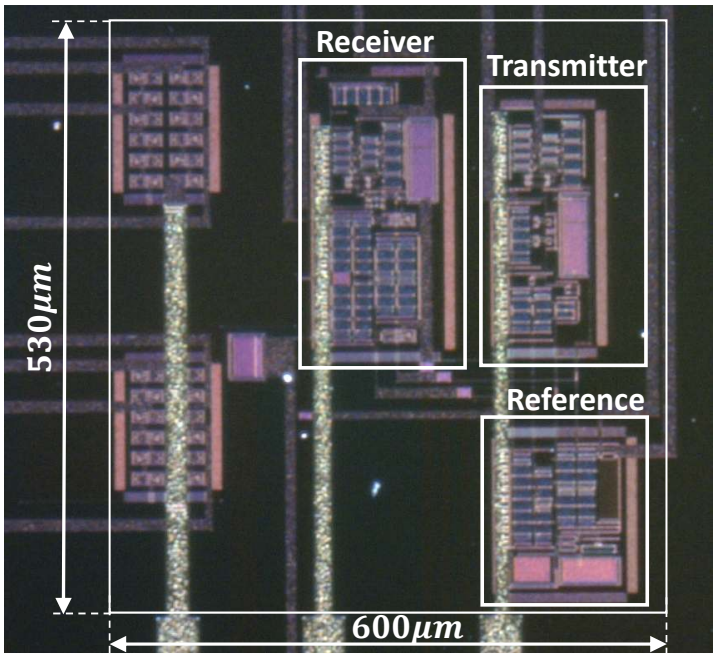

Figure 5.8: The fabricated chip.

integrated on the capacitor C_R. Thus the integrated voltage on C_R is proportional to the total energy in the received ping (as shown in Figure 5.7 (b)). Note that the bulk driven diodes in this implementation reduce the coupling of the power supply noise onto the integrating capacitor C_R. Once the integrated energy value exceeds the receiver voltage threshold V_{REFr}, C_R is discharged by the nMOS transistor N_5. The frequency of the generated pulses is therefore proportional to the received energy and could be used to detect a received pulse. Note that in this topology the sensitivity of the receiver can be adjusted by changing the input transconductance of the pMOS transistors P_2, P_3 or by varying V_{REFr} or by adjusting the value of C_R. Since the output of the receiver is in the form of pulse trains, a digital signal processor can be used to decode the received digital data.

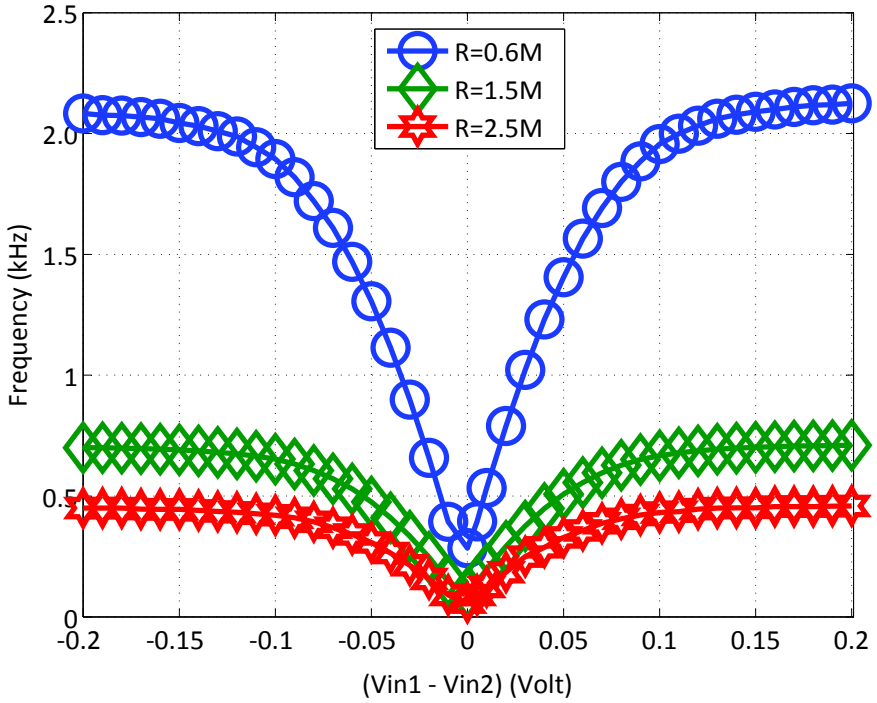

Figure 5.9: Measured response of the receiver circuit implementing a absolute value function.

5.2.2 Measured Results

A prototype of a wireless sonomicrometry transceiver was designed by integrating a commercially available sonimicrometry crystal (purchased from Sonometrics Inc.) with a telemetry circuit which fabricated in a standard 0.5-μm CMOS process. The specifications of the integrated transceiver is summarized in Table 5.2 and the micrograph of the fabricated circuit is shown in Figure 5.8.

The first set of experiments were designed to characterize the response of the receiver for different values of the input differential voltages ($V_{in}^{+} - V_{in}^{-}$). The pulses generated by the receiver were counted over a fixed time-interval to estimate the average frequency (pulses/sec). Figure 5.9 shows the measured pulse-rates for different values of the input voltages and different

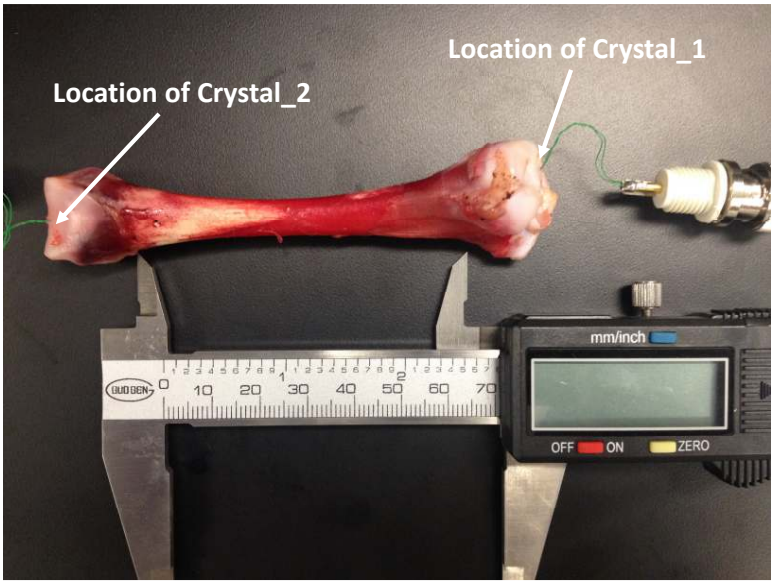

Figure 5.10: Phantom setup comprising of a femoral bone extracted from a chicken.

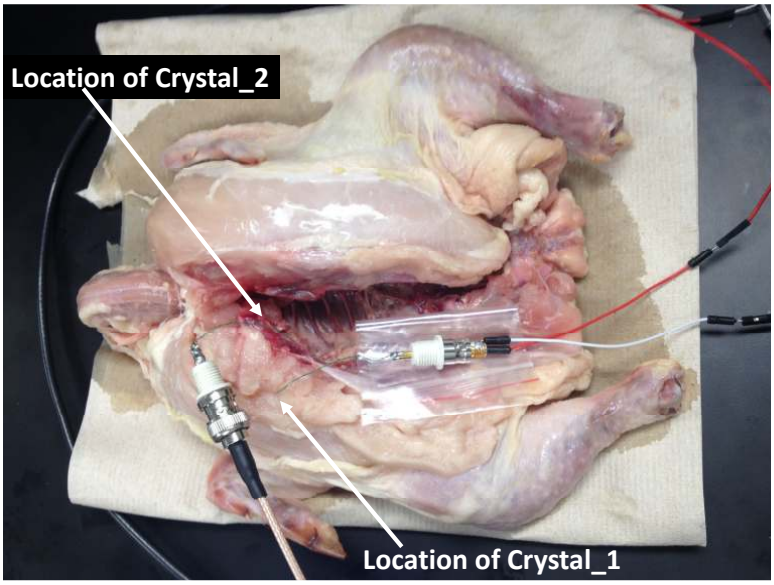

Figure 5.11: Phantom setup comprising of a whole chicken with in tact skin, muscles and bones.

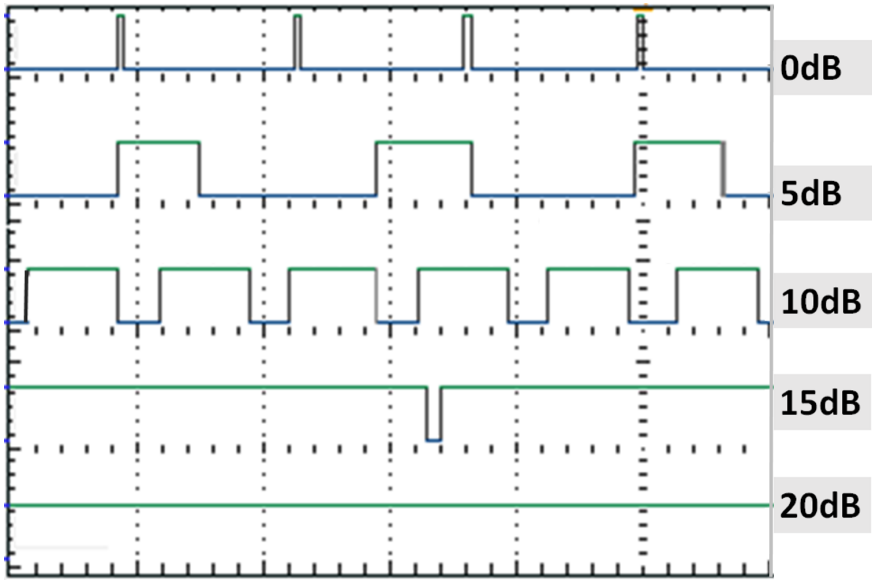

Figure 5.12: Measured receiver output waveforms for a specific phantom and for different levels of transmitted power.

values of the reference resistor R (which controls the bias current through the transconductor). The response follows an approximation of an absolute value function where the output saturates at a maximum pulse-rate that is determined by the parameters of the relaxation oscillator. The receiver circuit exhibits an imbalance between both the differential branches of the input current (due to transistors mismatch and finite drain impedance) which leads to an offset and gain mismatch in the output response, as shown in Figure 5.9.

The next set of experiments were designed to evaluate the performance of the telemetry circuits for three different phantom setups where a transmitter and receiver sonomicrometry crystal were implanted in: (a) a water bath; (b) a 7cm long bone; and (d) a chicken cadaver. Figure 5.10 and 5.11 show the pictures of the bone and chicken phantoms where the sonomicometry crystals were connected to transceiver IC using a twisted cable. To characterize the output of the receiver for different levels of input ultrasonic power, we used a commercial echoscope (GS200 by gaMPT - Frequency range $1 - 5MHz$). The echoscope automatically

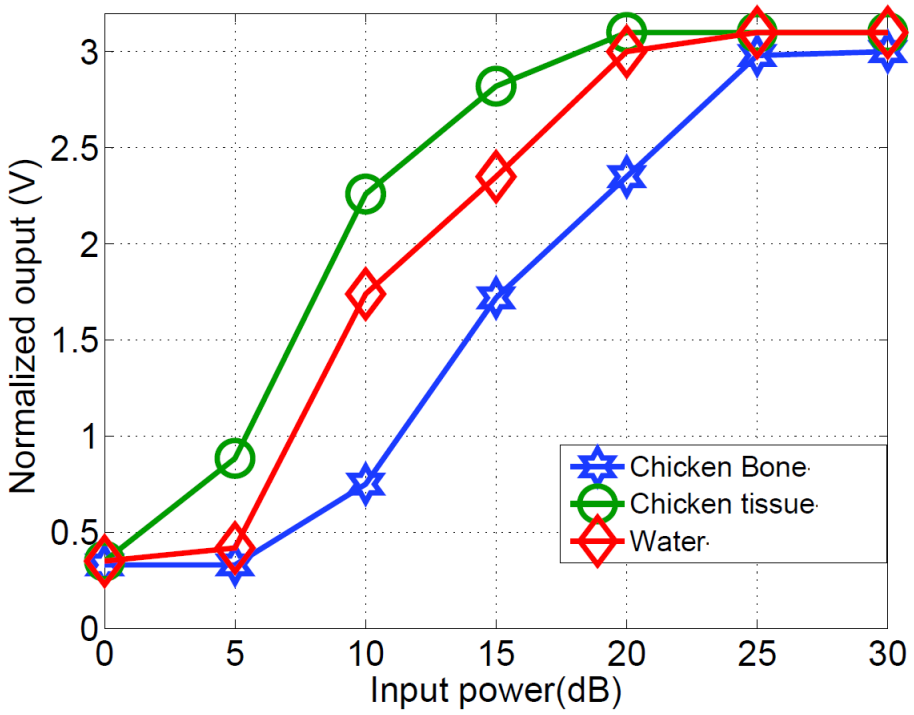

Figure 5.13: Receiver output for different levels of transmitted power and for different phantom setups.

matches the impedance of the source to that of the crystal to ensure maximum power transfer. The echoscope was used to transmit the ultrasonic pulses every 2 ms and the output of the receiver was measured. Figure 5.12 shows the measured receiver waveform when the power of the ultrasound pulses was varied for a phantom comprising of chicken meat, as shown in Figure 5.11. The measured output clearly shows that when the magnitude of the transmitted power is increased, the density of logic '1's increases as well. The digital output from the receiver could be decoded by a digital signal processor by averaging the output and then normalizing with respect to the maximum value. Figure 5.13 plots the normalized output for the three different phantom setups. The measured results show a monotonic response verifying that the crystals could be used for communicating digital bit-steams where

the higher levels of transmitted power ($>$ 15dB) could be distinguished from no transmissions. Also it can be seen from the measured results in Figure 5.13 that the receiver exhibits a higher sensitivity (lower activation threshold) when the transmission media is dominated by tissue. As expected the transmission through bone suffers from a higher attenuation but these results show that telemetry from within the bone structures (like bone marrow) is still feasible. In all the phantom experiments, the speed of data transmission determines the duration of the integration window which in turns determines the resolution of the receiver.

5.2.3 Summary and Conclusions

In section 3.1, we have proposed a design of a self-powered CMOS transceiver that can be used for through-substrate communications using ultrasonic pulses. The transceiver is powered by energy that can be harvested from ambient vibrations present in the susbtrate and hence can operate without batteries. It is envisioned that the transceiver will be integrated with a digital processor (also powered by the energy harvesting modules) which will be programmed to control the transmitter and also process the digital output produced by the receiver. The processor will also be programmed to implement communication protocols that can be used to form a sensor network inside the substrate such that important information related to the health of the structure can be reliably communicated.

In section 3.2, we investigated the feasibility of a miniaturized, wireless sonomicrometry based telemetry system that can be implanted inside biological structures like tissue and bones. We have proposed transmitter circuits that can be used to drive the sonomicrometry crystals (transmit data) and we have demonstrated that an on-chip receiver can be used to measure or decode the transmitted data. The proposed system offers numerous advantages

over a comparable RF telemetry system in terms of size and usability; and hence can be used for in-vivo monitoring of different structures ranging from bone marrow to cardiac valves to endoscopic structures. Characterization of the proposed telemetry system for these different structures, combined with the ability of harvest ultrasonic energy [91] for real-time operation will form the basis of future research in this area.

Three important notes we can get from tis chapter;

- First: the electrically isolated conductor for the application of SC-WPT can be any conductive substrate (live tissue or any other conductive material). Therefore, we claim that we can apply our proposed SC-WPT for wide range of applications for substrate computing and health monitoring.
- Second: it is preferable to reduce the power consumption of the electronic devices in addition to reduce their sizes while keeping them functional in order to improve the power transfer efficiency,
- Third: It is always possible to combine ambient energy harvesters with the self-capacitance based WPT to wirelessly self-power the electronic devices without involving an external power source.

In the next chapter, I will show some preliminary results and suggestions for future work to make the SC-WPT applications a reality in the near future.

Chapter 6

Conclusion

In this thesis, we focused on overcoming the problem of low power transfer efficiency (PTE) associated with conventional wireless power transfer approaches. The conventional wireless power transfer approaches use ; radio frequency (RF), Induction (Ind) and Ultrasound (US) to deliver the power to wearable and implantable electronic devices. We introduced a new highly efficient nonconventional wireless power transfer (WPT) technology through the investment of the human body's self-capacitance (SC) to deliver electrical power wirelessly to sub-millimeter sized wearable electronic devices and over a relatively long distance. We proved theoretically and experimentally that the self-capacitance (SC)-based WPT has significant advantages in terms of the power transfer-efficiency (PTE) (close to 99%), receiver form-factor, and system scalability in addition to misalignment insensitivity when compared to other approaches/modes of WPT methods. Wearable electronic devices are responsible for wireless health monitoring and fitness tracking, and they consist of various functional blocks for power management, sensing/actuation, communication and sometimes even signal processing. Depending on their design and application's constraints, their power consumption varies from a few micro-Watts to a few milli-Watts. Also, in this thesis, we focused on reducing the operational power consumption of wearable electronic devices by shrinking the

size of their functional blocks which can lead to prolonging their lifetime and making their future applications feasible.

6.1 Thesis Contributions

The main contributions of this thesis can be outlined as follows:

- The first to Introduce the concept of self-capacitance based wireless power transfer (SC-WPT), which is capable of transferring adequate power on-demand to millimeter size and less wearable electronic devices, and investigate its limitations.
- The first to investigate hybrid SC-WPT and telemetry/sensing, thereby developing a complete design of the SC-WPT to transfer microwatts of power wirelessly to designed and implemented power-efficient telemetry/sensors associated with radio frequency RF-signal backscattering antenna used for remote sensing of important biological/physiological parameters.
- The first to demonstrate and verify the SC-WPT technique through the modeling and optimization to maximize the power transfer efficiency (PTE), where the PTE parameter of the SC-WPT has been analyzed.
- The first to extend the SC-WPT to wireless power broadcasting (WPB) with applications for long-term monitoring through the design and implementation of energy-efficient diagnostic cages and smart rooms.

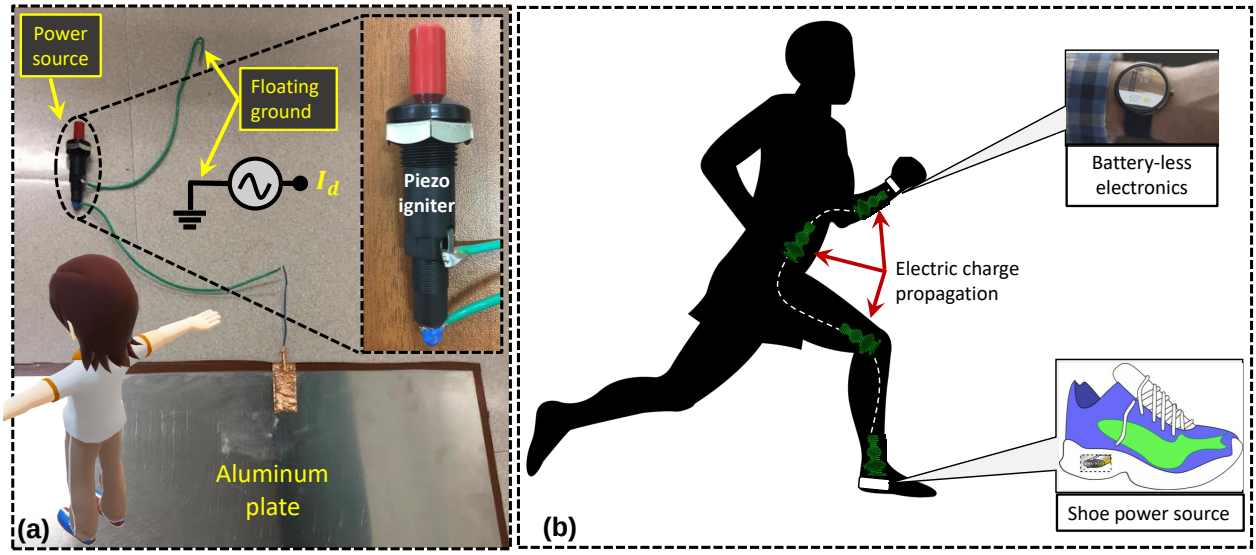

Figure 6.1: Self-powering based SC-WPT : (a) Experimental setup showing an SC-WPT configuration using a piezo igniter as a power source; (b) Future envision of the Biomechatronics approach showing self-powering based SC-WPT using the human shoe as a self-power generator [3–5].

6.2 Future Work

The advantages of the proposed SC-WPT make it a better fit for wearable electronic devices and possibly even implantable electronic devices. Therefore, I recommend in the future to improve this approach even more through making the entire system self-powered by harvesting the energy from the motion of the ambulatory system or from the environment using different methods of energy-harvesting modalities. We have preliminary data of self-powering based SC-WPT from the experimental setup shown in Figure 6.1, where we replaced the floating ground function generator in Figure 3.6 (a) with a piezo igniter (that creates voltage as a single spark when it is struck) as shown in Figure 6.1 (a) and we were able to harvest around 200 mV in the receiver side every time we click the igniter. In future, as a feasible Biomechatronics approach we will work on designing a shoe power source for this purpose

by setting a piezo igniter or similar inside the shoe to harvest the energy from human walking/running as shown in Figure 6.1 (b) to prove the concept. This energy harvesting ability in the absence of an external power source will complement our proposed wireless power transfer Biomechatronics approach and improve its reliability.

It could also be possible to extend the SC-WPT to be applicable for implantable devices through converting the electrical energy into different energy forms that can penetrate or propagate through a human body to reach implantable devices.

Finally, we will continue investigating different and alternative modalities of low-power analog and digital circuits designs to relax their power requirements in addition to shrinking their sizes, making the future design of applications for the Internet-of-things (IoT) even more promising.

Bibliography

[1] R. Gargulinski, "What do mice hate," 2017.

[2] T. Timek, J. Glasson, P. Dagum, G. Green, J. Nistal, M. Komeda, G. Daughters, A. Bolger, L. Foppiano, N. J. Ingels, and D. Miller, "Ring annuloplasty prevents delayed leaflet coaptation and mitral regurgitation during acute left ventricular ischemia," *J Thorac Cardiovasc Surg*, April 2000.

[3] "https://st-joseph.franco-nord.cnna/," 2016.

[4] J. Garvey, "Piezoelectric generator creates power from shoes," April 30, 2010.

[5] R. WYLIE, "Your body, the battery: Powering gadgets from human "biofuel"," 7/19/2015.

[6] S. H. Kondapalli, Y. Alazzawi, M. Malinowski, T. Timek, and S. Chakrabartty, "Multiaccess in vivo biotelemetry using sonomicrometry and m-scan ultrasound imaging," *IEEE Transactions on Biomedical Engineering*, vol. 65, no. 1, pp. 149–158, 2018.

[7] Y. Alazzawi, K. Aono, E. L. Scheller, and S. Chakrabartty, "Exploiting self-capacitances for wireless power transfer," *IEEE transactions on biomedical circuits and systems*, vol. 13, no. 2, pp. 425–434, 2019.

[8] W. Liu and J. Zhang, "Single layer self-capacitance touch screen realizing multi-touch identification as well as its data processing method," Dec. 29 2015. US Patent 9,223,337.

[9] K. Fujii, M. Takahashi, K. Ito, K. Hachisuka, Y. Terauchi, Y. Kishi, K. Sasaki, and K. Itao, "Study on the transmission mechanism for wearable device using the human body as a transmission channel," *IEICE transactions on communications*, vol. 88, no. 6, pp. 2401–2410, 2005.

[10] N. Cho, J. Yoo, S.-J. Song, J. Lee, S. Jeon, and H.-J. Yoo, "The human body characteristics as a signal transmission medium for intrabody communication," *IEEE transactions on microwave theory and techniques*, vol. 55, no. 5, pp. 1080–1086, 2007.

[11] J. Bae, H. Cho, K. Song, H. Lee, and H.-J. Yoo, "The signal transmission mechanism on the surface of human body for body channel communication," *IEEE Transactions on microwave theory and techniques*, vol. 60, no. 3, pp. 582–593, 2012.

[12] R. Xu, W. C. Ng, H. Zhu, H. Shan, and J. Yuan, "Equation environment coupling and interference on the electric-field intrabody communication channel," *IEEE Transactions on biomedical engineering*, vol. 59, no. 7, pp. 2051–2059, 2012.

[13] M. D. Pereira, G. A. Alvarez-Botero, and F. R. de Sousa, "Characterization and modeling of the capacitive hbc channel," *IEEE Transactions on Instrumentation and Measurement*, vol. 64, no. 10, pp. 2626–2635, 2015.

[14] J. Park, H. Garudadri, and P. P. Mercier, "Channel modeling of miniaturized battery-powered capacitive human body communication systems," *IEEE Transactions on Biomedical Engineering*, vol. 64, no. 2, pp. 452–462, 2017.

[15] X.-Q. Zhu, Y.-X. Guo, and W. Wu, "Investigation and modeling of capacitive human body communication," *IEEE transactions on biomedical circuits and systems*, vol. 11, no. 2, pp. 474–482, 2017.

[16] R. Jegadeesan, S. Nag, K. Agarwal, N. V. Thakor, and Y.-X. Guo, "Enabling wireless powering and telemetry for peripheral nerve implants.," *IEEE J. Biomedical and Health Informatics*, vol. 19, no. 3, pp. 958–970, 2015.

[17] M. S. Heo, H. S. Moon, H. C. Kim, H. W. Park, Y. H. Lim, and S. H. Paek, "Fully implantable deep brain stimulation system with wireless power transmission for long-term use in rodent models of parkinson's disease," *Journal of Korean Neurosurgical Society*, vol. 57, no. 3, p. 152, 2015.

[18] J. A. Shaw, "Radiometry and the friis transmission equation," *American Journal of Physics*, vol. 81, no. 1, pp. 33–37, 2013.

[19] D. Ahn and M. Ghovanloo, "Optimal design of wireless power transmission links for millimeter-sized biomedical implants.," *IEEE Trans. Biomed. Circuits and Systems*, vol. 10, no. 1, pp. 125–137, 2016.

[20] E. E. Aktakka and K. Najafi, "A micro inertial energy harvesting platform with self-supplied power management circuit for autonomous wireless sensor nodes," *IEEE Journal of Solid-State Circuits*, vol. 49, no. 9, pp. 2017–2029, 2014.

[21] Y. Karimi, A. Khalifa, W. Montlouis, M. Stanaćević, and R. Etienne-Cummings, "Coil array design for maximizing wireless power transfer to sub-mm sized implantable devices," in *Biomedical Circuits and Systems Conference (BioCAS), 2017 IEEE*, pp. 1–4, IEEE, 2017.

[22] D. Seo, R. M. Neely, K. Shen, U. Singhal, E. Alon, J. M. Rabaey, J. M. Carmena, and M. M. Maharbiz, "Wireless recording in the peripheral nervous system with ultrasonic neural dust," *Neuron*, vol. 91, no. 3, pp. 529–539, 2016.

[23] J. Charthad, M. J. Weber, T. C. Chang, and A. Arbabian, "A mm-sized implantable medical device (imd) with ultrasonic power transfer and a hybrid bi-directional data link," *IEEE Journal of solid-state circuits*, vol. 50, no. 8, pp. 1741–1753, 2015.

[24] Y. Alazzawi and S. Chakrabartty, "Design of cmos telemetry circuits for in-vivo wireless sonomicrometry," in *Circuits and Systems (ISCAS), 2016 IEEE International Symposium on*, pp. 2022–2025, IEEE, 2016.

[25] Y. Zhang, J. Zhou, G. Laput, and C. Harrison, "Skintrack: Using the body as an electrical waveguide for continuous finger tracking on the skin," in *Proceedings of the 2016 CHI Conference on Human Factors in Computing Systems*, pp. 1491–1503, ACM, 2016.

[26] J. C. Maxwell and J. J. Thompson, *A treatise on electricity and magnetism*, vol. 2. Clarendon, 1904.

[27] X. Lu, P. Wang, D. Niyato, D. I. Kim, and Z. Han, "Wireless charging technologies: Fundamentals, standards, and network applications," *IEEE Communications Surveys & Tutorials*, vol. 18, no. 2, pp. 1413–1452, 2016.

[28] H. G. Schantz, "Near field propagation law & a novel fundamental limit to antenna gain versus size," in *Antennas and Propagation Society International Symposium, 2005 IEEE*, vol. 3, pp. 237–240, IEEE, 2005.

[29] H. Zeine, D. Mayes, B. Renneberg, and A. Alfarra, "Energy delivery modulation in wireless power delivery environments," June 6 2017. US Patent 9,673,665.

[30] D. Williams, R. Qamheyeh, H. Zeine, and D. D. Mayes, "Systems and methods for improved phase determinations in wireless power delivery environments," Feb. 6 2018. US Patent 9,887,589.

[31] L. Radziemski and I. R. S. Makin, "In vivo demonstration of ultrasound power delivery to charge implanted medical devices via acute and survival porcine studies," *Ultrasonics*, vol. 64, pp. 1–9, 2016.

[32] Y. Hu, X. Zhang, J. Yang, and Q. Jiang, "Transmitting electric energy through a metal wall by acoustic waves using piezoelectric transducers," *IEEE Transactions on Ultrasonics, Ferroelectrics, and Frequency Control*, vol. 50, no. 7, pp. 773–781, 2003.

[33] T. L. Szabo, *Diagnostic ultrasound imaging: inside out*. Academic Press, 2004.

[34] U.-M. Jow, P. McMenamin, M. Kiani, J. R. Manns, and M. Ghovanloo, "Enercage: A smart experimental arena with scalable architecture for behavioral experiments," *IEEE Transactions on Biomedical Engineering*, vol. 61, no. 1, pp. 139–148, 2014.

[35] X. Lu, D. Niyato, H. Jiang, D. I. Kim, Y. Xiao, and Z. Han, "Ambient backscatter assisted wireless powered communications," *IEEE Wireless Communications*, vol. 25, no. 2, pp. 170–177, 2018.

[36] B. Kellogg, A. Parks, S. Gollakota, J. R. Smith, and D. Wetherall, "Wi-fi backscatter: Internet connectivity for rf-powered devices," in *ACM SIGCOMM Computer Communication Review*, vol. 44, pp. 607–618, ACM, 2014.

[37] H. N. Schwerdt, F. A. Miranda, and J. Chae, "Wireless fully passive multichannel recording of neuropotentials using photo-activated rf backscattering methods," *IEEE Transactions on Microwave Theory and Techniques*, vol. 63, no. 9, pp. 2965–2970, 2015.

[38] D. Liu and S. Georgakopoulos, "Cylindrical misalignment insensitive wireless power transfer systems," *IEEE Transactions on Power Electronics*, 2018.

[39] D. Liu, H. Hu, and S. V. Georgakopoulos, "Misalignment sensitivity of strongly coupled wireless power transfer systems," *IEEE Trans. Power Electron*, vol. 32, no. 7, pp. 5509–5519, 2017.

[40] M. Huang, Y. Lu, and R. P. Martins, "A reconfigurable bidirectional wireless power transceiver for battery-to-battery wireless charging," *IEEE Transactions on Power Electronics*, 2018.

[41] K.-S. Yoon, S.-H. Lee, I.-K. Cho, H.-J. Lee, and G.-H. Cho, "Dual receiver coils wireless power transfer system with interleaving switching," *IEEE Transactions on Power Electronics*, vol. 33, no. 12, pp. 10016–10020, 2018.

[42] H. Vihvelin, J. R. Leadbetter, M. Bance, J. A. Brown, and R. B. Adamson, "Compensating for tissue changes in an ultrasonic power link for implanted medical devices," *IEEE transactions on biomedical circuits and systems*, vol. 10, no. 2, pp. 404–411, 2016.

[43] A. Ma and A. S. Poon, "Midfield wireless power transfer for bioelectronics," *IEEE Circuits and Systems Magazine*, vol. 15, no. 2, pp. 54–60, 2015.

[44] R. Jegadeesan, K. Agarwal, Y.-X. Guo, S.-C. Yen, and N. V. Thakor, "Wireless power delivery to flexible subcutaneous implants using capacitive coupling," *IEEE Transactions on Microwave Theory and Techniques*, vol. 65, no. 1, pp. 280–292, 2017.

[45] A. Aldaoud, J.-M. Redoute, K. Ganesan, G. S. Rind, S. E. John, S. M. Ronayne, N. L. Opie, D. J. Garrett, and S. Prawer, "Near-field wireless power transfer to stent-based biomedical implants," *IEEE Journal of Electromagnetics, RF and Microwaves in Medicine and Biology*, vol. 2, no. 3, pp. 193–200, 2018.

[46] P. B. Ishai, M. S. Talary, A. Caduff, E. Levy, and Y. Feldman, "Electrode polarization in dielectric measurements: a review," *Measurement Science and Technology*, vol. 24, no. 10, p. 102001, 2013.

[47] U. Food, D. Administration, *et al.*, "Information for manufacturers seeking marketing clearance of diagnostic ultrasound systems and transducers," *Rockville, MD: Center for Devices and Radiological Health, US Food and Drug Administration*, 1997.

[48] F. Commission *et al.*, "Guidelines for evaluating the environmental effects of radiofrequency radiation," *FCC 96-326*, 1996.

[49] J. C. Lin, "A new ieee standard for safety levels with respect to human exposure to radio-frequency radiation," *IEEE Antennas and Propagation Magazine*, vol. 48, no. 1, pp. 157–159, 2006.

[50] F. Galembeck and T. A. Burgo, "Accidents and losses caused by electrostatic discharge," in *Chemical Electrostatics*, pp. 169–183, Springer, 2017.

[51] Y. Alazzawi, K. Aono, E. L. Scheller, and S. Chakrabartty, "Self-capacitance based wireless power broadcasting for internet of medical things (iomt)," *IEEE Transactions on Internet of Things*, 2020, Under Review.

[52] A. Marincic and D. Budimir, "Tesla's contribution to radiowave propagation," in *5th International Conference on Telecommunications in Modern Satellite, Cable and Broadcasting Service. TELSIKS 2001. Proceedings of Papers (Cat. No. 01EX517)*, vol. 1, pp. 327–331, IEEE, 2001.

[53] G. J. Joyia, R. M. Liaqat, A. Farooq, and S. Rehman, "Internet of medical things (iomt): applications, benefits and future challenges in healthcare domain," *J Commun*, vol. 12, no. 4, pp. 240–7, 2017.

[54] M. Roes, M. Hendrix, and J. Duarte, "Contactless energy transfer through air by means of ultrasound," in *IECON 2011-37th Annual Conference of the IEEE Industrial Electronics Society*, pp. 1238–1243, IEEE, 2011.

[55] A. S. Rekhi, B. T. Khuri-Yakub, and A. Arbabian, "Wireless power transfer to millimeter-sized nodes using airborne ultrasound," *IEEE transactions on ultrasonics, ferroelectrics, and frequency control*, vol. 64, no. 10, pp. 1526–1541, 2017.

[56] R. Dekimpe, P. Xu, M. Schramme, P. Gérard, D. Flandre, and D. Bol, "A batteryless ble smart sensor for room occupancy tracking supplied by 2.45-ghz wireless power transfer," *Integration*, vol. 67, pp. 8–18, 2019.

[57] H.-H. Greve, "Rubber, 2. natural," *Ullmann's Encyclopedia of Industrial Chemistry*, 2000.

[58] B. Kapilevich, B. Litvak, M. Anisimov, D. Hardon, and Y. Pinhasi, "Complex permittivity measurements of textiles and leather in a free space: An angular-invariant approach," *International Journal of Microwave Science and Technology*, vol. 2012, 2012.

[59] T. G. Zimmerman, "Personal area networks: near-field intrabody communication," *IBM systems Journal*, vol. 35, no. 3.4, pp. 609–617, 1996.

[60] Y. Alazzawi, O. Chatterjee, and S. Chakrabartty, "A compact and energy-efficient ultrasound receiver using ptat reference circuit," *Microelectronics Journal*, vol. 94, p. 104656, 2019.

[61] J. Zhang, Z. Yu, H. Yang, M. Wu, and J. Yang, "Wireless communication using ultrasound through metal barriers: Experiment and analysis," in *2015 10th International Conference on Information, Communications and Signal Processing (ICICS)*, pp. 1–5, IEEE, 2015.

[62] S. Das, H. Salehi, Y. Shi, S. Chakrabartty, R. Burgueno, and S. Biswas, "Towards packet-less ultrasonic sensor networks for energy-harvesting structures," *Computer Communications*, vol. 101, pp. 94–105, 2017.

[63] M. Rigo, "Analysis and laboratory verification of bandgap prototypes, circuit engineering, optimization of trimming process," 2013.

[64] K. Soumyanath and V. S. Borkar, "An analog scheme for fixed-point computation-part ii: Applications," *IEEE Transactions on Circuits and Systems I: Fundamental Theory and Applications*, vol. 46, no. 4, pp. 442–451, 1999.

[65] E. K. Blum and X. Wang, "Stability of fixed points and periodic orbits and bifurcations in analog neural networks," *Neural Networks*, vol. 5, no. 4, pp. 577–587, 1992.

[66] M. Sawan, R. Chebli, and A. Kassem, "Integrated front-end receiver for a portable ultrasonic system," *Analog integrated circuits and signal processing*, vol. 36, no. 1-2, pp. 57–67, 2003.

[67] R. Sarpeshkar, R. F. Lyon, and C. Mead, "A low-power wide-linear-range transconductance amplifier," *Analog Integrated Circuits and Signal Processing*, vol. 13, no. 1-2, pp. 123–151, 1997.

[68] A. Veeravalli, E. Sánchez-Sinencio, and J. Silva-Martínez, "Transconductance amplifier structures with very small transconductances: A comparative design approach," *IEEE Journal of Solid-State Circuits*, vol. 37, no. 6, pp. 770–775, 2002.

[69] A. Veeravalli, E. Sánchez-Sinencio, and J. Silva-Martínez, "A CMOS transconductance amplifier architecture with wide tuning range for very low frequency applications," *IEEE Journal OF Solid-state circuits*, vol. 37, no. 6, pp. 776–781, 2002.

[70] K. Chen, H.-S. Lee, A. P. Chandrakasan, and C. G. Sodini, "Ultrasonic imaging transceiver design for CMUT: a three-level 30-vpp pulse-shaping pulser with improved efficiency and a noise-optimized receiver," *IEEE Journal of Solid-State Circuits*, vol. 48, no. 11, pp. 2734–2745, 2013.

[71] X. Huang, J. H. Cheong, H.-K. Cha, H. Yu, M. Je, and H. Yu, "A high-frequency transimpedance amplifier for CMOS integrated 2d cmut array towards 3d ultrasound imaging," in *Engineering in Medicine and Biology Society (EMBC), 2013 35th Annual International Conference of the IEEE*, pp. 101–104, IEEE, 2013.

[72] T.-C. Cheng and T.-H. Tsai, "CMOS ultrasonic receiver with on-chip analog-to-digital front end for high-resolution ultrasound imaging systems," *IEEE Sensors Journal*, vol. 16, no. 20, pp. 7454–7463, 2016.

[73] I. O. Wygant, X. Zhuang, D. T. Yeh, O. Oralkan, A. S. Ergun, M. Karaman, and B. T. Khuri-Yakub, "Integration of 2D CMUT arrays with front-end electronics for volumetric ultrasound imaging," *IEEE transactions on ultrasonics, ferroelectrics, and frequency control*, vol. 55, no. 2, 2008.

[74] E. Vittoz and J. Fellrath, "CMOS analog integrated circuits based on weak inversion operations," *IEEE journal of solid-state circuits*, vol. 12, no. 3, pp. 224–231, 1977.

[75] E. A. Vittoz, "The design of high-performance analog circuits on digital CMOS chips," *IEEE Journal of Solid-State Circuits*, vol. 20, no. 3, pp. 657–665, 1985.

[76] T. Ytterdal, Y. Cheng, and T. A. Fjeldly, *Device modeling for analog and RF CMOS circuit design*. John Wiley & Sons, 2003.

[77] B. Razavi, *Design of Analog CMOS Integrated Circuits, Second Edition*. McGraw-Hill, 2017.

[78] D. Seo, J. M. Carmena, J. M. Rabaey, E. Alon, and M. M. Maharbiz, "Neural dust: An ultrasonic, low power solution for chronic brain-machine interfaces," *arXiv preprint arXiv:1307.2196*, 2013.

[79] R.-L. Lin, *Piezoelectric transformer characterization and application of electronic ballast*. PhD thesis, Virginia Tech, 2001.

[80] D. J. Leo, *Engineering analysis of smart material systems*. John Wiley & Sons, 2007.

[81] Y. Alazzawi and S. Chakrabartty, "Self-powered system-on-chip for substrate computing and ultrasonic communications," *2017 IEEE 60th International Midwest Symposium on Circuits and Systems (MWSCAS)*, Aug. 2017.

[82] J. Morizio, S. Guhados, J. Castellucci, and O. von Ramm, "64-channel ultrasound transducer amplifier," in *Southwest Symposium on Mixed-Signal Design, 2003.*, pp. 228–232, IEEE, 2003.

[83] H. Choi, X. Li, S.-T. Lau, C. Hu, Q. Zhou, and K. K. Shung, "Development of integrated preamplifier for high-frequency ultrasonic transducers and low-power handheld

receiver," *IEEE transactions on ultrasonics, ferroelectrics, and frequency control*, vol. 58, no. 12, pp. 2646–2658, 2011.

[84] R. R. Harrison and C. Charles, "A low-power low-noise CMOS amplifier for neural recording applications," *IEEE Journal of solid-state circuits*, vol. 38, no. 6, pp. 958–965, 2003.

[85] B. Wang, J. R. Hellums, and C. G. Sodini, "Mosfet thermal noise modeling for analog integrated circuits," *IEEE Journal of Solid-State Circuits*, vol. 29, no. 7, pp. 833–835, 1994.

[86] J. Chang, A. Abidi, and C. Viswanathan, "Flicker noise in CMOS transistors from subthreshold to strong inversion at various temperatures," *IEEE Transactions on Electron Devices*, vol. 41, no. 11, pp. 1965–1971, 1994.

[87] A. Arnaud and C. Galup-Montoro, "Consistent noise models for analysis and design of cmos circuits," *IEEE Transactions on Circuits and Systems I: Regular Papers*, vol. 51, no. 10, pp. 1909–1915, 2004.

[88] X. Lu1, C. Liu, H. Jiang, X. Zou, A. Zhang, and K. M. Lau, "Ultralow reverse leakage current in algan/gan lateral schottky barrier diodes grown on bulk gan substrate," *IOPscience*, pp. 031001–1—031001–4, January 28, 2016.

[89] P. Hasler, "Overview of floating-gate devices, circuits, and systems," *Circuits and Systems—II: Analog and Digital Signal Processing*, vol. 48, no. 1, JANUARY 2001.

[90] P.-J. Shih and W.-P. Shih, "Design, fabrication, and application of bio-implantable acoustic power transmission," *Microelectromechanical Systems, Journal of*, vol. 19, no. 3, pp. 494–502, 2010.

[91] B. Fang, T. Feng, M. Zhang, and S. Chakrabartty, "Feasibility of b-mode diagnostic ultrasound energy transfer and telemetry to a cm2 sized deep-tissue implant," IEEE Symposium on Circuits and Systems (ISCAS 2015), Lisbon, Portugal, 2015.

[92] R. Gorman, J. McCaughan, M. Ratcliffe, K. Gupta, J. Streicher, V. Ferrari, S. M. JohnSutton, D. Bogen, and L. J. Edmunds, "Pathogenesis of acute ischemic mitral regurgitation in three dimensions," *J Thorac Cardiovasc Surg*, April 1995.

[93] J. A. Spencer, F. Ferraro, E. Roussakis, A. Klein, J. Wu, J. M. Runnels, W. Zaher, L. J. Mortensen, C. Alt, R. Turcotte, R. Yusuf, D. Côté, S. A. Vinogradov, D. T. Scadden, and C. P. Lin, "Swallowablewireless capsule endoscopy: Progress and technical challenges," *nature*, March 2014.

[94] G. Pan and LitongWang, "Direct measurement of local oxygen concentration in the bone marrow of live animals," *Gastroenterology Research and Practice*, October 2012.

[95] A. Christ, M. Douglas, J. Nadakuduti, and N. Kuster, "Assessing human exposure to electromagnetic fields from wireless power transmission systems," *Proceedings of the IEEE*, vol. 101, no. 6, pp. 1482–1493, 2013.

[96] A. Christ, M. G. Douglas, J. M. Roman, E. B. Cooper, A. P. Sample, B. H. Waters, J. R. Smith, and N. Kuster, "Evaluation of wireless resonant power transfer systems with human electromagnetic exposure limits," *IEEE Transactions on Electromagnetic compatibility*, vol. 55, no. 2, pp. 265–274, 2012.

[97] I. Laakso, S. Tsuchida, A. Hirata, and Y. Kamimura, "Evaluation of sar in a human body model due to wireless power transmission in the 10 mhz band," *Physics in Medicine & Biology*, vol. 57, no. 15, p. 4991, 2012.

[98] F. 96-326, "Guidelines for evaluating the environmental effects of radio frequency radiation," 1996.

Appendix A

Safety of Self-Capacitance-based WPT

WPT systems induce electric fields in the human body tissue if a body is in close vicinity to the power source. This near-field exposure may pose safety issues like tissue heating from radio frequency absorption or nerve stimulation due to induced currents or fields [95]. Previously, some studies discussed the human body exposure to different WPT [96, 97], but the available data according to U.S. Federal Communication Commission (FCC) are scarce and can not be used as a clear guideline for accurate quantification of this exposure.

In this thesis, we recruited human subjects for the obtaining experimental results to verify the proposed power transfer technique under approved IRB protocol #201907109, safety is an important factor that was considered. U.S. Food and Drug Administration (FDA) limits on power dissipation for SC-based WPT is estimated to be $2.5(\frac{mW}{mm^2})$ [47, 49, 98] which is significantly higher than the microwatts of power delivery reported in this paper. Furthermore, the devices used in sourcing the AC for these experiments were configured to limit the potential for a shock hazard in a short circuit event. This limit is defined for the galvanic DC current, but in our experiments we utilized the displacement current, which is safer than DC current, and no human body came in direct contact with electrified conductive substrate or power source electrode. Instead, the sole connection was through a coupling capacitor constructed by the human body and the electrically-isolated source electrode.

Vita

Yarub Omer Naji Alazzawi

Degrees

Ph.D., Electrical Engineering, Washington University in St. Louis, Missouri, USA, May 2020
M.S., Electrical Engineering, Washington University in St. Louis, Missouri, USA, May 2018
M.Sc., Mechatronics Engineering, Baghdad University, Baghdad, Iraq, June 2005
B.S., Mechatronics Engineering, Baghdad University, Baghdad, Iraq, June 2002

Professional Memberships

The Institute of Electrical and Electronics Engineers (IEEE)
IEEE Circuits and Systems Society

Publications

Journal Publications:

Y. Alazzawi, K. Aono, E. Scheller, and S. Chakrabartty, "Self-Capacitance based Wireless Power Broadcasting for Internet of Medical Things (IoMT)," *IEEE Trans. Internet of Things.*, 2020, (under review).

Y. Alazzawi, O. Chatterjee, and S. Chakrabartty, "A compact and energy-efficient ultrasound receiver using PTAT reference circuit," *Microelectronics Journal*, vol. 94, p. 104656, 2019.

Y. Alazzawi, K. Aono, E. Scheller, and S. Chakrabartty, "Exploiting self-capacitances for wireless power transfer," *IEEE Trans. Biomedical Circuits and Systems.*, vol. 13, no. 2, pp. 425–434, April. 2019.

S.H. Kondapalli, **Y. Alazzawi**, M. Malinowski, T. Timek, and S. Chakrabartty, "Multiaccess in vivo biotelemetry using sonomicrometry and m-scan ultrasound imaging," *IEEE Trans. Biomedical Engineering.*, vol. 65, no. 1, pp. 149–158, Jan. 2018.

S.H. Kondapalli, **Y. Alazzawi**, M. Malinowski, T. Timek, and S. Chakrabartty, "Feasibility of Self-Powering and Energy Harvesting Using Cardiac Valvular Perturbations," *IEEE Trans. Biomedical Engineering.*, vol. 12, no. 6, pp. 1392–1400, Dec. 2018.

Patents:

S. Chakrabartty, **Y. Alazzawi**, S. Signamaneni, K.K. Liu, and M. Yuan,"Systems and methods for detecting embedded target elements using signal interference," US PatentApp. 16/023,761.

S. Chakrabartty, **Y. Alazzawi**, K. Aono, and E. Scheller,"Method and Implementation of Wireless Power Delivery and Remote Sensing Using Self-Capacitances," US PatentApp. T-018759, pending.

Conference Publications:

Y. Alazzawi and S. Chakrabartty, "Self-powered system-on-chip for substrate computing and ultrasonic communications," *IEEE 60th International Midwest Symposium on Circuits and Systems (MWSCAS)*, Boston, MA, USA, August 6-9, 2017.

Y. Alazzawi and S. Chakrabartty, "Design of CMOS telemetry circuits for in-vivo wireless sonomicrometry ," *IEEE International Symposium on Circuits and Systems (ISCAS)*, Montreal, QC, Canada, May 22-25, 2016.

Y. Alazzawi, C. Qian and S. Chakrabartty, "Feasibility of noncontact ultrasound generation using implanted metallic surfaces as electromagnetic acoustic transducers," *IEEE Biomedical Circuits and Systems Conference (BioCAS)*, Atlanta, GA, USA, October 22-24, 2015.

May 2020